



THESIS

2

2004

57065472

This is to certify that the  
dissertation entitled

STUDIES OF SOME PROBLEMS RELATED TO ATOMIC  
ORDERING, MOLECULAR MOTION AND PAIR  
DISTRIBUTION FUNCTION

presented by

VALENTIN A. LEVASHOV

has been accepted towards fulfillment  
of the requirements for the

Ph.D. degree in Physics and Astronomy

M. F. Thayer

Major Professor's Signature

28 April 2004

Date

**LIBRARY**  
**Michigan State**  
**University**

**PLACE IN RETURN BOX** to remove this checkout from your record.  
**TO AVOID FINES** return on or before date due.  
**MAY BE RECALLED** with earlier due date if requested.

DATE DUE	DATE DUE	DATE DUE
<del>SEP 20 2005</del>		

STUDIES OF SOME PROBLEMS RELATED TO  
ATOMIC ORDERING, MOLECULAR MOTION  
AND  
PAIR DISTRIBUTION FUNCTION

By

Valentin A. Levashov

A DISSERTATION

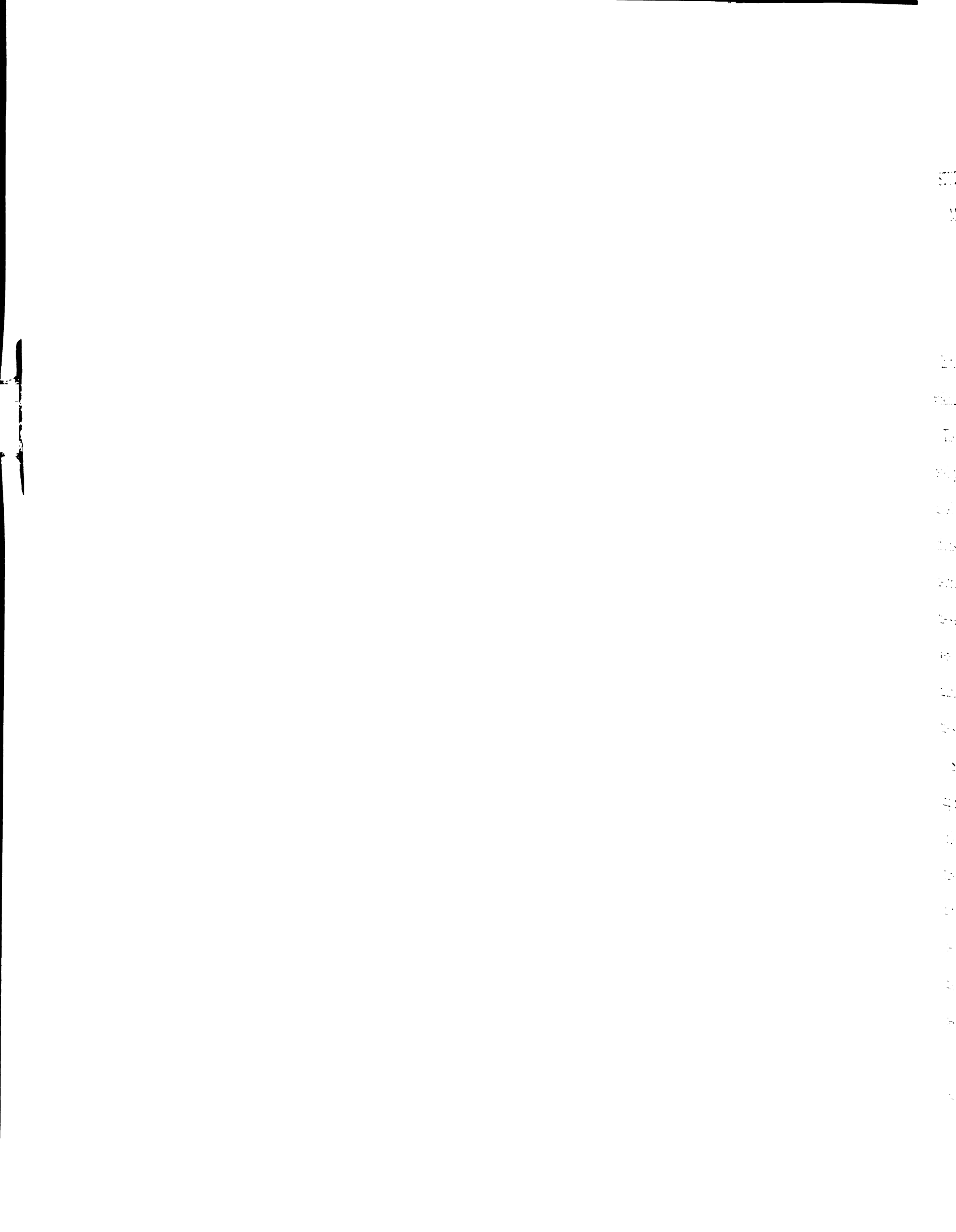
Submitted to  
Michigan State University  
in partial fulfillment of the requirements  
for the degree of

DOCTOR OF PHILOSOPHY

Department of Physics & Astronomy

2004





## ABSTRACT

### STUDIES OF SOME PROBLEMS RELATED TO ATOMIC ORDERING, MOLECULAR MOTION AND PAIR DISTRIBUTION FUNCTION

By

Valentin A. Levashov

In this thesis the results of my work on three out of four projects on which I was working during my Ph. D. under supervision of Prof. M.F. Thorpe are summarized.

The first project was devoted to the study of properties of a model that was developed to reproduce the ordering of ions in layered double hydroxides. In the model two types of positive ions occupy the sites of triangular lattice. The ordering of ions is assumed to occur due to the long-range Coulomb interaction. The charge neutrality is provided by the negative background charge, which is assumed to be the same at every site of the lattice. General properties of the model in 1d and 2d were studied and the phase diagrams were obtained. The obtained results predict multiple phase separations in this system of charges that can, in particular, affect the stability of the layered double hydroxides.

Some properties of the atomic pair distribution function (PDF) were studied during my work on the second project. Traditionally PDF was used to study atomic ordering at small distances, while it was assumed that at large distances PDF is featureless. Puzzled by the observation that PDF calculated for the crystalline Ni does not decay at large distances we studied the behavior, in particular the origin of decay, of PDF at large distances. The obtained results potentially could be used to measure the amount of imperfections in crystalline materials and to test instrumental resolution in X-ray and neutron diffraction experiments.

During my work on the third project we were developing a technique that would allow accurate calculation of PDF for the flexible molecules. Since quantum me-



chanical calculations are complicated and computationally demanding in calculations of PDF for molecules in liquid or gaseous phases, classical methods, like molecular dynamics are usually employed. Thus, quantum mechanical effects, like zero-point atomic motion, are usually ignored. However, it is necessary to take into account the effect of atomic zero-point motion if there is a desire to extract fine structural details from the PDF. We developed a method that allows incorporation of the effect of atomic zero-point motion into the results of classical MD simulations without performing full quantum mechanical calculations. This technique could be used to correct classically calculated PDFs and thus to achieve better agreement between modeled and experimental PDFs.

*To my grandfather, grandmother and mother*

## Acknowledgements

First of all, I would like to thank Prof. Michael F. Thorpe for being my thesis adviser. It was quite an experience working with him. For me, it was the first time working with somebody for such a long time. Thus, I was able to observe how another person thinks and works. Of course, I was able to make such observations in some other situations, but this time when the main objective of the work was "to think" about some particular topic, these observations were especially pronounced. I think that due to him I was able to realize on a deeper level what it means to really understand a problem and what it means to understand obtained results. There were situations when I would get some results and I would not really care about what they meant. His desire to understand the meaning of the results sometimes would really open new horizons in the problems. I was very often amazed by his ability to feel what should be the level of agreement between results obtained in different ways, i.e. how different curves should fit. Personally, I would often be satisfied with a fit that could be significantly worse. But a disagreement occurs when something is done in a wrong way. Thus his feeling for the level of agreement that we should get was allowing us to find errors in calculations. I think that in these situations I got rather significant lessons. In most cases he would give a good shot at where the error was, but sometimes he would just say: "I do not believe in this result. You have to go and find an error." Of course, it is very depressing to search for errors when you do not know what is wrong or why it is wrong. However, when the error was found (in most cases there were errors) it would make the results look really beautiful. In this sense I was able to realize that the beauty of the studied problems lies in the details. In other words, it is hard to see the beauty if one looks at the problem superficially or if one would just see the final answer.

In order to see the beauty of the correct answer it is necessary to see beforehand



100  
101  
102  
103  
104  
105  
106  
107  
108  
109  
110  
111  
112  
113  
114  
115  
116  
117  
118  
119  
120  
121  
122  
123  
124  
125  
126  
127  
128  
129  
130  
131  
132  
133  
134  
135  
136  
137  
138  
139  
140  
141  
142  
143  
144  
145  
146  
147  
148  
149  
150  
151  
152  
153  
154  
155  
156  
157  
158  
159  
160  
161  
162  
163  
164  
165  
166  
167  
168  
169  
170  
171  
172  
173  
174  
175  
176  
177  
178  
179  
180  
181  
182  
183  
184  
185  
186  
187  
188  
189  
190  
191  
192  
193  
194  
195  
196  
197  
198  
199  
200

what **an** incorrect answer looks like. I would say that in these details all of the **problems** that I was working on were interesting. They were somewhat non-trivial. Thus, **it** was often difficult and depressing, but in the same time enjoyable to work on them. **On** the other hand, I often was suffering from lack of understanding of what the **problem** that we were working on was really about and of what results we wanted to **obtain**.

**Often**, I also had a hard time trying to understand why it was important to work on this **problem** and what its scientific significance was. However, my discussions with **different** people revealed that it is in principal the situation that occurs in science **relatively** often.

Sometimes we were arguing on this and some other issues. As it seems to me now, it **was** very important for me because I was learning to fight for my own opinion. At the **same** time, I guess that it was rather difficult for him to tolerate such an attitude and **I** should acknowledge his tolerance and diplomacy on these issues.

**While** working on different projects I was communicating with different people. I **would** like to acknowledge them in a "problem by problem" fashion.

**In** connection with the "Coulomb lattice gas" problem I would like to acknowledge the **following** people. I would like to thank Prof. J.B. Parkinson for his explanations **on** the details of the program that was used previously to run Monte Carlo simulations. I **had** a very joyful collaboration with Prof. B.W. Southern. His calm and deep **attitude** made the study of this problem much more systematic. In particular it was his **idea** (and realization) to calculate the properties of the 1d chain with interaction **beyond** nearest neighbors with transfer matrix method. This allowed us to have a **basically** exact solution for this case. Together, we also gained a deeper understanding of the devils staircase formalism that I would not have been able obtain by myself. He **also** employed Bonsall-Maradudin formalism to calculate exactly the energies of the **given** configurations in 2d that was also a significant development. Especially, I



would like to acknowledge his support in preparing the materials for the publication [2].

Since this paper is presented in this thesis without any significant changes as a second chapter I should say that some parts of it that are related to the properties of the linear chain are written by Prof. B.W. Southern.

I would like to acknowledge Prof. S.D. Mahanti who carefully read the final version of the paper and with whom I had detailed discussion of this paper.

I also would like to thank Prof. Thomas J. Pinnavaia for reading the introduction to the paper. Especially, I also would like to acknowledge Dr. M.V. Chubynsky with whom I had several very important discussions. In particular the idea about the phase separation came to my mind during one of these discussions and it was the first time when I pronounced the words: "there is phase separation". This conversation took place at a very important moment and if we would not have had it things could have developed in a completely different way in general.

While working on problems related to the pair distribution function (PDF) I had long discussions with Valeri G. Petkov and Emil Bozin. In particular, as a result of one of such discussions, I had the idea to write a paper on the role of instrumental resolution function and for the first time I calculated PDF up to 200 Å. It was the first time when I was surprised that it does not decay. The importance of this observation was realized a bit later due to M.F. Thorpe and Simon J.L. Billinge and after that we calculated PDF at distances up to 10000 Å. Even before, as I learned a bit later, this behavior was observed in the lab of S.J.L. Billinge (I saw a picture of a PDF on the screen of E. Bozins computer with non-decaying PDF at 150 Å). However, it seems that there was a belief that eventually it should decay.

At some moment, Prof. Phillip M. Duxbury advised me to look for a connection between the non-decaying behavior of the PDF in real space and statistics of energy levels in  $\vec{k}$  space.

17

18

19

20

21

22

23

24

25

26

27

28

29

30

31

32

33

34

35

36

37

38

39

40

41

42

43

44

45

**Due** to this advice I later found a paper [57] and found out that the behavior of PDF **is** related to the Gauss circle problem. There were also few other conversations.

I **would** like to thank Jean Soo Chung for his explanation on how programs for calculations of the PDF work and Xiangyun Qiu who was operatively providing the experimental data for me when I needed them. Of course, all this interest in the PDF here **is in** many senses due to S.J.L. Billinge with whom I also had useful discussions.

I **also** had several useful discussions with Prof. Robert I. Cukier and Prof. James E. **Jackson**, on some issues related to molecular dynamics simulations and issues related to molecular modelling in general.

I **would** like to acknowledge Dr. M. Lei for being my office mate for the last year and **half**. He was the first person with whom I was sharing all the ideas that were **coming** to my mind. He also was helping me to find little mistakes in my computer programs and manage some other computer issues. Often he was just saying that my program does not work because in the description of variable I put a dot instead of a **comma**. This helped save me lots of time. We in general discussed many different **issues** and it made life in the office much more plausible, at least for me.

**There** are several people who helped me a lot on computer related issues. Very **often** I was asking Dr. Tibor Nagy for advice. During my first two years here Mykyta Chubynsky were also helping me. I had also few discussions with Dr. Andrew J. **Rader**. Of course, I should thank the computer staff of the Physics Department, **especially** Dr. George J. Perkins, Jeffrey R. Bowes, Nicholas J. Kreucher, Margaret A. **Wilke** and Robert T. Neary.

I **would** like to acknowledge the members of my guidance committee: Prof. J. **Bass**, Prof. S.J.L. Billinge, Prof. P.M. Duxbury, Prof. J.E. Jackson, and Prof. S.D. **Mahanti**.

I **also** would like to thank Prof. D. Tomanek for bringing me to MSU.

I **would** like to express my sincere gratitude to all of those whose names I would not

list **here**, but whose presence was extremely important during these six years. They are **those** whom I was asking for advice, those who were helping me in different life **situations**, those with whom I was talking about different things, those with whom I was **playing** tennis and volleyball, scuba diving, playing underwater hockey, dancing, **partying** and (after all) drinking in Peanut Barrel. I would like to acknowledge all of **you** because you were turning my existence into living. Thank you very much! **There** are also a few memories that would determine my behavior in some complex situations and I am happy that I have them.

I also would like to thank those who were correcting my English (including the writing center of MSU) in the present thesis.

**Finally** I would like to acknowledge my mother and other relatives for their care and **belief** in me.

Abstract

Acknowledgments

List of Figures

List of Tables

1. Introduction

## Table of Contents

<b>Abstract</b>	<b>1</b>
<b>Acknowledgements</b>	<b>v</b>
<b>List of tables</b>	<b>xiv</b>
<b>List of figures (Images in this thesis are presented in color)</b>	<b>xv</b>
<b>1 Introduction</b>	<b>1</b>
1.0.1 Chapter 2: Charged Lattice Gas with a Neutralizing Background	4
1.0.2 Chapter 3: Absence of Decay in the Amplitude of Pair Distribution Functions at Large Distances . . . . .	5
1.0.3 Chapter 4: Quantum Correction to the Molecular Pair Distribution Function Calculated Classically . . . . .	6
<b>2 Charged Lattice Gas with a Neutralizing Background</b>	<b>7</b>
2.1 Introduction . . . . .	7
2.2 Model . . . . .	11
2.3 Monte Carlo Method for Simulations of the System . . . . .	14
2.4 Linear Chain . . . . .	20

241

242

243

244

245

246  
at Lar

247

248

2.4.1	Nearest Neighbors Interaction . . . . .	20
2.4.2	Finite Range of Interaction . . . . .	25
2.4.3	Infinite Range Coulomb Interaction . . . . .	30
2.5	Triangular Lattice . . . . .	33
2.6	Conclusion . . . . .	40
<b>3</b>	<b>Absence of Decay in the Amplitude of Pair Distribution Functions at Large Distances</b>	<b>42</b>
3.1	Introduction . . . . .	42
3.2	PDF in d-Dimensional Space . . . . .	50
3.2.1	Continuous Definition of PDF . . . . .	50
3.2.2	Definition of PDF Through Bins . . . . .	52
3.3	Random Case . . . . .	54
3.4	Random Case with Excluded Volume . . . . .	57
3.4.1	General Discussion . . . . .	57
3.4.2	Results of Simulations in 2d . . . . .	60
3.4.3	Results of Simulations in 3d . . . . .	63
3.5	Crystals . . . . .	66
3.5.1	General Discussion . . . . .	66
3.5.2	Exact Solution for 1d Crystal . . . . .	70
3.5.3	Results of Simulations in 2d . . . . .	72
3.5.4	Results of Simulations in 3d . . . . .	76



2.1

3.1

3.1

3.1

3.1

4. Quant  
classi

4.1

4.2

4.3

3.5.5	Speculations on the Origin of $\sigma$ -Divergence. . . . .	78
3.5.6	Order and Disorder. Similarities and Differences. . . . .	80
3.5.7	The Role of the Spherical Geometry. . . . .	81
3.6	Perfect $S(q)$ . . . . .	84
3.7	Conclusion . . . . .	86
4	<b>Quantum correction to the Pair Distribution Function calculated classically.</b>	<b>87</b>
4.1	Introduction . . . . .	87
4.2	Pair Distribution Function for a single molecule . . . . .	91
4.3	An example of Morse potential. The idea of the method. . . . .	92
4.3.1	Molecule $N_2$ . . . . .	100
4.3.2	Correction to the heat capacity . . . . .	106
4.4	Vibrations of large molecules . . . . .	112
4.5	TINKER package for molecular modelling and the $C_6H_{14}$ molecule . .	116
4.6	Calculation of PDF for $C_6H_{14}$ molecule . . . . .	119
4.6.1	Low temperatures . . . . .	119
4.6.2	High temperatures . . . . .	128
4.6.3	Pair Distribution Function from Molecular Vibrations and Partial PDFs. . . . .	133
4.6.4	Correction to the Heat Capacity for $C_6H_{14}$ molecule . . . . .	139
4.7	Conclusion . . . . .	142

Summary

1. Chapter

2. Bibliography

3. Question

Appendices

4. Behavior

A. R.

B.

<b>5 Summary</b>	<b>143</b>
5.1 Charged lattice gas with a neutralizing background . . . . .	143
5.2 Behavior of the PDF at large distances . . . . .	144
5.3 Quantum corrections for the PDF calculated classically . . . . .	146
<b>Appendices</b>	<b>147</b>
<b>A Behavior of pdf at large distances</b>	<b>147</b>
A.1 Random case in d-dimensions . . . . .	147
A.1.1 Ensemble averaging . . . . .	147
A.1.2 Integral approach. . . . .	149
A.2 Amorphous case in d-dimensions: integral approach . . . . .	153
A.2.1 Difference with the random case from the integral approach: detailed derivation . . . . .	153
A.3 1d crystal . . . . .	155
<b>B Cut-off for the Morse potential</b>	<b>157</b>
<b>Bibliography</b>	<b>159</b>

## List of Tables

2.1	Comparison of energies at special concentrations obtained in simulations on lattices with sample sizes $18 \times 18$ , in the first row, $\sim 30 \times 30$ in the second row and exact values calculated with method of Bonsall and Maradudin in the third row. . . . .	36
4.1	The distances between some atoms in <i>Long</i> and <i>Short</i> conformations. . . . .	118
4.2	Boltzman weights for $C_6H_{14}$ molecule in <i>Long</i> and <i>Short</i> conformations at different temperatures. . . . .	128

## List of Figures

<b>2.1</b>	The sketch of the structure of aluminum substituted nickel layered double hydroxides $\text{Ni}_{1-x}\text{Al}_x(\text{OH})_2(\text{CO}_3)_{x/2} \cdot y\text{H}_2\text{O}$ . . . . .	8
<b>2.2</b>	Dependence of the concentration $\bar{x}$ on MC sweeps at a fixed values of the chemical potential $\mu$ at temperature $(T/J) = 0.08$ for the triangular lattice with $30 \times 30$ sites in the sample. The values of $\mu$ are shown near their corresponding curves. . . . .	16
<b>2.3</b>	Histograms that show distributions of concentrations for the curves from Fig.2.2. Data were collected over 10000 MC sweeps. The sharp peak corresponding to $(\mu/J) = 0.315$ has height 4000. The peak corresponding to $(\mu/J) = 0.606$ has a height 1700. . . . .	19
<b>2.4</b>	Dependence of the chemical potential $\mu$ on the average concentration $\bar{x}$ for the case of a linear chain with interaction limited to nearest neighbors only. The plateaus seen in simulations for $(T/J) = 0.10$ correspond to the regions of phase separation. . . . .	22
<b>2.5</b>	Energy and Helmholtz free energy as functions of the average concentration $\bar{x}$ at temperature $(T/J) = 0.05$ for a linear chain with interaction limited to nearest neighbors only. . . . .	23
<b>2.6</b>	Phase diagram for a linear chain with nearest neighbor interactions. The solid lines indicate the borders of the phase separation regions. The dashed curve shown for $x < 1/2$ only is the spinodal curve. Both curves were obtained with the transfer matrix method. The points on the right show the results of the simulations performed on lattices with different sample sizes. . . . .	24



2.7	The linear chain sample of 120 sites with interactions up to fifth neighbors included at $\bar{x} = 3/8 = 0.375$ and temperature $(T/J) = 0.01$ . The second row from the top is the continuation of the first row and so on. The picture illustrates the tendency of the system to phase separation: in the top row $x \approx 1/2$ , while in the bottom row $x \approx 1/3$ . Separation cannot really occur due to the same background charge at every site of the chain that corresponds to $\bar{x} = 3/8$ . . . . .	26
2.8	Dependence of the energy per site on concentration, at very low temperatures, for the linear chain with interaction extending up to first, second, third, fourth, fifth and sixth neighbors. Points from simulations are plotted on top of the exact solid curves obtained with transfer matrix technique. Dotted curve shows limiting case of infinite range coulomb interaction. . . . .	27
2.9	Energy per site as a function of concentration $\bar{x}$ for a linear chain with Coulomb interactions. The solid curve was obtained by knowing equilibrium structures predicted with the devil's staircase formalism on the lattice sample with 1000 sites. Circles give the results of the MC simulations at low temperature for samples with 180 sites. . . .	29
2.10	Dependence of the chemical potential $\mu$ on concentration $\bar{x}$ for the linear chain with Coulomb interaction in the region $\bar{x} > 1/2$ . The solid line shows the limit of zero temperature obtained from the energy curve on Fig.2.9. The inset shows the results from the lattice sample with 960 sites at very low temperatures in the whole range $0 < \bar{x} < 1$ . . . .	30
2.11	Phase diagram for the linear chain with Coulomb interactions in the region $x > 1/2$ obtained from MC simulations. . . . .	31
2.12	Energy per site as a function of concentration $\bar{x}$ for the triangular lattice with Coulomb interactions. The solid curve connects the points obtained by simulations in previous work[1]. Dashed vertical lines give the position of concentrations that are stable in MC simulations at very low temperatures. . . . .	34
2.13	Ground state configurations for the triangular lattice with Coulomb interaction for $x = 1/2, 3/5, 2/3$ , and $3/4$ . . . . .	35
2.14	Lattice structures obtained from simulations at three different values of $\mu$ at $(T/J) = 0.01$ . Concentrations of black ions are close to $x = 1/2 = 0.5$ , $x = 3/5 = 0.6$ , $x = 6/7 \simeq 0.857$ for the pictures from left to right. . . . .	36



2.15	Dependence of chemical potential $\mu$ on concentration $\bar{x}$ for the triangular lattice with Coulomb interaction. For the cases of temperatures $(T/J) = 0.2$ and $(T/J) = 0.1$ the size of the sample was $9 \times 9$ and no points are shown since their density is high. . . . .	37
2.16	Phase diagram for the triangular lattice with Coulomb interaction in the region $x > 1/2$ obtained with MC simulations. . . . .	40
3.1	Experimental $F(q)$ and $G(r)$ of Ni at 15K measured by neutron scattering. . . . .	45
3.2	Only those sites contribute to the value of $G_i(r)$ that are in $\sigma$ vicinity of the distance $r$ with respect to site $i$ . . . . .	46
3.3	PDF of Ni at 15K at different distances. The blue solid lines are results of calculations while the red dotted lines on the two panels on top show the result of neutron scattering experiment taken from Fig. 3.1 . . . .	48
3.4	PDF for the amorphous Si: $a_o \simeq 2.4 \text{ \AA}$ , $\sigma = 0.1 \text{ \AA}$ . A: with respect to 1 atom, B: averaged over 10 atoms, C: averaged over 20000 atoms. . .	49
3.5	PDF calculated for a square lattice $\sigma = 0.1a$ according to definitions through bins (blue lines) and Gaussians (red lines). Fig.3.1 . . . . .	53
3.6	Scaled PDF function $g_{3i}(r) \equiv G_{3i} \sqrt{\sigma/\rho_o}$ vs. reduced distance $r/\sigma$ . .	55
3.7	Distributions of points for two different excluded distances. The left figure shows distribution that was obtained by choosing excluded distance in such a way that excluded area covers 1/4 of the total area. In the right figure, excluded area covers 1/2 of the total area. . . . .	57
3.8	Only those points that are in $\sigma$ vicinity of the distance $r$ with respect to site $i$ contribute to the value of $G_i(r)$ . Excluded volume around every point reduces the volume accessible to the other points, that may want to enter the annulus due to fluctuations, and thus reduces the size of fluctuations in the number of points. . . . .	58

VI. Dependent  
variables  
and  
control  
variables  
in  
the  
model

VI. Dependent  
variables  
and  
control  
variables  
in  
the  
model

3.9	Dependence of $g_{2i}^2(E)$ and $g_{2i}^2(G)$ on $\sigma$ for configurations with different excluded volumes. For the curves (with circles) shown, excluded volume covers 0.05 , 0.10, 0.20 and 0.525 of the total area of the box. The curve with squares corresponds to the amorphous distribution of sites. It basically coincides with the curve that has the fraction of excluded volume 0.525. The curve with triangles corresponds to completely random distribution. . . . .	61
3.10	Dependence of the slope (linear part) of the curves $g_{2i}^2$ versus $\sigma$ (see Fig.3.9) on excluded volume. The value of excluded volume 0.525 is very close to the limiting accessible value. The inset shows how the ratio of the asymptotic value (large $\sigma/\lambda$ ) of $g_{2i}^2$ to the value of $g_{2i}^2$ for the random case depends on excluded volume. Note the scale on the $y$ -axis. . . . .	62
3.11	Dependence of $g_{3i}^2(E)$ and $g_{3i}^2(G)$ on $\sigma$ for configurations with different excluded volumes. For the curves (with circles) shown, excluded volume covers 0.02, 0.05 , 0.10, 0.20 and 0.30 of the total volume of the box. The curve with squares corresponds to the distribution of sites in amorphous Si. It basically coincides with the curve that has the fraction of excluded volume 0.35 (not shown). The curve with triangles corresponds to completely random distribution. . . . .	64
3.12	Dependence of the slope (linear part) of the curves $g_{2i}^2$ versus $\sigma$ (see Fig.3.11) on excluded volume. The value of excluded volume 0.525 is very close to the limiting accessible value. The inset shows how the ratio of the asymptotic value (large $\sigma/\lambda$ ) of $g_{2i}^2$ to the value of $g_{2i}^2$ for the random case depends on excluded volume. . . . .	65
3.13	Illustration for the Gauss's circle problem. Sites that lie inside of the circle of radius $r$ shown as black filled circles, while sites that lie outside of the circle of radius $r$ as open circles. Only those sites contribute to the value of $G_i(r)$ that are in $\sigma$ vicinity of the distance $r$ with respect to site $i$ . . . . .	67
3.14	Figure shows the dependence of the ratio $g_{1L}^2(\sigma)/g_{1R}^2(\sigma)$ on $\sigma$ . At small values of $\sigma$ , when different peaks in $G(r)$ do not overlap, this ratio linearly decreases as $\sigma$ increases. As peaks start to overlap (large values of $\sigma$ ), the rate of decay in the average amplitude of PDF decreases.	71

- 3.15 Inset shows how  $F(r)$  depends on  $r$  for  $r \in (0; 1000)a$ ,  $r \in (9000; 10,000)a$  and  $r \in (99,000; 100,000)a$ . It shows that on average amplitude of oscillations in  $F(r)$  does not depend on  $r$ . At least, it is impossible to see it by eye. The dashed curve on the main figure shows how  $\langle F^2(r) \rangle$  averaged over few intervals of  $r$  of length  $1000a$  depends on the position of the averaging interval. At the beginning and at the end of every averaging interval circles are plotted. . . . . 73
- 3.16 Dependencies of  $g_2^2(L)/g_2^2(R)$  on  $\sigma/\lambda$  for triangular and square lattices. Triangles and squares represent the results of numerical calculations for triangular and square lattice respectively. The solid fitting curves are given by formulas  $g_2^2(tri)/g_2^2(R) = 2.483(\sigma/\lambda)^{-1/3} - 18.264(\sigma/\lambda)$  for triangular lattice and  $g_2^2(sqr)/g_2^2(R) = 1.849(\sigma/\lambda)^{-1/3} - 14.478(\sigma/\lambda)$  for square lattice. Dashed lines highlight the effect of excluded volume. Expressions for them are given by the first divergent term in the formulas for the solid curves. They do not contain the second term (that might be) caused by excluded volume. From the figure, it follows that the effect of the excluded volume is bigger for triangular lattice than for square lattice. . . . . 74
- 3.17 Results of numerical simulations for FCC and orthorhombic lattices. For rectangular lattice  $b/a = 2$  and  $c/a = 3$ . Points represent results of simulations. Solid fitting curves are given by formulas described in the text. Dashed lines highlight the effect of excluded volume. Expressions for them are given by the first divergent term in the formulas for the solid curves. Thus they do not contain the second term (that might be) caused by excluded volume. It can be seen from the figure that the effect of excluded volume is bigger for FCC lattice than for orthorhombic lattice. . . . . 77
- 3.18 Triangular or square PDFs can be defined through triangular or square densities, i.e. by counting the number of points inside triangular or square annulus and dividing this number by the area of the annulus. 82
- 3.19 Dependence of  $\rho_{tri} - \rho_o$  on distance  $r/a$  for triangular PDF on square lattice. Since the amplitudes of oscillation persist as distance increases the figure demonstrates that the use of the polygons (any polygon can be divided into triangles) instead of the circle changes the way in which PDF should be defined. . . . . 83
- 3.20 Reduced scattering intensity obtained by Fourier transformation from PDF calculated for the values of lattice parameters similar to those for the Ni crystal at 20K and 300K:  $a \simeq 3.53\text{\AA}$ ,  $\sigma_{20} = 0.05\text{\AA}$  and  $\sigma_{300} = 0.1\text{\AA}$ . 84

4.1	The blue curve shows the Morse potential for the $N_2$ molecule. The red curve shows the harmonic approximation to the Morse potential at small values of $x$ . The blue and red horizontal lines are the energy levels for the Morse and harmonic potentials respectively. . . . .	96
4.2	The squares of the wave functions of the Morse potential for the $N_2$ molecule. The little figures on the left from the top to the bottom show normalized wave functions for $n = 0, 1, 2, 3, 7$ . The figures on the right from the top to the bottom show normalized wave functions for $n = 10, 20, 30, 40, 50$ . There are 61 energy levels for the chosen values of parameters. . . . .	99
4.3	The Pair Distribution Functions or the probabilities to find the particle at a given distance in the Morse potential or its harmonic approximation at temperatures 100K, 1000K, 2000K and 10,000K. The red and orange curves represent QM (4.24,4.25) and CM (4.13,4.14) results for the Morse potential. The blue and green curves represent QM and CM results for the harmonic approximation to the Morse potential. The black curves represent CM results for the Morse potential corrected by the convolution (4.34) with $\sigma_{corr}^2$ obtained from the harmonic approximation to the Morse potential. . . . .	101
4.4	The dependencies of $\sigma^2$ on temperature $T$ that were calculated in four different ways. The red and orange curves show QM (4.24, 4.25, 4.28) and CM (4.13, 4.14, 4.17) results for the Morse potential. The blue and green curves show QM (4.9) and CM (4.12) results for the harmonic approximation to the Morse potential. The black curve shows the CM results on the Morse potential with correction (4.31) that comes from the harmonic approximation to the Morse potential. . . . .	103
4.5	Average energies for a particle in the Morse potential and its harmonic approximation as a function of temperature. The red and orange curves represent the QM and CM solution for the Morse potential. The blue and green (dashed) curves show the QM and CM solutions for the harmonic approximation to the Morse potential. The black dashed curve shows the CM solution for the Morse potential with correction (4.31) that comes from the harmonic approximation to the Morse potential. It is assumed that $U_o = 0$ . . . . .	108

4.6	The dependencies of the heat capacities for the particle in the Morse potential and its harmonic approximation on temperature. The red and orange curves represent QM and CM solutions for the Morse potential. The blue and green (dashed) curves show the QM and CM solutions for the harmonic approximation to the Morse potential. The black dashed curve shows the CM solution for the Morse potential with the correction (4.31) that comes from the harmonic approximation to the Morse potential. All these curves were obtained by the differentiation (4.39) of the corresponding energy curves on Fig.4.5. . . . . .	110
4.7	The sketch of the $C_6H_{14}$ molecule. The carbon atoms are shown as black filled circles. The hydrogen atoms are shown as open circles. The numeration of the atoms coincides with those used in the Fig.4.9 and Fig.4.10,4.11,4.12 . . . . .	117
4.8	The geometry of the $C_6H_{14}$ molecule in <i>Long</i> conformation. . . . .	118
4.9	The probability for finding a particular pair of atoms at a given distance at temperatures 150K on the left and at 500K on the right. The blue curves were obtained from the classical MD trajectories. The red curves result from the convolution of the blue curves with the corresponding correction Gaussian. Every pair of atoms has its own $\sigma_{corr}^2(T)$ . . . . .	120
4.10	The dependencies of the average distances between some pairs of atoms on temperature obtained from MD simulations. In the beginning of every MD run (at a particular temperature) the molecule was always in equilibrium <i>Long</i> conformation. At low temperatures these distances only slightly depend on temperature, as molecule remains in the <i>Long</i> conformation. As temperature increases instantaneous distance between a pair of atoms can have significantly different values that occur when the molecule can be in different conformations (or identical atoms interchange their positions). Thus, as temperature increases, there occur sharp changes in the average distances for some pairs of atoms. . . . .	121
4.11	The dependencies of $\sigma^2$ on temperature $T$ for some pairs of atoms. The orange triangles show the results obtained from MD simulations, the blue and green curves show the QM and CM results obtained from the eigenfrequencies and eigenvectors of molecular vibrations. The red circles show the MD results corrected by adding to the orange triangles the difference between the blue and green curves. . . . .	122

4.12	The dependencies of $\sigma^2$ on temperature $T$ for some pairs of atoms. The orange triangles show the results obtained from MD simulations, the blue and green curves show the QM and CM results obtained from the eigenfrequencies and eigenvectors of molecular vibrations. The red circles show the MD results corrected by adding to the orange triangles the difference between the blue and green curves. . . . .	123
4.13	PDF for the $C_6H_{14}$ molecule in <i>Long</i> conformation at low temperatures. The brown curves show the results of MD simulations before the correction is applied. The blue curves show the results of MD simulations corrected by convolution (4.33, 4.34). . . . .	125
4.14	The blue and green solid curves show total corrected PDFs for the molecule in <i>Long</i> and <i>Short</i> conformations. The red dashed curve shows Boltzman combination (4.70) of PDFs from <i>Long</i> and <i>Short</i> conformations. At all temperatures when the molecules remains in one or another conformation the combined PDF basically coincides with PDF in <i>Long</i> conformation due to the values of the Boltzman weights. . . .	127
4.15	The brown curves on both figures show MD results obtained on the <i>Long</i> (top) and <i>Short</i> (bottom) conformations. The figure on top also shows the corrected PDFs obtained by the correction of MD results from the <i>Long</i> conformation with the set of $\sigma_{corr}$ from the <i>Long</i> (the blue solid curve) and <i>Short</i> (the red dashed curve) conformations. The bottom figure also shows the PDFs obtained by the correction of MD results from the <i>Short</i> conformation with the sets of $\sigma_{corr}$ from <i>Short</i> (blue solid curve) and <i>Long</i> (red dashed curve) conformations. . . . .	130
4.16	Corrected PDFs for the $C_6H_{14}$ molecule at different temperatures. The inset shows the region between 3 Å and 6.5 Å on a bigger scale. . . .	132
4.17	The panel on top shows PDFs with respect to carbon atom number 1 created by the other carbon atoms only at 298K. Blue and green curves were obtained from molecule in <i>Long</i> and <i>Short</i> conformations correspondingly. The widths of peaks were calculated in QM approach using eigenfrequencies and eigenvectors of molecular vibrations. As distance increases there are peaks that correspond to the carbon atoms number 2, 3, 4, 5 and 6. The red curve is a linear combination of blue and green curves with corresponding Boltzman weights. The red curve in the bottom panel is the same as the red curve in the top panel. The grey curve, that also shows PDF with respect to the carbon atom number 1 due to the other carbon atoms, was obtained from MD simulations. The black curve was obtained from the grey curve using our correction scheme. . . . .	134





- 4.18 The top panel shows partial PDFs with respect to the carbon atom number 1 calculated for the molecule in *Long* conformation from eigenfrequencies and eigenvectors of molecular vibrations in the QM approach. The blue curve shows partial PDF due to the other carbon atoms only (hydrogen atoms are ignored). The red curve is due to all the other atoms (carbons and hydrogens). Thus, the difference between two curves is due to the hydrogen atoms. The bottom panel shows the same curves as the top panel, but for the molecule in *Short* conformation. . . . . 135
- 4.19 The top panel shows partial PDFs with respect to the carbon atom number 1 created by all other atoms (carbons and hydrogens). The blue and green curves were calculated from eigenfrequencies and eigenvectors of molecular vibrations in *Long* and *Short* conformations correspondingly. The red curve is the linear combination of the blue and green curves with corresponding Boltzman weights. The red curve in the bottom panel is the same as the red curve in the top panel. The grey curve was extracted from MD simulations in which transitions between conformations occur. The black curve was obtained from the grey curve using our correction method. . . . . 136
- 4.20 The blue and green curves in the top panel were calculated from eigenfrequencies and eigenvectors of molecular vibrations for the molecule in *Long* and *Short* conformations correspondingly. They show the total PDFs of the molecule. The red curve is a linear combination of the blue and green curves with corresponding Boltzman weights ( $w_L(T) = 0.79$  and  $w_S(T) = 0.21$ ). The red curve in the bottom panel is the same as the red curve in the top panel. The grey curve, that also shows the total PDF of the molecule, was obtained from MD simulations. The black curve was obtained from the grey curve using our correction/convolution method. . . . . 137
- 4.21 The blue and green curves in the top panel were calculated from eigenfrequencies and eigenvectors of molecular vibrations for the molecule in *Long* and *Short* conformations correspondingly. They show the total PDFs of the molecule. The red curve is a linear combination of the blue and green curves with corresponding Boltzman weights ( $w_L(T) = 0.62$  and  $w_S(T) = 0.38$ ). The red curve in the bottom panel is the same as the red curve in the top panel. The grey curve, that also shows the total PDF of the molecule, was obtained from MD simulations. The black curve was obtained from the grey curve using our correction/convolution method. . . . . 138

4.22	The dependencies of the energy and the heat capacity on temperature for the $C_6H_{14}$ molecule. Blue and green curves represent the QM and CM results for the harmonic approximation to the real potential. The orange curves and circles represent the result of the MD simulations. The red curves and circles show the corrected MD results. See more detailed description of the figure in the text. . . . .	140
B.1	Dependencies of $\sigma_{MCM}^2(T)$ on temperature (see Fig.4.4) for different values of the upper cut off in the integrals (4.14, 4.17). Thus, if $T \leq 10000$ (K) any cut-off in the interval (1.5:3.0) Å would lead to basically the same result. The inset shows how $\langle U_{MCM}(T) \rangle$ (in temperature units) depends on temperature. Thus for the potential energy any upper cut off (see (4.38)) in the interval (1.5:3.0) Å is also suitable. . .	158

# Chapter 1

## Introduction

During my Ph.D. years I was working on several different projects all in the area of computational/theoretical condensed matter physics. Thus, it is somewhat difficult to write an introduction to the thesis because, as it seems to me, it should unite all these different projects under the roof of one idea. But it is hard to unite things that are different. It also means that an introduction, if it has to be written, should be rather general. So let it be...

Any object in this world interacts in one way or another with other objects. In fact we know that an object exists from the way it interacts with us or from the way its footsteps interact with us. Thus, objects are distinguished by their interactions. Due to the interactions things in the world become organized. Thus, there are three words: existence, interaction and organization that from my point of view, are inseparable in nature and as follows in the essence of all sciences.

Generally speaking, all different sciences addresses the same questions: which objects exist, how they interact with each other and how objects are organized. We learn about the objects from the way they interact with each other and from the way they are organized. Almost always when we want to learn about an object we artificially put it in conditions that will reveal its ability to interact in one way

or another; i.e., reveal its properties. In other words we do experiments. On the other hand, if we know about interactions, we use this knowledge to construct more complicated objects or to predict the behavior of more complicated objects in some new situation. For example, if the interaction between two masses is known, the structures of solar systems and galaxies can be predicted.

May be the last statements are not true with respect to all sciences-there are so many that I cannot think about all of them. But it seems to be true in sciences like physics, chemistry, biology and sciences that are directly related to them, like microbiology. Mathematics is somewhat different, because at first it states the existence of different objects, like points, lines, angles. Then it establishes interactions between them - axioms. From these objects and interactions more complicated objects and relations between them are constructed-theorems. Thus, from this point of view, these three words are also applicable to mathematics.

All objects are immersed in space or space contains all the objects. It also allows objects to interact with each other. Often, while studying properties of different objects, we do not pay attention to the space in which they are immersed. However properties of the space and properties of the objects in space are as inseparable as those three words. Thus, by learning about the objects we also learn about the space.

One of the properties of space that is always involved in the nature of interactions and motion of objects is the dimensionality of space. Everyday observations of this world suggest that it is 3-dimensional. Thus, in order to describe the position of an object in space we need 3 real numbers:  $x$ ,  $y$ ,  $z$ . However, often there is no need to use all three coordinates. Thus, in order to find our location in the city we do not need all three coordinates- two is enough. Because of it most city maps do not contain information about the height of a particular city point with respect to sea level. The Properties of complex objects, even if they are constructed from objects with very simple interactions between them, can be rather complicated. These properties can

also drastically depend on the dimensionality of space, as in Ising model in which features of phase transitions are different in different dimensions.

Evolution of sciences is basically the development of ideas and tools that are used to study objects, to model their properties and to construct new objects.

From this extremely general point of view my thesis can be separated into two parts.

The first part is devoted to the modeling of properties of an object that consists of many objects with simple known interactions between them (Chapter 2).

The second part is about a particular technique that is being used to study the properties of complex objects: the ordering and interactions of simple objects from which these complex objects are constructed. This second part, in its turn, can be divided into smaller pieces.

Although this technique was used to study ordering of objects and their properties for almost a hundred years, it turns out that it has some properties, related to the general properties of space, that never were carefully discussed. The results of the study of these properties are presented in chapter 3.

Footsteps of more complicated objects sometimes are rather complicated. Thus, it order to extract information about them from their footsteps it might be necessary to model the possible footsteps. To the modeling of these footsteps, in the frame of a particular technique that is used to study objects properties, chapter 4 of this thesis is devoted.

Since, as it was written in the very beginning, I was working on several almost independent projects, it is natural to write introduction for every project independently. Thus, every chapter in this thesis is about a particular project, it has its own introduction that explains the motivation for this research project, describes directions of the investigation and methods that were used in the study. In the remaining part of this introduction there are short descriptions of every project/chapter with

the summaries of the main results.

### 1.0.1 Chapter 2: Charged Lattice Gas with a Neutralizing Background

In this part of my thesis we consider a model that was first introduced by Y.Xiao, M.F. Thorpe and J.B. Parkinson in [1] to describe the ordering of two different types of positive ions in the metal planes of layered double hydroxides  $\text{Ni}_{1-x}\text{Al}_x(\text{OH})_2(\text{CO}_3)_{x/2} \cdot y\text{H}_2\text{O}$ . The ordering is assumed to occur due to long-range Coulomb interactions, and overall charge neutrality is provided by a negative background representing the hydroxide planes and  $\text{CO}_3^{2-}$  anions. The previous study [1] was restricted to the ground state properties. Here we use a Monte Carlo technique to extend the study to finite temperatures. The model predicts that at some values of the concentration  $x$ , the system can exhibit an instability and phase separate. In order to evaluate the precision of these Monte Carlo procedures, we first study a linear chain with finite ranged interactions where exact solutions can be obtained using a transfer matrix method. For a linear chain with infinite-ranged interactions, we use a devil's staircase formalism to obtain the dependence of the energy of the equilibrium configurations on  $x$ . Finally we study the two dimensional triangular lattice using the same Monte Carlo techniques. In spite of its simplicity, the model predicts multiple first order phase transitions. The model can be useful in applications such as the modeling of the ordering of intercalated metal ions in positive electrodes of lithium batteries or in graphite. The obtained results were published in Phys.Rev.B [2] and the text in this chapter is basically identical to the text in this publication.

## 1.0.2 Chapter 3: Absence of Decay in the Amplitude of Pair Distribution Functions at Large Distances

In this chapter the behavior of pair distribution function (PDF) at large distances is addressed. Traditionally the PDF, that can be obtained from the Fourier transform of powder diffraction data, was used to describe short-range correlations in atomic positions. Amplitudes of peaks in experimental PDF decay as distance increases. Thus, it was always assumed that the PDF at large distances is featureless. Puzzled by the observation that PDF calculated for crystalline materials does not decay at large distances, if instrumental resolution is ignored, we studied the behavior of PDF at very large distances. To the best of our knowledge, the origin of the PDF decay at large distances has never been carefully discussed. It turns out, surprisingly, that the increase in the number of neighbors at large distances does not lead to the decay of the PDF independently from the type of the material. In other words, the PDF calculated with respect to one atom does not decay at large distances not only for the crystalline, but also for amorphous materials. We find that this behavior in amorphous materials is caused by random fluctuations in the radial number density. Thus PDF in amorphous materials decays due to ensemble averaging over different central atoms. We achieve an accurate quantitative description of fluctuations for the case when atoms are distributed randomly in space. Differences with the amorphous case are discussed. The case of perfect, single component, crystals is the most interesting because in it all atomic positions are equivalent and there is no need to average over different atoms. Thus total measurable PDF for perfect crystals does not decay at large distances if instrumental resolution is ignored. However, the origin of this behavior in crystals is significantly more complicated. It turns out that this behavior of the PDF is related to the still unsolved problem that C.F. Gauss formulated more than a hundred fifty years ago and that has give rise to the whole area in mathematics called lattice point theory. Further investigation of this case is obviously needed. For

generality we discuss the case of the PDF in d-dimensional space. Our results can be used to measure the amount of dislocations in crystalline materials and to test instrumental resolution in scattering experiments.

### **1.0.3 Chapter 4: Quantum Correction to the Molecular Pair Distribution Function Calculated Classically**

In this chapter we present some ideas and the developed technique that may significantly improve precision of PDF calculations for complex molecules. This technique allows, in particular, the incorporation of the purely quantum effect of zero-point motion into the pair distribution function calculated classically for molecules using Monte Carlo or Molecular Dynamics simulations. This correction may significantly improve agreement between modeled and experimental data, especially at small distances. Thus it may allow more definite conclusions about inter- and intramolecular motion, including flexibility, and also about mutual orientations of different molecules.



# Chapter 2

## Charged Lattice Gas with a Neutralizing Background

### 2.1 Introduction

This chapter is devoted to the study of a model that was introduced earlier[1] by Y.Xiao, M.F. Thorpe and J.B. Parkinson, to describe the possible ordering of metal ions that can occur in aluminum substituted nickel layered double hydroxides  $\text{Ni}_{1-x}\text{Al}_x(\text{OH})_2(\text{CO}_3)_{x/2} \cdot y\text{H}_2\text{O}$ [3, 4, 5, 6, 7].

The Ni ions in  $\text{Ni}(\text{OH})_2$  occupy the octahedral holes between alternate pairs of OH planes and thus form a triangular lattice identical to that adopted by the OH ions, as shown on Fig.2.1. The two planes of OH ions, with the plane of Ni atoms between them, form a brucite like layer of the host structure[8].

$\text{Ni}(\text{OH})_2$  can exist in two polymorphous crystal structures denoted as  $\alpha$  and  $\beta$ . Both structures consist of brucite-like layers, that are well ordered in the  $\beta$ -phase and randomly stacked in the  $\alpha$ -phase. The interlayer spacing (gallery) in the  $\alpha$ -phase usually is significantly larger than in the  $\beta$ -phase due to the large number of water molecules and anionic species that can penetrate into the galleries[9].

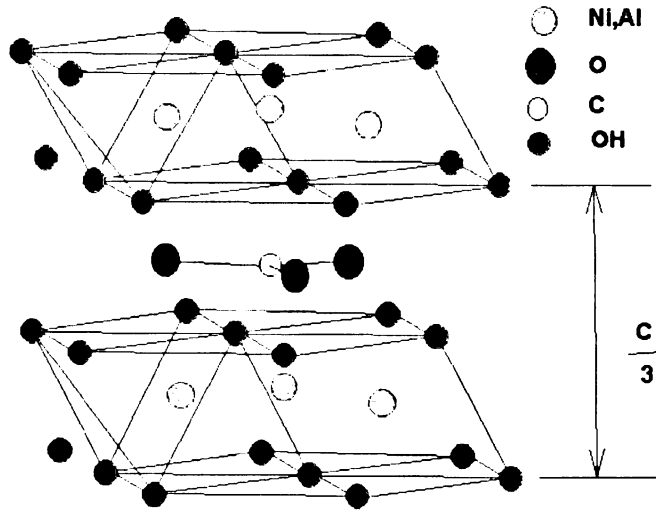
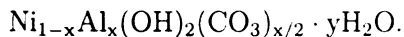


Figure 2.1: The sketch of the structure of aluminum substituted nickel layered double hydroxides  $\text{Ni}_{1-x}\text{Al}_x(\text{OH})_2(\text{CO}_3)_{x/2} \cdot y\text{H}_2\text{O}$

Nickel hydroxide  $\text{Ni}(\text{OH})_2$  in the  $\beta$ -phase has been extensively used as a material for the positive electrode in rechargeable alkaline batteries[10]. However it has been shown that electrodes based on the  $\alpha$ -phase hydroxide have a bigger charge capacity, lower charge and higher discharge voltages [11, 12]. Unfortunately the  $\alpha$ -phase reverts to the  $\beta$ -phase in the alkaline media (KOH-for example) which is used in batteries. Thus the stabilization of the  $\alpha$ -phase of  $\text{Ni}(\text{OH})_2$  in an alkaline media is an important goal for potential applications. To enhance the  $\text{Ni}(\text{OH})_2$  stability many studies of the partial substitution of metal ions (Al-for example) for Ni in the lattice of nickel hydroxide have been carried out [13, 14, 15, 16].

When  $\text{Ni}^{2+}$  ions are substituted by  $\text{Al}^{3+}$  ions in the metal sheets,  $[\text{CO}_3]^{2-}$  anions accumulate in the galleries in such an amount that total charge neutrality is preserved. The amount of water in the galleries depends on the preparation method: the general formula of the aluminum substituted layered nickel hydroxide is



It is natural to expect that the stability of these compounds is composition dependent and also depends on the preparation technique. Different authors were able to synthesize layered hydroxides with different concentrations of aluminum. In particular the range  $0 \leq x \leq 0.4$  has been reported [8]. Not all ranges of composition  $x$  are accessible due to the limited number of  $[\text{CO}_3]^{2-}$  ions and water molecules that can penetrate into the gallery.

Possible orderings of the Ni and Al ions in the metal planes can also affect the stability of the compound. Several authors have reported observations of in-plane ordering of metal ions [3, 4, 5, 6, 7]. Ordering of ions was observed near the values of  $x$  equal to 1/4 and 1/3 that are in registry with the host geometry of triangular lattice. However, it seems that there are no detailed experimental studies of the ordering as a function of composition  $x$ .

The ordering of metal ions in alloys is often considered within the framework of a lattice gas model where only interactions between neighbors that are not separated by large distances is taken into account because of the relatively short screening length [17, 18, 19] caused by free electrons.

It is generally accepted that in layered hydroxides the Coulomb interaction between positively charged metal planes, negatively charged hydroxide planes and negatively charged anions  $[\text{CO}_3]^{2-}$  in the galleries are important. The screening length in layered hydroxides should be significantly larger than in metal alloys, because dielectric screening caused by water and other polar molecules is weaker than screening caused by free electrons. Thus a model that takes into account long range Coulomb interaction and interaction between positive metal ions in the plane with negative hydroxides layers and negative anions in the galleries might be more suitable than a lattice gas model to describe the ordering of metal ions in layered double hydroxides. The role of ordering due to Coulomb interactions has been discussed previously by

Thompson[20].

We have previously suggested a simple model to describe the ordering of metal ions in layered hydroxides[1]. In this model two kinds of positively charged metal ions occupy the sites of a triangular lattice. The lattice is immersed in a negatively charged background which represents the hydroxide layers and negative anions in the galleries. It was assumed that the background charge is the same at every site of the triangular lattice. Thus the total charge at every site is formed by the positive charge due to the metal ion and the negative background charge. The interaction potential between sites was assumed to be a long ranged  $1/r$  Coulomb type.

In the previous work[1] the dependence of the ground state energy of this model system on the concentration of Al was studied assuming a homogeneous concentration of metal ions in the plane. Equilibrium ordering configurations of ions that can occur at each concentration in the range  $0 \leq x \leq 1$  were calculated and compared with corresponding X-ray diffraction patterns.

In this study a new interpretation of the previous results is suggested. It will be shown that at some concentrations  $x$  the system is unstable with respect to phase separation into phases with concentrations  $x_1$  and  $x_2$  such that  $x_1 < x < x_2$ . The phase diagram of the system is calculated in the  $(T, x)$  plane using the grand canonical ensemble by introducing a chemical potential  $\mu$ . In the case of the layered hydroxides, the chemical potential under consideration is not related to the voltage on the electrodes and represents only a useful way to obtain the phase diagram.

The model is quite general and can be employed to describe ordering and first order phase transitions in ionic systems with long range interactions. It may have some application to the ordering of intercalated Li ions in rechargeable Li-batteries [20, 21, 22]. Predicted phase separations can lead to the staging when homogenous planes with different concentrations of metal ions will form. In plane long range interaction in this case can be similar to that occurring in staged graphite intercalation



compounds[23, 24].

The chapter is organized as follows. In section 2.2 the model is defined. Then in section 2.3 the discussion of the details of the Monte Carlo (MC) method that was used to obtain the phase diagrams is presented. Section 2.4 describes an application of the method to the linear chain. Subsections 2.4.1 and 2.4.2 are devoted to the case of finite ranges of interaction where an exact solution can be obtained using *transfer matrix* techniques. The case of a linear chain with infinite range Coulomb interaction, in which the energies of equilibrium configurations can be calculated exactly using the *devil's staircase* method, is discussed in subsection 2.4.3. Finally in section 2.5 the case of the two dimensional triangular lattice is studied. Results are summarized in the conclusion.

## 2.2 Model

Consider a system composed of two types of positive ions which occupy the sites of some lattice. Every site of the lattice is occupied either by a *black* ion with charge  $Q_b$  or by a *white* ion with charge  $Q_w$ . The concentration of black ions is  $x$  and the concentration of white ions is  $1 - x$ . In addition to these two types of positive ions there is also a negative compensating uniform background charge  $q$ , at every site of the lattice, that ensures charge neutrality in the system. Hence at any site  $i$  a total charge is equal to either  $\Delta_b = Q_b + q$  or  $\Delta_w = Q_w + q$ . The Hamiltonian of the system of charges can be written in terms of the pairwise interactions  $V_{ij}$ :

$$H = \sum_{i < j} V_{ij} \Delta_i \Delta_j. \quad (2.1)$$

For the Coulomb interaction  $V_{ij} = 1/R_{ij}$ , where  $R_{ij}$  is the distance between sites  $i$  and  $j$ . In the following the case of truncated Coulomb interaction, for which there is interaction only between neighbors that are in some range, also will be considered.

The value of the background charge depends on the values of  $Q_b, Q_w$  and on the concentrations of those ions. The average charge per site due to the positive ions is

$$\bar{q} = xQ_b + (1 - x)Q_w. \quad (2.2)$$

The value of the charge that provides the uniform background with overall charge neutrality is then given by  $q = -\bar{q}$ . Thus  $\Delta_b = Q_b + q = (Q_b - Q_w)(1 - x)$  and  $\Delta_w = Q_w + q = (Q_b - Q_w)(-x)$ . Introducing  $J_{ij} = V_{ij}(Q_b - Q_w)^2$  we rewrite Eq. (2.1) as:

$$H = \sum_{i < j} J_{ij} (n_i - x)(n_j - x). \quad (2.3)$$

where  $n_i = 1$  if site  $i$  is occupied by a black ion and  $n_i = 0$  if site  $i$  is occupied by white ion. Thus the precise values of the positive charges do not change the general properties of the model. From Eq. (2.3) follows that at a fixed concentration  $x$

$$H = \sum_{i < j} J_{ij} n_i n_j - x^2 \sum_{i < j} J_{ij}. \quad (2.4)$$

Thus at fixed concentration the model is essentially a lattice gas model because in this case the second term in Eq. (2.4) is the same for all configurations of ions. This term is due to the neutralizing background and cancels the divergence of the energy associated with the Coulomb repulsion when the interactions are of infinite range.

It is easy to estimate the values of the constants  $J_{ij}$  if the lattice constant and charges  $Q_b$  and  $Q_w$  are known. For the aluminium substituted nickel layered double hydroxide  $a = 3.032 \text{ \AA}$  [8],  $Q_b = 3e$  and  $Q_w = 2e$ . For the nearest neighbors we have:

$$J = V_{nn}(Q_b - Q_w)^2 = \frac{e^2}{\epsilon a}. \quad (2.5)$$

Thus if we use a dielectric constant appropriate for water  $\epsilon = 80$ , then  $J \simeq 60 \text{ meV}$  or about 500 K. Short range screening, due to the presence of water and other ions,

can effectively decrease the values of the  $J_{ij}$ .

In order to use the grand canonical ensemble to study the equilibrium properties of this system of charges a chemical potential term  $-\mu \sum_i n_i$  should be added to the Hamiltonian. Now the concentration  $x$  can fluctuate and hence the background charge will also fluctuate. The grand canonical Hamiltonian can be written as:

$$H = \sum_{\langle ij \rangle} J_{ij}(n_i + q)(n_j + q) - \mu \sum_i n_i, \quad (2.6)$$

where  $q$  describes the uniform background charge which is adjusted to be equal to  $q = -\langle n_i \rangle = -x$ .

Although the primary goal is to study the two-dimensional triangular lattice with infinite range Coulomb interactions, it is worth at first to consider the linear chain as an example to gain a better understanding of the model since there are exact analytical methods that can be used in two limiting cases: finite range interactions can be studied exactly using transfer matrix methods [25] and infinite range Coulomb interactions can be described in terms of a Devil's staircase formalism[17]. The study of the linear chain will also give an insight into the precision of the numerical techniques that will be used for the triangular lattice with Coulomb interactions.

In the following sections the following questions are addressed. What is the equilibrium structure of the charges for a given concentration of the ions? How does the equilibrium energy of the system depend on the concentration of the ions? How does the chemical potential depend on the average concentrations of the ions at different temperatures. Do phase transitions occur in the system and what is the phase diagram of the system at finite temperatures?



## 2.3 Monte Carlo Method for Simulations of the System

In Monte Carlo simulations a Metropolis algorithm[26] will be used to accept or reject elementary moves that will be performed on the charges to bring them into an equilibrium configuration. Two different types of moves will be used: *A* interchange the positions of *black* and *white* ions in the lattice. *B* change the *color* of the ion at a particular site.

The simulations can be carried out with either constant values of the concentration or with constant values of the chemical potential. In case of simulations at a constant value of concentration only moves of type *A* were used. In case of simulations at a constant value of the chemical potential both types of moves *A* and *B* were used. The *A*-move does not change the value of the background charge since it does not change the concentration. The *B*-move changes the concentration and thus the background charge has to be changed at every site in the lattice. In order to decide whether to accept or reject the move it is necessary to calculate the energy of the system before and after the move. A lattice of size  $N$  in case of the linear chain and  $N \times M$  for the triangular lattice are considered. Standard periodic boundary conditions are applied with respect to this *central zone*. Thus the central zone occurs in the center of bigger lattice surrounded by *surrounding zones*. In order to calculate the energy of the system we calculate the energy of interaction between all sites inside the central zone and the energy of interaction between the sites in the central zone with sites in all surrounding zones. Since the system is charge neutral, the contribution to the energy from surrounding zones that are far away from the central zone are much smaller than the contribution from surrounding zones that are close to the central zone. In fact, it was found that if  $N$  and  $M$  are of the order of 10, then it is enough to consider the lattice of size  $5N \times 5M$  in order to calculate the energy with

sufficient precision for almost all concentrations. In other parts of this chapter we refer to the size of the central zone as to the sample size, with the periodic boundary conditions described above.

The total energy of the system given by Eq. (2.3) can be separated into three parts which represent interaction between black-black, white-white and black-white sites

$$E = E_{bb} + E_{ww} + E_{bw} . \quad (2.7)$$

It follows from Eq. (2.3) that  $E_{bb}$  can be written as

$$E_{bb} = (1 - x)^2 \sum_{i < j} J_{ij} n_i^b n_j^b . \quad (2.8)$$

In the sum above, the index  $i$  runs over all sites in the *central zone* and the index  $j$  over all sites in the *central* and *surrounding zones* ( $i \neq j$ ). The quantity  $n_i^b$  is unity if a black ion occupies site  $i$  and zero otherwise. Using the notation  $\sigma_{bb}(j) = \sum_i J_{ij} n_j^b$  Eq. (2.8) can be rewritten as:

$$E_{bb} = (1 - x)^2 \sum_i n_i^b \sigma_{bb}(i) = (1 - x)^2 \sigma_{bb} . \quad (2.9)$$

In the same manner we can write  $E_{ww} = x^2 \sigma_{ww}$  and  $E_{bw} = 2x(1 - x) \sigma_{bw}$ . Then the energy of the system per site can be written as:

$$E = \frac{1}{2(N \times M)} [(1 - x)^2 \sigma_{bb} + 2x(1 - x) \sigma_{bw} + x^2 \sigma_{ww}] , \quad (2.10)$$

where the first term in square brackets comes from the interaction between black-black sites, the second from black-white sites and the third from white-white sites. It is easy to see from Eq. (2.10) that the equilibrium energy of the system is a symmetric function,  $E(x) = E(1 - x)$ , with respect to  $x = 1/2$ . The ground states corresponding to concentrations  $x$  and  $1 - x$  can be obtained from each other by

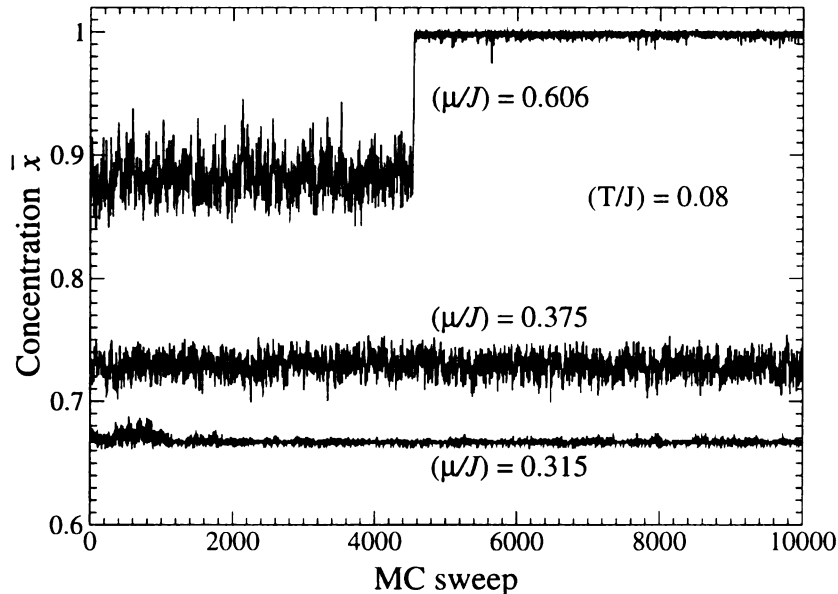


**Figure 2.2:** Dependence of the concentration  $\bar{x}$  on MC sweeps at a fixed values of the chemical potential  $\mu$  at temperature  $(T/J) = 0.08$  for the triangular lattice with  $30 \times 30$  sites in the sample. The values of  $\mu$  are shown near their corresponding curves.

changing all white sites into black sites and all black sites into white sites. In this case  $x \leftrightarrow 1 - x$ ,  $\sigma_{bb} \leftrightarrow \sigma_{ww}$ ,  $\sigma_{bw} \leftrightarrow \sigma_{bw}$  and it follows from Eq. (2.10) that the energy remains the same. In order to accept or reject the move we calculate the change in  $\Delta E - \mu \Delta \bar{x}$ . For calculation of  $\Delta E$  it is necessary to take into account that if we turn a white site  $i$  into a black site then charges at the sites corresponding to the site  $i$  but situated in the surrounding zones should be changed also. When an elementary move is performed, then values of  $\sigma_{bb}$ ,  $\sigma_{bw}$ ,  $\sigma_{ww}$  can be updated by calculating the sums  $\sigma_{bb}(i)$ ,  $\sigma_{bw}(i)$ ,  $\sigma_{ww}(i)$  for the particular site  $i$  that participate in the move. This significantly reduces the calculation time since it is not necessary to recalculate the energy of the whole lattice again after every move.

We say that one MC step was performed if one attempt to perform operation A or B was made. We say that one MC sweep was made if as many MC steps were made as there are sites in the sample. In simulations at a constant  $\mu$  we initially tried

to vary the frequency with which operations  $A$  and  $B$  were performed, but we found that 1 : 1 ratio was close to the optimum value. For every value of the concentration or the chemical potential, simulations start at a relatively high temperature  $T \simeq J$ . If simulations are to be performed at constant  $x$  then in the initial configuration black and white ions in amounts corresponding to  $x$  are randomly distributed over the lattice sites. If simulations are to be performed at a constant value of  $\mu$ , the initial configuration is less important.

We used the following criteria to check the equilibration of the system at a given temperature. Let  $\bar{E}_2$  will be the average value of the energy in the last 10 MC sweeps and  $\bar{E}_1$  will be the average value of the energy in the previous 10 MC sweeps. Let  $\sigma_{E_2}$  and  $\sigma_{E_1}$  be the average fluctuations of energy in those two cycles. If  $|\bar{E}_2 - \bar{E}_1| \leq \frac{1}{10} \min(\sigma_{E_1}, \sigma_{E_2})$  then we say that the system is sufficiently equilibrated in order to collect the data. If this condition is not fulfilled another 10 MC sweeps are made until this condition is met and so on.

After the equilibration, in order to obtain statistics, we calculated and stored the values of parameters of interest after every MC sweep. Their convergence to equilibrium values was verified by plotting them versus the number of the MC sweep. The number of required MC sweeps varied depending on the size of the system, type of interaction and temperature. When the necessary data at a temperature  $T$  were collected, the temperature was decreased by a small amount  $\delta T$ . For smaller values of the temperature  $T$ , a smaller value of  $\delta T$  was used.

It will be shown below that first order phase transitions occur in these systems. In other words ions on the lattice should separate into two parts with different concentrations of the black ions in each part. Parts with different concentrations of the black ions should also have different values of the background charge. But it is assumed in our model that the value of the background charge is the same everywhere. Thus the background in our simulations does not allow the systems to split into parts with

different concentrations and thus does not allow the phase separation to be observed directly.

When we perform simulations at a constant value of average concentration  $\bar{x}$ , it is possible that we may choose some particular average value  $\bar{x}$  that can not occur in a homogeneous system. The energy curve  $E(\bar{x})$  obtained in this case does not really give the dependence of energy on concentration, but rather shows when phase separation should occur. This will be demonstrated explicitly in the next section using the linear chain as an example.

In simulations with a fixed value of the chemical potential the phase transitions are more pronounced. At high temperatures  $(T/J) \geq 1$  changes in the chemical potential lead to the smooth changes in average concentration  $\bar{x}$ . However, at low temperatures  $(T/J) \ll 1$  there are discontinuities in the  $\bar{x}(\mu)$  curve. We assume that the borders of the discontinuity region are the borders of the phase separation region.

The situation at intermediate temperatures is more complicated. As an example, Fig.2.2 shows the concentration as a function of the number of MC sweeps for a  $30 \times 30$  triangular lattice for three values of  $\mu$  at  $(T/J) = 0.08$ . The sharp jump in concentration from  $\bar{x} \simeq 0.88$  to  $\bar{x} = 1$  that occurs at  $\mu/J = 0.606$  shows that both concentrations  $\bar{x} \simeq 0.88$  and  $\bar{x} = 1$  lead to the same minimum value of Helmholtz free energy and thus are stable. Homogeneous equilibrium configurations in the range of concentrations  $0.88 < \bar{x} < 1$  have higher values of the Helmholtz free energy and thus are unstable with respect to phase separation into two parts with concentrations  $\bar{x} = 0.88$  and  $\bar{x} = 1$ .

Fig.2.3 shows the histogram of the distribution of concentrations corresponding to those in Fig.2.2. Peak positions give us the values of average concentrations. For some particular values of  $\mu$  the system migrates between two significantly different concentrations, as for example for  $\mu = 0.606$ . We assume in this case that there is phase separation and relative areas under two peaks give us the relative sizes of

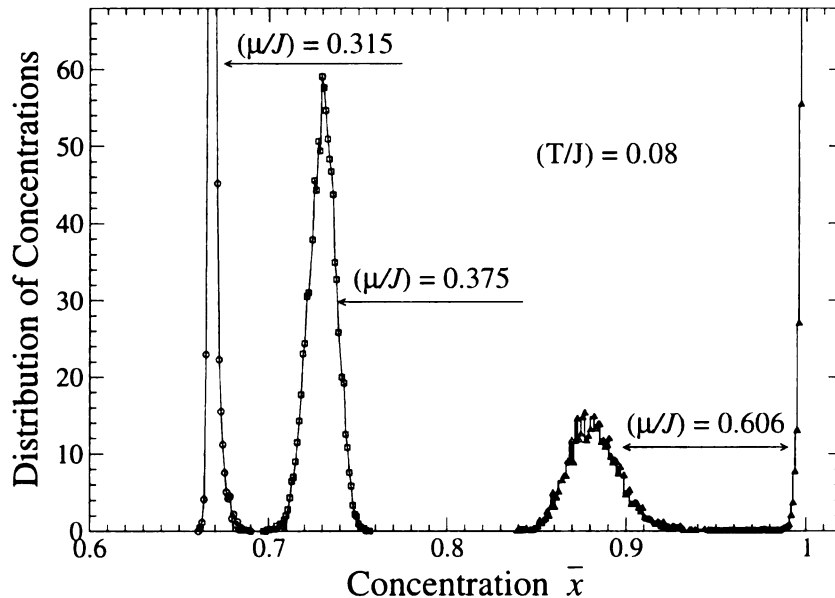


Figure 2.3: Histograms that show distributions of concentrations for the curves from Fig.2.2. Data were collected over 10000 MC sweeps. The sharp peak corresponding to  $(\mu/J) = 0.315$  has height 4000. The peak corresponding to  $(\mu/J) = 0.606$  has a height 1700.

the two phases. Thus the appearance or disappearance of a peak tells us about the appearance or disappearance of a phase. We will use the positions of the peaks when they appear or disappear as the borders of the two phase coexistence region.

At low temperatures  $(T/J) \ll 1$  our MC procedure becomes less effective and the system can become frozen in some configurations. One of the reasons for this is the local character of the moves  $A$  and  $B$  that we use to search for a new configurations e.g. every MC move involves only one or two sites. To study the properties of the system at very low temperatures and critical behavior of the model (when simulations of the large systems are required) it might be useful to implement other simulation methods[27], but that is not the objective of the present work.

## 2.4 Linear Chain

There are two exact analytical methods to study the model in the one dimensional case of the linear chain. In particular, if the Coulomb interaction is truncated at some distance then a *transfer matrix*[25] technique can be applied to calculate the free energy as a function of chemical potential and temperature. Then the dependence  $x(\mu, T)$  can be studied and the phase diagram can be obtained.

In case of the infinite range Coulomb interaction at  $T = 0$ , a *devil's staircase*[17] formalism can be used to predict the equilibrium structure for any concentration and calculate the ground state energy of the system. In both cases exact results will be compared with the results of simulations to establish the precision of the numerical methods.

### 2.4.1 Nearest Neighbors Interaction

If we restrict the range of interaction to nearest neighbors only, the Hamiltonian becomes

$$H = J \sum_i (n_i + q)(n_{i+1} + q) - \mu \sum_i n_i. \quad (2.11)$$

Initially we assume that  $q$  is a constant and is not connected with concentration. Then the grand partition function  $\mathcal{Z}_N$  for a cyclic chain of  $N$  sites can be expressed in terms of the largest eigenvalue of the  $2 \times 2$  transfer matrix as  $\mathcal{Z}_N = \lambda_{max}^N$  with

$$\lambda_{max} = \frac{e^{-\beta J q^2}}{2} \left[ 1 + \gamma + \sqrt{(\gamma - 1)^2 + 4\gamma e^{\beta J}} \right], \quad (2.12)$$

where  $\gamma = e^{\beta(\mu + 2Jq - J)}$  and  $\beta = 1/(k_B T)$ . The grand potential per site is given by  $\Omega = -k_B T \ln[\lambda_{max}]$ . Using the fact that  $\bar{x} = \langle n_i \rangle = \partial \Omega / \partial \mu$ , we can find  $\bar{x}$  as a function of the independent variables  $T$  and  $\mu$ . The resulting expression can then be inverted using the charge neutrality requirement,  $q = -\bar{x}$ , to obtain  $\mu$  in terms of  $\bar{x}$

and  $T$  with the following result:

$$\mu = J - 2J\bar{x} + \frac{2}{\beta} \sinh^{-1} \left[ \frac{(\bar{x} - 1/2)e^{\beta J/2}}{\sqrt{\bar{x}(1 - \bar{x})}} \right]. \quad (2.13)$$

Fig.2.4 shows the transfer matrix predictions for the  $\mu$  versus  $\bar{x}$  curves for various values of  $T/J$  and also the results of numerical simulations. The upper left frame shows the results of the transfer matrix calculations at various temperatures.

Note that  $\mu = 0$  corresponds to  $\bar{x} = 1/2$ . At high temperatures,  $\mu$  is a monotonically increasing function of  $\bar{x}$  but at low temperatures,  $\mu$  has regions where the slope is negative. This behavior is thermodynamically unstable and indicates that phase separation occurs. The upper right frame shows transfer matrix predictions and the results of simulations at  $(T/J) = 0.50$ . Simulation points lie on top of the exact curve. The lower left frame shows the results at temperature  $(T/J) = 0.20$  which is just above the maximum temperature for which phase separation occurs. The regions with a low density of simulation points indicate the appearance of the regions of phase separation that occur at lower temperatures. The concentration  $\bar{x}$  in this region is the average over the two peaks that occurs at the intermediate temperatures as shown in Fig.2.2 and in Fig.2.3. The lower right frame at  $(T/J) = 0.10$  clearly shows the sharp jumps in concentration that occur at low temperatures.

In the simulations, phase separation manifests itself as a discontinuity in the dependence  $\bar{x}(\mu)$ . In contrast, a second order transition would correspond to  $\mu$  increasing monotonically with a discontinuity in slope.

The first order transition can also be seen in plots of the grand potential per site,  $\Omega$ , versus chemical potential. Loops corresponding to the unstable branches appear at low temperatures. However, we find it more convenient to plot the Helmholtz free energy per site,  $F = \Omega + \bar{x}\mu$ , or the internal energy per site,  $E$ , as a function of the concentration  $\bar{x}$ .



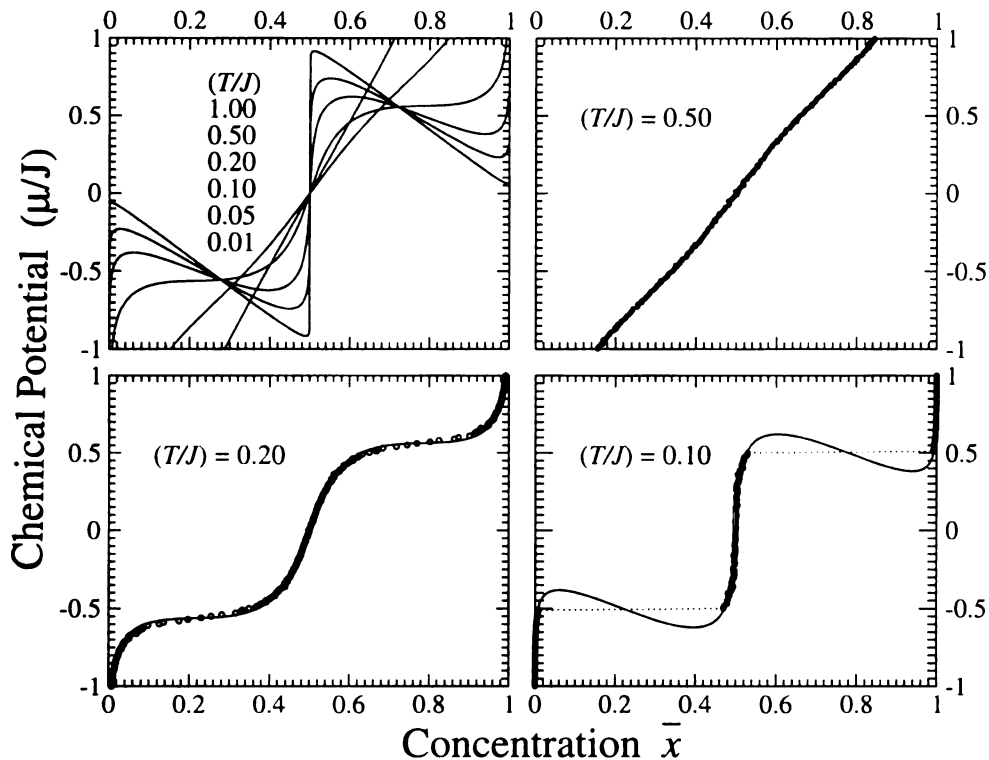


Figure 2.4: Dependence of the chemical potential  $\mu$  on the average concentration  $\bar{x}$  for the case of a linear chain with interaction limited to nearest neighbors only. The plateaus seen in simulations for  $(T/J) = 0.10$  correspond to the regions of phase separation.

A finite temperature phase transition is not expected in one dimension for finite range interactions. However, the presence of the background charge effectively makes this an infinite range problem and produces a first order phase transition at a finite temperature. This behavior is similar to that in the Van der Waals theory of liquids where long range attractive interactions lead to condensation phenomena.

Figure 2.5 shows both energy  $E$  and Helmholtz free energy  $F = E - TS$  as a function of  $\bar{x}$  at  $(T/J) = 0.05$ . The difference between these two curves is due to the entropy of the system. Since the difference between these two curves is significant, the entropy plays an important role even at quite low temperatures.

Since  $\bar{x}$  is the independent coordinate, we apply the double tangent rule to the

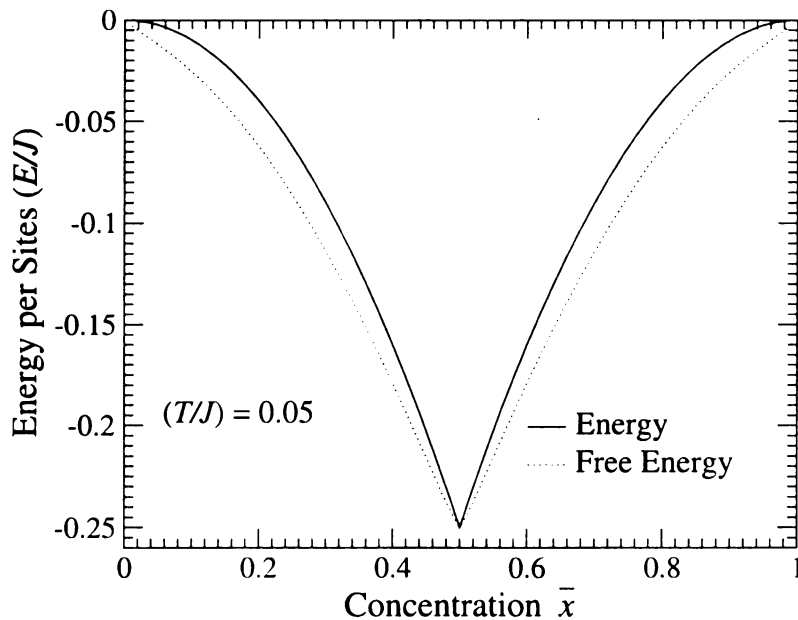


Figure 2.5: Energy and Helmholtz free energy as functions of the average concentration  $\bar{x}$  at temperature  $(T/J) = 0.05$  for a linear chain with interaction limited to nearest neighbors only.

Helmholtz free energy  $F$  (or to the energy curve at  $T = 0$ ) to determine the equilibrium concentration. The slope of the tangent line gives the value of the chemical potential  $\mu$ . This predicts that at  $T = 0$  the system will separate into two phases with concentrations 0 and  $1/2$  if  $\bar{x}$  is between those two concentrations. If  $1/2 < \bar{x} < 1$  then the system will separate into two phases with concentrations  $1/2$  and  $1$ . Hence a plot of  $\mu$  versus  $\bar{x}$  should display flat horizontal sections at values of  $\mu$  corresponding to the slopes of the double tangent lines. This process is equivalent to a Maxwell construction applied to the regions in Fig.2.4 where the  $\mu(x)$  dependence has a negative slope.

If in MC simulations we are trying to produce the  $E(\bar{x})$  curve and we fix the concentration at a particular value that cannot exist homogeneously across the system, then we create an internal stress in the system: the ions tend to separate into two phases but the background charge, through Coulomb interaction, does not allow this

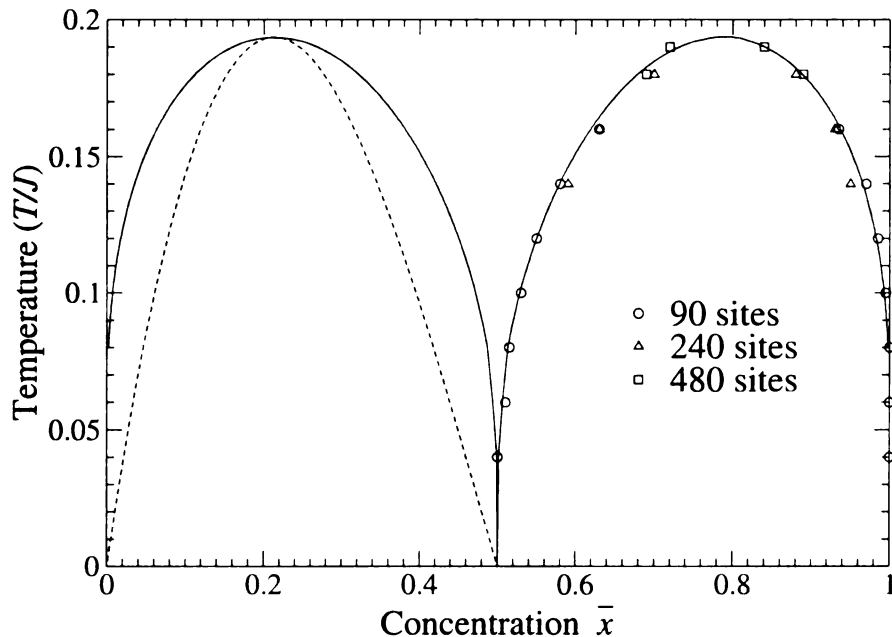


Figure 2.6: Phase diagram for a linear chain with nearest neighbor interactions. The solid lines indicate the borders of the phase separation regions. The dashed curve shown for  $x < 1/2$  only is the spinodal curve. Both curves were obtained with the transfer matrix method. The points on the right show the results of the simulations performed on lattices with different sample sizes.

phase separation since it is constrained to be uniform. This stress should effectively increase the value of the energy  $E(\bar{x})$  in the simulations. It is possible sometimes to see in structures obtained from simulations the tendency to phase separation. In Fig. 2.7 one can clearly see this tendency for the phase separation: The average concentration in the top row is  $1/2$  while the average concentration in the bottom row is  $1/3$ .

Fig. 2.6 shows the phase diagram in the temperature-concentration plane. The solid curve is the transition temperature  $T_c$ . This curve was obtained using the equal area rule applied to the  $\mu$  versus  $\bar{x}$  curves (see Fig. 2.4) obtained from Eq. (2.13). The dashed curve is the spinodal which corresponds to the locus of points for which  $(\partial\mu/\partial\bar{x}) = 0$ . The spinodal is only shown in the region  $x < 1/2$  but it is symmetric

with respect to  $x = 1/2$ . The regions between solid and dashed curves correspond to the regions of metastability.

In order to obtain the phase diagram in MC simulations at low temperatures  $(T/J) \leq 0.12$  we refer back to Fig.2.4. The plateaus in the  $\mu(x)$  dependence give us the concentrations for which phase separation occurs. In other words, any concentration on any plateau should split into the two concentrations on the edges of the same plateau. Thus the edges of the plateaus give us the borders of the two phase coexistence regions and the phase diagram of the system. This approach gives good agreement with exact results at low temperatures but fails at intermediate temperatures when fluctuations in the concentration are big or when system migrates between two different concentrations. To obtain the phase diagram at intermediate temperatures  $0.14 \leq (T/J) \leq 0.20$  we used the observations and interpretation that was discussed above in Fig.2.2 and Fig.2.3. In Fig.2.6 data for the sample with 90 sites were obtained from the borders of the jumps in  $x(\mu)$  curves shown in Fig.2.4. The remaining points are obtained from the distribution of concentrations at different  $T$  and  $\mu$  using larger sample sizes. The peaks in the distributions of concentrations for the sample with 480 sites are narrower than those with 240 sites, as expected. The full width at half of the maximum for the peaks at temperatures  $(T/J) \simeq 0.14$  is about 0.05 and at temperature  $(T/J) \simeq 0.18$  it is about 0.1. Thus at temperature  $(T/J) \simeq 0.18$  peaks corresponding to two different concentrations overlap.

The good agreement between the exact phase diagram and the one obtained from simulations indicates that our interpretation of the histogram of the concentration frequencies is correct. It also indicates the precision of our technique.

## 2.4.2 Finite Range of Interaction

The Hamiltonian of the model at fixed concentration  $x$  is given by Eq. (2.3). In the case of nearest neighbor interaction  $J_1$  and a second neighbor interaction  $J_2$

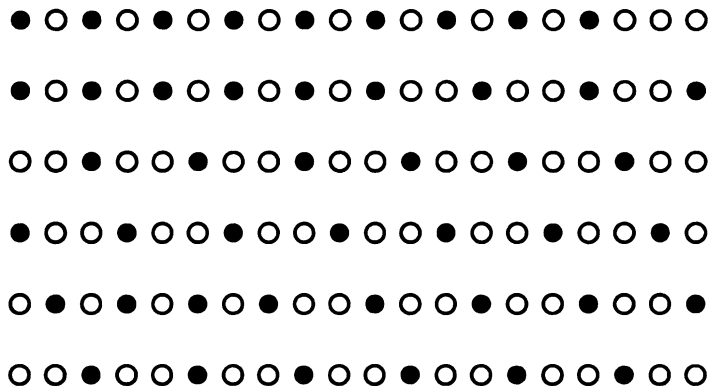


Figure 2.7: The linear chain sample of 120 sites with interactions up to fifth neighbors included at  $\bar{x} = 3/8 = 0.375$  and temperature  $(T/J) = 0.01$ . The second row from the top is the continuation of the first row and so on. The picture illustrates the tendency of the system to phase separation: in the top row  $x \approx 1/2$ , while in the bottom row  $x \approx 1/3$ . Separation cannot really occur due to the same background charge at every site of the chain that corresponds to  $\bar{x} = 3/8$ .

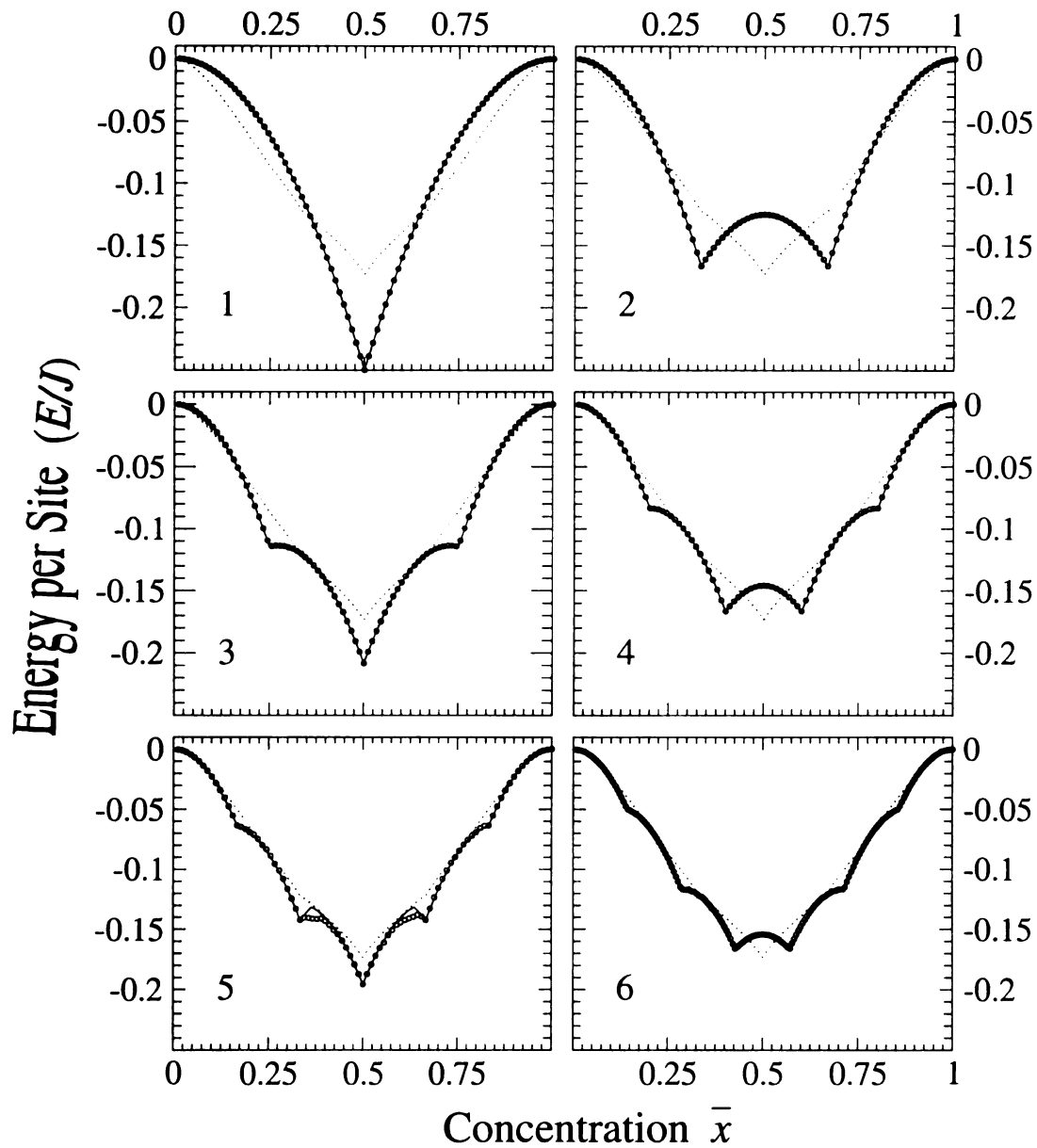
only, the ground state energy can be obtained directly using the following reasoning: for concentrations in the range  $0 < x < 1/3$ , the background charges (white charges) contribute an amount  $-(J_1 + J_2)x^2$  to the energy per site from the last term in Eq. (2.4). The black charges can be placed on every third site so as to avoid the repulsion in the first term. However, in the concentration range  $1/3 < x < 1/2$  the repulsive interactions contribute an additional amount  $(J_1 + J_2)(x - 1/3)$  to the energy. The energy in the range  $1/2 < x < 1$  is obtained using the symmetry property  $E(x) = E(1 - x)$ . Similar reasoning can be used for larger ranges of the interactions but the expressions become more complicated.

Fig.2.8 shows the ground state energies as a function of concentration  $\bar{x}$  at  $T = 0$ , for finite ranged interactions  $J_n = J/n$ , where  $n = 1, 2, 3, 4, 5$  and 6. The solid curves were obtained using the arguments described above and were verified using the numerical transfer matrix method results at very low temperatures. The MC simulations were performed on lattice samples with 90 and 180 sites and periodic boundary conditions.

-0.1  
-0.15  
-0.2  
0  
-0.05  
-0.1  
-0.15  
-0.2  
0  
-0.05  
-0.1  
-0.15  
-0.2

Energy per Site (eV)

Fig. 2  
Fig. 3  
Fig. 4  
Fig. 5  
Fig. 6



**Figure 2.8:** Dependence of the energy per site on concentration, at very low temperatures, for the linear chain with interaction extending up to first, second, third, fourth, fifth and sixth neighbors. Points from simulations are plotted on top of the exact solid curves obtained with transfer matrix technique. Dotted curve shows limiting case of infinite range coulomb interaction.

The panel 2 in Fig.2.8 shows the energy curve for the interaction between nearest and second nearest neighbors only. It is easy to see that for  $\bar{x} = 1/2$  it is energetically favorable for the system to split into two parts with different average concentrations  $\bar{x}_1 = 1/3$  and  $\bar{x}_2 = 2/3$ .

If we apply the double tangent construction to the  $E(\bar{x})$  curves in Fig.2.8, corresponding to the interactions with larger range, we find additional transitions compared to the nearest neighbor case. For interaction up to second neighbors we have first order transitions from  $x = 0$  to  $x = 1/3$ ,  $x = 1/3$  to  $x = 2/3$  and  $x = 2/3$  to  $x = 1$ . For neighbors up to the third included, there are four transitions involving  $x = 0, 1/4, 1/2, 3/4$  and  $1$ .

As the range of interaction increases there is an increasing amount of structure in the energy curves but the double tangent construction does not always lead to an increasing number of transitions. It will be shown in the next section that in the limit of Coulomb interactions, the energy curve approaches a form which predicts only four transitions involving the values  $x = 0, 1/3, 1/2, 2/3, 1$ .

Phase separations predicted from the energy curves cannot occur in our MC simulations because this phase separation requires two different values of the background charge, while in our simulations background charge is constrained to have the same value at every site.

However if concentrations of the two parts are close to each other then the tendency to the phase separation can be seen even if the value of the background charge is the same everywhere as shown in Fig.2.7. This behavior can also be seen on the fifth panel of Fig.2.8 that shows a disagreement between exact curve and results of simulations for the case of interaction up to fifth neighbors. There is a region between  $0.325 \leq \bar{x} \leq 0.425$  in which simulation points seem to follow a horizontal line while the exact curve has a peak in this region. We believe that the origin for this behavior is the tendency for the phase separation described above. Thus every simulated



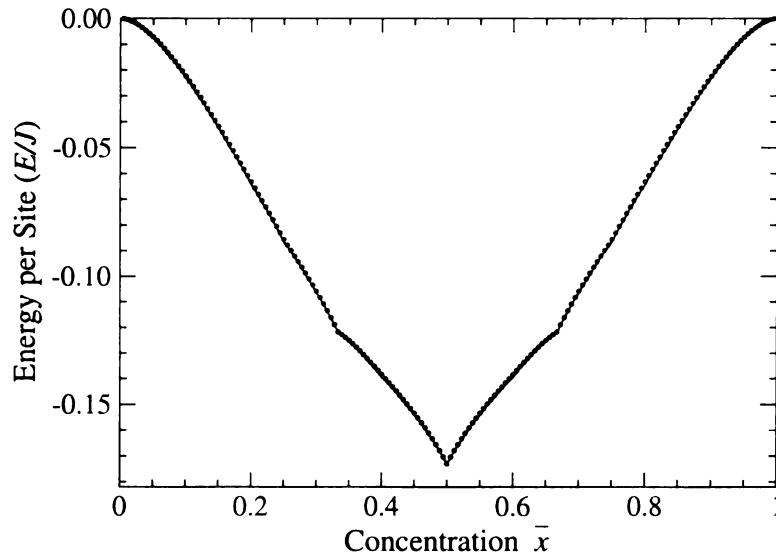


**Figure 2.9:** Energy per site as a function of concentration  $\bar{x}$  for a linear chain with Coulomb interactions. The solid curve was obtained by knowing equilibrium structures predicted with the devil's staircase formalism on the lattice sample with 1000 sites. Circles give the results of the MC simulations at low temperature for samples with 180 sites.

point in this region is a weighted average of two concentrations that correspond to the edges of this horizontal region. The weight is proportional to the fraction of the whole sample that is at a given edge concentration.

In order to apply the transfer matrix method to the case with range of interaction  $n \geq 2$  neighbors, we can group the sites into consecutive blocks of length  $n$  and the interactions are then only between nearest blocks. The transfer matrix formalism can be used again, but the Hamiltonian given by Eq. (2.6) leads to the transfer matrix of size  $2^n \times 2^n$  and it is difficult or impossible to solve the problem analytically. However, it is possible to calculate the largest eigenvalue of the transfer matrix numerically and obtain the thermodynamic properties. We have used this method to study the energy, Helmholtz free energy and chemical potential as a function of concentration  $\bar{x}$ . Our results are in agreement with the predictions made from the energy curves, shown in Fig. 2.8.

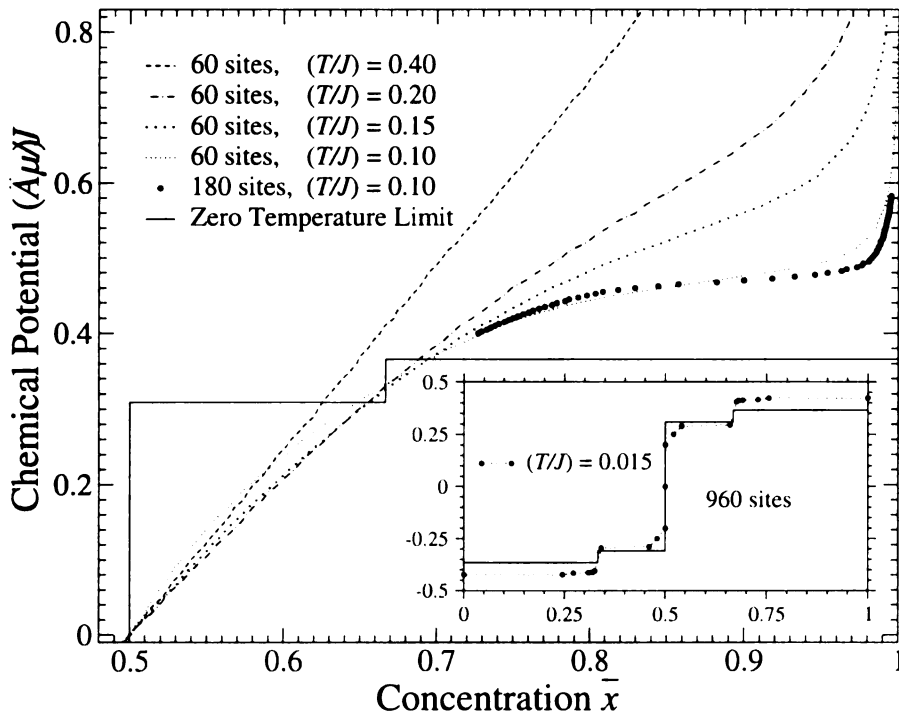


Figure 2.10: Dependence of the chemical potential  $\mu$  on concentration  $\bar{x}$  for the linear chain with Coulomb interaction in the region  $\bar{x} > 1/2$ . The solid line shows the limit of zero temperature obtained from the energy curve on Fig.2.9. The inset shows the results from the lattice sample with 960 sites at very low temperatures in the whole range  $0 < \bar{x} < 1$ .

### 2.4.3 Infinite Range Coulomb Interaction

If the  $J_{ij}$  correspond to the bare Coulomb interaction, the interactions satisfy the positivity and convexity condition [17] which allows the ground state to be found for **any** rational value of  $\bar{x}$ . If  $\bar{x} = 1/n$  where  $n$  is an integer, then the black charges are **equally** spaced along the chain at a distance of  $n$  neighbors apart and form the one dimensional analogue of the Wigner lattice[28]. In the more general case where  $\bar{x} = p/q$  is the ratio of two integers, the ground state configuration is periodic with period  $q$  and has  $p$  black charges in each cell. If there is a black charge at site 0 then black **charges** are at the sites with numbers  $[nq/p] = [n/x]$  where  $n$  is any integer and  $[A]$  denotes the integer part of  $A$ . Since the structure is known for any rational value

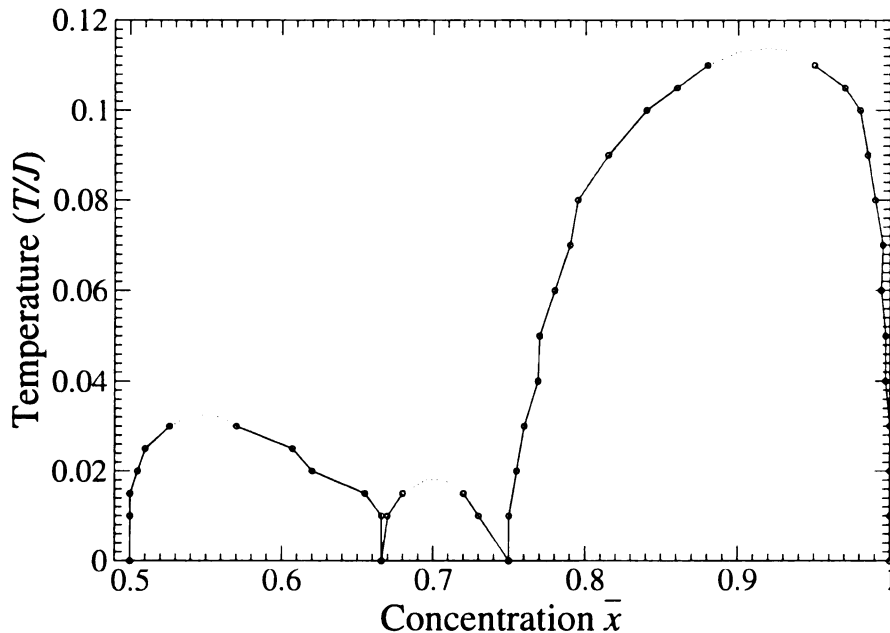


Figure 2.11: Phase diagram for the linear chain with Coulomb interactions in the region  $x > 1/2$  obtained from MC simulations.

of  $x$  the ground state energy can be calculated using the same techniques that was used to calculate energies in MC simulations. But since in this case it is not necessary to run a relaxation procedure much bigger samples can be considered.

Fig.2.9 shows the ground state energy as a function of  $x$  for the Coulomb potential obtained using both the exact ground state configurations and our simulation technique. The value of the energy at  $x = 1/2$  corresponds to alternating black and white charges and is equal to  $-(\ln 2)/4$ . For smaller values of  $x = 1/n$  corresponding to period  $n$  Wigner lattices of equally spaced black charges, the energy per site is given by  $E = x^2 \ln x$ . For values of  $x$  between these values the energy is slightly larger than if we use the same formula for all  $x$ . The energy curve has a sequence of cusps located at all rational values of  $x$  (devil's staircase).

Since at  $T = 0$ , the chemical potential is given by  $\mu = \partial E / \partial x$ , we predict that at zero temperature  $\mu$  versus  $\bar{x}$  will display a series of jumps as shown in Fig.2.10.

The double tangent rule applied to the energy curve predicts phase separations for some values of  $\bar{x}$ . For  $0 < x < 1/3$ , the system should separate into phases with  $x = 0$  and  $x = 1/3$  whereas, for  $1/3 < x < 1/2$ , it should separate into phases with  $x = 1/3$  and  $x = 1/2$ .

Phase separation is due to the second term in Eq. (2.4) which is entirely due to the background. It corresponds to a long range attractive interaction. In the absence of the background, the model would not display phase separation and the chemical potential versus concentration curve would be a devil's staircase with an infinite number of jumps corresponding to the rational values of  $x$ .

The Devil's staircase formalism can be used to obtain the  $E(\bar{x})$  curve at zero temperature and thus predict  $\mu(x)$  dependence at zero temperature. In order to obtain the  $\mu(x)$  dependence at non zero temperature we used MC simulations. The  $\mu(x)$  curves at several temperatures obtained from MC simulations are shown in Fig.2.10. Simulations were performed on samples with 60, 90, 120, 180 and 960 sites. The role of size effects can be seen for the curve  $(T/J) = 0.10$  for which the results from the samples with 60 and 180 sites are shown. For higher temperatures the differences are less significant. We found that up to very low temperatures there are almost no differences between the results on samples with 120 and 180 sites.

The inset in Fig.2.10 shows a rather large difference between the predictions for  $\mu(x)$  from the devil's staircase formalism and from the results of simulations at low temperatures. There can be several reasons for this disagreement. One reason, discussed earlier, is that simulations at low temperatures may not be reliable since the system can become frozen in some local minima that it cannot leave due to the large transition barrier associated with the local character of moves  $A$  and  $B$ . On the other hand the entropy contribution can make the "cusp" at  $x = 1/3$  and  $x = 2/3$  in the  $E(\bar{x})$  dependence more "rounded" and this can lead to an extended range of chemical potential near concentrations  $x = 1/3$  and  $x = 2/3$  on the  $\mu(x)$  curve.

In order to obtain the phase diagram shown in Fig.2.11 we used the technique already discussed above. As expected the size of the plateaus corresponding to the regions of phase separation decreases as the temperature increases and the concentrations of both phases becomes the same at the critical temperature. Only half of the phase diagram is shown since it is symmetric with respect to  $x = 1/2$ . At temperatures  $0.04 \leq (T/J) \leq 0.08$  the data were obtained using a sample with 480 sites. At other temperatures the data were obtained using a sample with 960 sites. There are three distinct regions of phase separation that correspond to the following transitions in concentration at zero temperature:  $1/2 \rightarrow 2/3$  with critical temperature  $(T/J) \simeq 0.03$ ,  $2/3 \rightarrow 3/4$  with critical temperature  $(T/J) \simeq 0.0175$  and  $3/4 \rightarrow 1$  with critical temperature  $(T/J) \simeq 0.11$ .

## 2.5 Triangular Lattice

The Hamiltonian for triangular lattice with Coulomb interaction is given by Eq. (2.6):

$$H = \sum_{\langle ij \rangle} J_{ij}(n_i + q)(n_j + q) - \mu \sum_i n_i. \quad (2.14)$$

The details of model and simulation techniques were described in section 2.2 and 2.3. In the 2D case with long range interaction we used MC simulations as the main method to study the system. Different sample sizes were used in the previous study[1] in order to obtain  $E(\bar{x})$  dependence shown in Fig.2.13.

For the triangular lattice there are multiple “cusps” in the  $E(\bar{x})$  curve that are similar to the devil’s staircase behavior in case of the one dimensional chain. In the region  $1/2 \leq \bar{x} \leq 1$  significant cusps in  $E(\bar{x})$  curve occur at concentrations:  $1/2, 2/3, 3/5, 3/4, 6/7$ .

Ground state configurations for  $x = 1/2, 3/5, 2/3$  and  $3/4$  are shown in Fig.2.12. Ion distributions obtained on the  $30 \times 30$  sample with MC simulations at three different

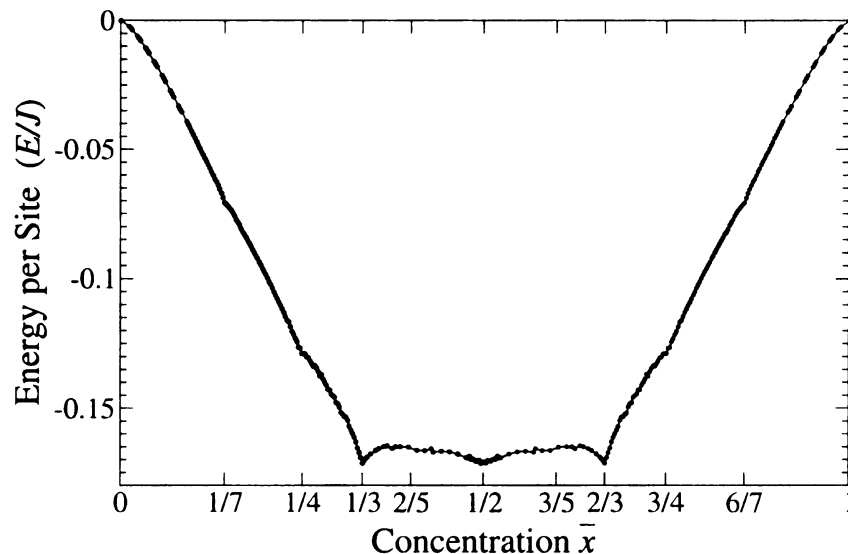


**Figure 2.12:** Energy per site as a function of concentration  $\bar{x}$  for the triangular lattice with Coulomb interactions. The solid curve connects the points obtained by simulations in previous work[1]. Dashed vertical lines give the position of concentrations that are stable in MC simulations at very low temperatures.

values of  $\mu$  at  $(T/J) = 0.01$  are shown in Fig.2.14. In the ground state at  $x = 6/7$  white sites should form a triangular Wigner lattice with the spacing  $a\sqrt{7}$  between ions[1].

For values of  $x = 1/(m^2 + n^2 + mn) \leq 1/3$  or  $1 - x \geq 2/3$  where  $m$  and  $n$  are integers, the ground state configurations are triangular Wigner crystals[28, 29] and the ground state energy can be calculated exactly using the numerical formalism of Bonsall and Maradudin[30]. For these triangular Wigner crystal structures the energy is given exactly by  $E(x) = -2.10671262(x^{3/2} - x^2)$ . Between  $x = 1/2$  and  $x = 2/3$ , the ground state configurations have a rectangular rather than triangular geometry. Regular rectangular structures can be formed at concentrations  $x = l/(2(l+1))$ , where  $l$  is any integer[1]. Thus  $l = 4$  corresponds to  $x = 2/5$  and is the same structure as for  $x = 3/5$  with the interchange of black and white sites. The same numerical method[30] can be used again to obtain  $E(3/5) = -0.1709803$  and  $E(1/2) = -0.1755589512$

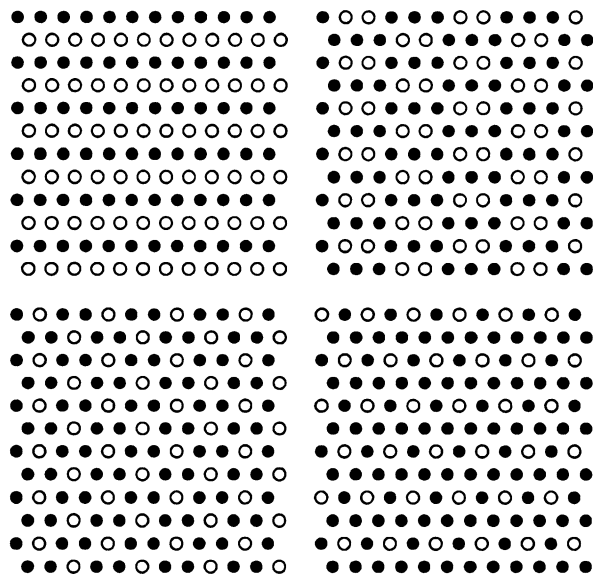


Figure 2.13: Ground state configurations for the triangular lattice with Coulomb interaction for  $x = 1/2, 3/5, 2/3$ , and  $3/4$ .

The first row of the table 2.1 shows the values of the energies obtained from simulations at  $(T/J) = 0.002$  with sample sizes  $\approx 18 \times 18$ . For every concentration the sample size was chosen to be commensurate with particular concentration. The second row shows the results of simulations from the lattice samples of size  $\approx 30 \times 30$ . The third row of the table shows the exact values of the energies obtained with the method of Bonsall and Maradudin.

The major difference between the simulated and the exact values arises because our simulation method can not relax the system to the exact ground state configurations for concentrations  $1/2, 3/5, 3/4, 6/7$ . On the other hand it is easy to obtain the ground state configuration for  $x = 2/3$  and the agreement between the simulated and the exact values of the energy is much better in this case.

Double tangent construction applied to the energy curve Fig.2.13 shows that only concentrations  $0, 1/4, 1/3, 1/2, 2/3, 3/4, 1$  are stable with respect to the phase separation at zero temperature. Thus at zero temperature the system is always a

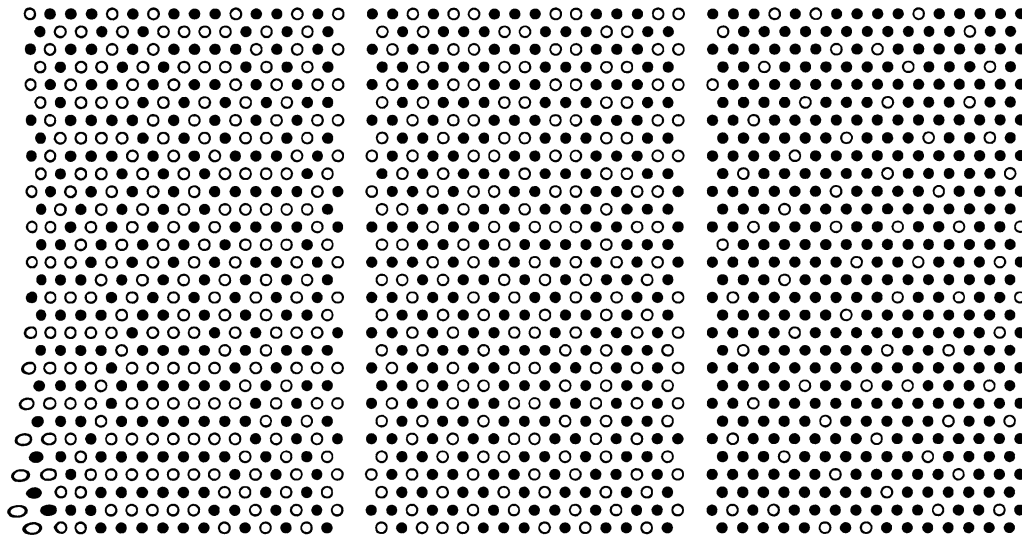


Figure 2.14: Lattice structures obtained from simulations at three different values of  $\mu$  at  $(T/J) = 0.01$ . Concentrations of black ions are close to  $x = 1/2 = 0.5$ ,  $x = 3/5 = 0.6$ ,  $x = 6/7 \simeq 0.857$  for the pictures from left to right.

mixture of parts with these concentrations. For example if  $\bar{x}$  is between 0 and  $1/4$  then the system should split into two homogeneous parts with  $x = 0$  in one part and  $x = 1/4$  in another.

The slope of the double tangent lines gives the values of chemical potential at which the transition from one concentration to another should occur. In the region  $x > 1/2$  we have:  $(\mu/J)_{1/2 \rightarrow 2/3} = 0.0003$ ,  $(\mu/J)_{2/3 \rightarrow 3/4} = 0.5087$ ,  $(\mu/J)_{3/4 \rightarrow 1} = 0.5159$ . The corresponding dependence  $\mu(x)$  at zero temperature shown in Fig.2.15 as the dotted curve. Direct simulations of the  $\mu(x)$  curve were performed on lattices

$\bar{x}$	1/2	3/5	2/3	3/4	6/7
$E_{sim}(18 \times 18)$	-0.17056	-0.16534	-0.16953	-0.12450	-0.06794
$E_{sim}(30 \times 30)$	-0.16964	-0.16456	-0.17070	-0.12671	-0.06807
$E_{exact}$	-0.17556	-0.17098	-0.17136	-0.13167	-0.07076

Table 2.1: Comparison of energies at special concentrations obtained in simulations on lattices with sample sizes  $18 \times 18$ , in the first row,  $\sim 30 \times 30$  in the second row and exact values calculated with method of Bonsall and Maradudin in the third row.



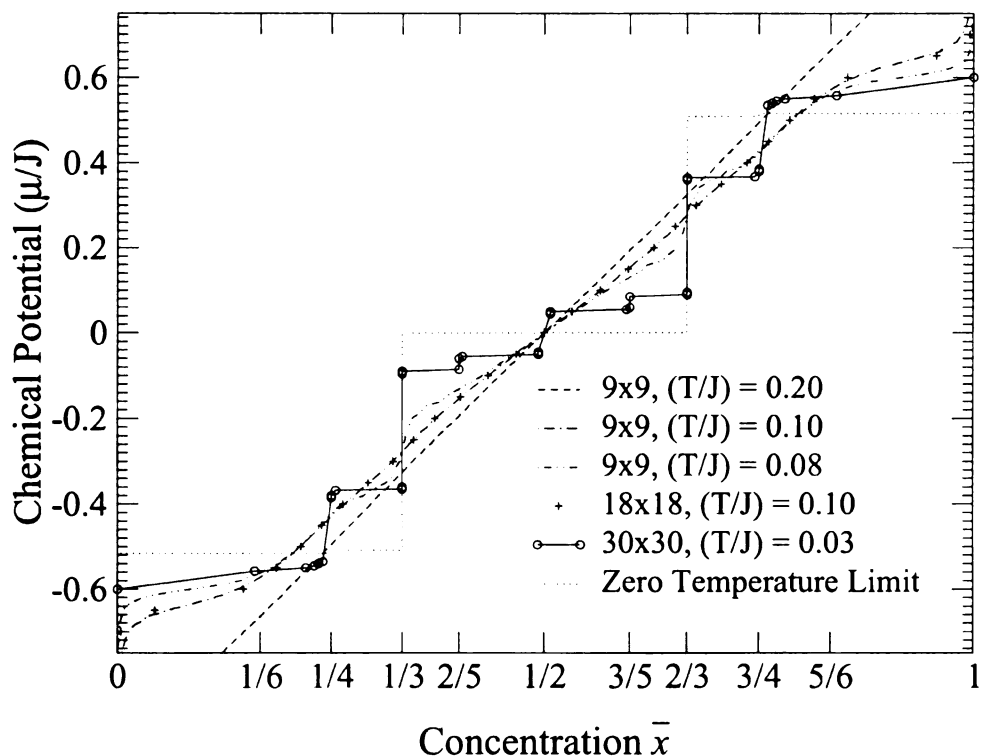


Figure 2.15: Dependence of chemical potential  $\mu$  on concentration  $\bar{x}$  for the triangular lattice with Coulomb interaction. For the cases of temperatures  $(T/J) = 0.2$  and  $(T/J) = 0.1$  the size of the sample was  $9 \times 9$  and no points are shown since their density is high.

of different sample sizes:  $9 \times 9$ ,  $18 \times 18$ ,  $18 \times 20$ ,  $24 \times 24$  and  $30 \times 30$ . Some results are shown in Fig.2.15. Crosses for the sample size  $18 \times 18$  show that there is no big difference with the results obtained on the sample of size  $9 \times 9$  at  $(T/J) = 0.10$ . For higher temperatures the difference is even less significant.

When we consider long range interactions in  $2D$ , the amount of time needed to calculate the energies before and after the MC step increases quickly with the size of the system. In order to save time we tried to perform calculations on smaller samples when possible. Thus at high temperatures, we performed simulations on small  $9 \times 9$  samples. Every point is the result of averaging over 20,000 MC sweeps. Even at  $(T/J) = 0.05$  there is almost no difference between the results of simulations on the

lattices  $18 \times 18$  and  $30 \times 30$ . However, at very low temperatures, there are some structures that can be observed only on large samples. For example at a temperature  $(T/J) \leq 0.03$  we can clearly see concentrations  $3/5$  and  $6/7$  on the  $30 \times 30$  sample, but we cannot see these concentrations on the  $18 \times 18$  sample and they are not pronounced in case of the  $24 \times 24$  sample.

At low temperatures ( $T \simeq 0.01$ ) there is a significant difference between the direct simulations of  $\mu(x)$  dependence and the predictions from the  $E(x)$  curve. In the simulations, the ranges of stability (with respect to the change in chemical potential) at concentrations  $x = 1/4, 3/4$  and  $1/2$  are much larger then they should be according to predictions from the energy curve, while at concentrations  $x = 1/3$  and  $2/3$  the ranges of stability are smaller. In simulations we also see stable concentrations  $2/5$  and  $3/5$  that should not appear according to the energy curve. Several effects can lead to this disagreement.

First of all, the difference between the energy and the free energy curves can be significant even at very low temperatures. This difference can lead to higher stabilities of some concentrations. Moreover some concentrations that should not appear, as follows from energy curve, can appear due to entropic contributions to the free energy. For example, configurations at  $x = 1/3$ , and  $x = 2/3$  are highly ordered and have relatively small entropy. The concentrations between  $x = 1/3$  and  $x = 2/3$  are highly disordered (large entropy) and have approximately the same energy as energy of the system at concentrations  $1/3$  and  $2/3$ . Thus one can expect that concentrations  $1/3$  and  $2/3$  will have smaller range of stability in  $\mu$ , while concentration  $1/2$  will be more stable than follows from energy curve predictions. This is in agreement with Fig.2.15. This feature can also lead to the appearance of some configurations with  $1/3 < x < 1/2$  and  $1/2 < x < 2/3$ : for example  $x = 2/5$  and  $x = 3/5$ . It also explains why we see these concentrations on larger samples and do not see them on smaller samples.

Another reason can be in the way simulations were performed at a constant value of the concentration. For example, if the system has average concentration  $1/2 < \bar{x} < 2/3$  then it should separate into two parts with concentrations  $x = 1/2$  and  $x = 2/3$ . But since at every site the background charge is the same, the system cannot separate. This tendency of the system to phase separation, that cannot occur, creates internal stress and effectively increases the energies of intermediate concentrations. When simulations are performed at a constant value of the chemical potential there is no problem connected with background charge that prohibits the phase separation and there is no stress in the system. Thus energies at intermediate concentrations effectively become smaller.

The last reason that we can mention is the local character of the  $A$  and  $B$  operations that were used to introduce changes in the system. Their local character can also become important at low temperatures.

All the reasons discussed above can lead to the larger regions of stability for concentrations  $x = 1/4, 1/2, 3/4$  and to the smaller regions of stability for the concentrations  $x = 1/3$  and  $x = 2/3$ . They also explain appearance of concentrations  $x = 2/5$  and  $x = 3/5$ .

One can obtain the phase diagram for the triangular lattice in the same way as for the linear chain. In order to obtain the phase diagram of the system at low temperature we had to perform up to 100,000 MC sweeps on the lattice with the sample size equal to  $30 \times 30$ . The phase diagram of the triangular lattice is shown in Fig. 2.16. Only half of the phase diagram is shown since it is symmetric with respect to  $x = 1/2$ . There are five distinct regions of phase separation that correspond to the transitions in concentrations  $1/2 \rightarrow 3/5, 3/5 \rightarrow 2/3, 2/3 \rightarrow 3/4, 3/4 \rightarrow 6/7, 6/7 \rightarrow 1$  at zero temperature. Some regions of phase separation exist only at low temperature and it is difficult to obtain an accurate phase boundary for them.

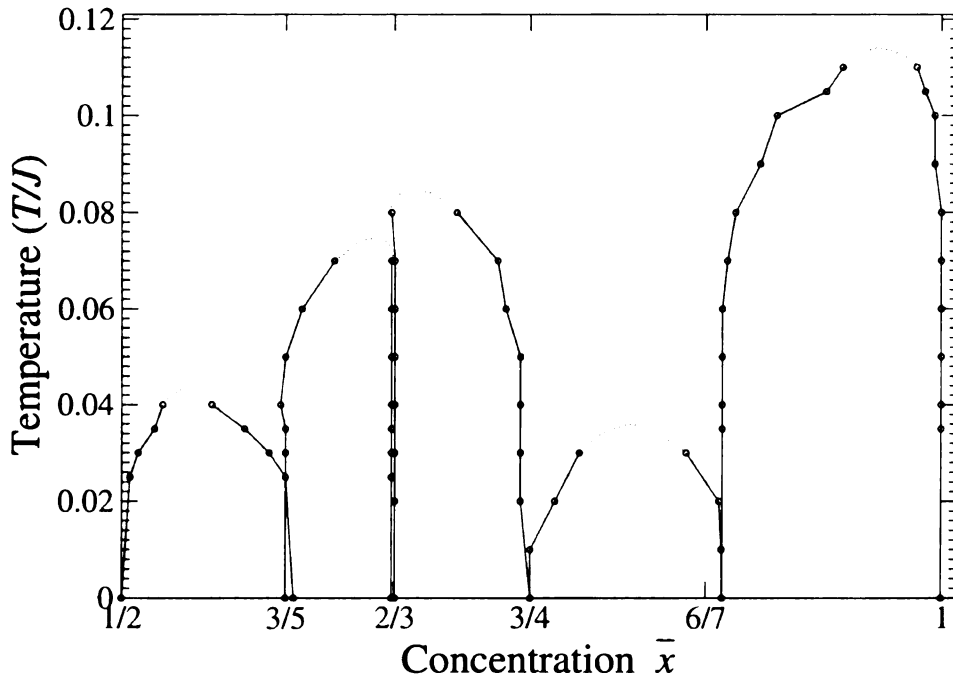


Figure 2.16: Phase diagram for the triangular lattice with Coulomb interaction in the region  $x > 1/2$  obtained with MC simulations.

## 2.6 Conclusion

We have introduced and studied a model to describe the possible ions ordering in layered double hydroxides. In the model ions situated at the sites of the triangular lattice interact through long range Coulomb interaction. The exactly solvable example of the linear chain was used to get insight into the model properties and to demonstrate the precision of the MC simulation methods employed. The model predicts multiple phase transitions and phase separation regions.

Our results are in agreement with experimental measurements in a sense that concentrations  $x = 1/4$  and  $x = 1/3$  are special [3, 4, 5, 6, 7]. However a large number of predicted possible phases with different fractions of metal ions can lead to the situation when effects are hard to see in experiments. If we assume that some phase separation really occurs, then we should allow for the fact that there are different amounts of  $[\text{CO}_3]^{2-}$  anions in the different regions of the same gallery. Regions with

a large number of  $[\text{CO}_3]^{2-}$  anions should have a larger interlayer spacing than the regions with a small number of  $[\text{CO}_3]^{2-}$  anions. This should lead to mechanical stress in the system and that will also resist the tendency to phase separation. This competition between the Coulomb tendency to phase separation and mechanical stress can lead to the disintegration of the compounds and limit the composition range over which layered hydroxides can be synthesized. However the effect of nonzero temperature can move the system over the phase separation boundary and bring the system to a uniform distribution of charges. In this case there should not be internal stress in the compounds. Thus Al substituted layered Ni hydroxides that are stable at higher temperatures may become unstable and disintegrate at lower temperatures.

It would be interesting to see detailed experimental measurements that can support evidence for the charge ordering and the presence or absence of phase separation in these systems.

## Chapter 3

# Absence of Decay in the Amplitude of Pair Distribution Functions at Large Distances

### 3.1 Introduction

Pair Distribution Function (PDF) or radial distribution function  $G(r)$  has been used to study atomic structures of materials since 1927[32, 33]. It is a real function of a single real variable: radius  $r$ . Peaks in PDF centered at values of  $r = \langle r_{ij} \rangle$  that correspond to the average distances between atomic pairs. Thus in principal PDF contains rather limited information about the structure of the materials. Because of it PDF is used mostly to characterize local atomic environment in materials with the absence of long range order like amorphous materials or liquids. Importance of PDF function is caused by the fact that PDF is related in a simple way to the scattering intensity in X-ray or neutron diffraction experiments[34].

If a material consists of atoms of only one type then experimental PDF  $G_{ex}(r)$  can be obtained from reduced scattering intensity  $F(q) \equiv q[S(q) - 1]$  via the sin

Fourier transformation:

$$G_{ex}(r) = \frac{2}{\pi} \int_0^\infty F(q) \sin(qr) dq, \quad (3.1)$$

where  $S(q) \equiv \frac{I(q)}{Nf^2}$ ,  $I(q)$  is scattering intensity averaged over the directions of momentum transfer vector  $q$ ,  $f$  is the ( $q$  dependent) atomic form factor in x-ray scattering, and is the (constant) scattering length in neutron scattering. The total number of scattering centers in the sample  $N$  in practice is defined in such a way that  $S(q)$  goes to unity as  $q$  goes to infinity[34].

As it was already mentioned PDF is related to structure of a material. If material consist of only one type of atoms then:

$$G(r) = 4\pi r[\rho(r) - \rho_0], \quad (3.2)$$

where the average number of atoms in a unit volume (average number density) is  $\rho_0$  and the number of particles in the spherical annulus of thickness  $dr$  is given by  $dN(r) = 4\pi r^2 \rho(r) dr$ . It is clear that radial density  $\rho(r)$  should oscillate around  $\rho_0$ . In order to compare modeled structure with real structure of a material experiment modeled  $\rho(r)$  usually is calculated as follows.

It is a widely used approximation justified by the Debye-Waller theorem, that in solids, if  $\vec{r}_i$  and  $\vec{r}_j$  are equilibrium positions of atoms  $i$  and  $j$ , the density with respect to atom  $i$  created by atom  $j$  is given by[34]:

$$\rho_{ij}(\vec{r}) = \frac{1}{(2\pi\sigma_{ij}^2)^{\frac{3}{2}}} \exp\left[-\frac{(\vec{r} - \vec{r}_{ij})^2}{2\sigma_{ij}^2}\right], \quad (3.3)$$

where  $\vec{r}_{ij} = \vec{r}_j - \vec{r}_i$  and  $\sigma_{ij}^2 = \langle (\vec{r}_{ij} - \langle \vec{r}_{ij} \rangle)^2 \rangle$  is the mean square deviation of  $\vec{r}_{ij}$  from its equilibrium value  $\langle \vec{r}_{ij} \rangle$  due to atomic vibrations. In order to obtain  $\rho(r)$  it is necessary to perform angular averaging of  $\rho_{ij}(\vec{r})$ . This can easily be done in 3d

leading to:

$$\rho_{ij}(r) = \frac{1}{4\pi r r_{ij} \sqrt{2\pi\sigma_{ij}^2}} \left\{ \exp\left[-\frac{(r-r_{ij})^2}{2\sigma_{ij}^2}\right] - \exp\left[-\frac{(r+r_{ij})^2}{2\sigma_{ij}^2}\right] \right\}. \quad (3.4)$$

Since in solids deviations of atoms from their equilibrium positions are much smaller than interatomic distances  $\sigma_{ij} \ll r_{ij}$ , the second term in the numerator can be ignored and  $r_{ij}$  in the denominator can be substituted with  $r$ . The total radial density with respect to the atom  $i$  is obtained as a sum of contributions from different atoms  $j$ :

$$\rho_i(r) \cong \frac{1}{4\pi r^2} \sum_{j \neq i} \frac{1}{\sqrt{2\pi\sigma_{ij}^2}} \exp\left[-\frac{(r-r_{ij})^2}{2\sigma_{ij}^2}\right]. \quad (3.5)$$

Finally in order to obtain  $\rho(r)$  it is necessary to average  $\rho_i(r)$  over all sites  $N$  in the sample:

$$\rho(r) = \frac{1}{N} \sum_{i=1}^N \rho_i(r). \quad (3.6)$$

PDF  $G(r)$  is obtained by substitution of  $\rho(r)$  into (3.2)[34, 58, 36, 37, 38]. From formulas (3.2,3.5,3.6) follows that peaks in  $G(r)$  occur at values of  $r$  that correspond to the average interatomic distances in a material and that since  $\rho(r)$  oscillates around  $\rho_0$  PDF should oscillate around zero.

By comparing PDF calculated for some model structure with experimental PDF obtained from scattering data it is possible to verify how close the model structure is to the real structure of the material. PDFs for amorphous materials and liquids contain only a few peaks, whose amplitudes quickly decrease as  $r$  increases, as it is shown in panel *C* of Fig.3.4. Because of this, little attention was paid to the behavior of PDF at large distances.

In the last 20 years PDF has also been used to extract information about interatomic interactions in crystalline materials[39]. This can be done because  $\sigma_{ij}$  is *interaction-dependent*[37, 38]. Experimental PDF for crystalline materials decays



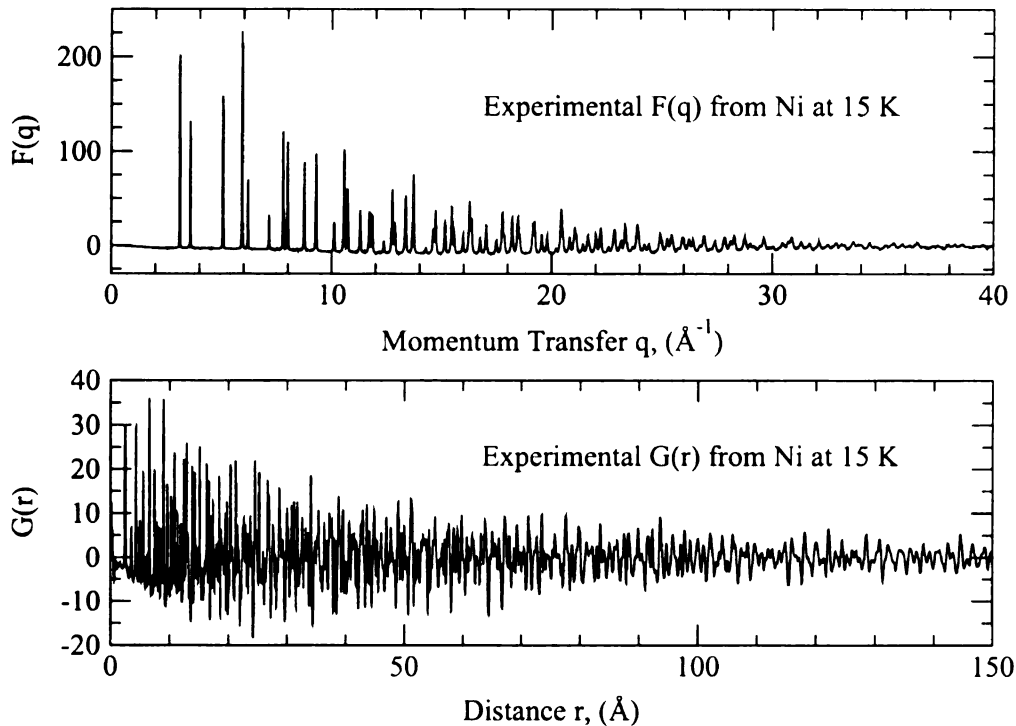


Figure 3.1: Experimental  $F(q)$  and  $G(r)$  of Ni at 15K measured by neutron scattering.

significantly slower than for amorphous materials, as shown in Fig.3.1 that shows reduced scattering intensity  $F(q)$  obtained in the neutron diffraction experiment at the NPDF diffractometer at Los Alamos National Laboratory and corresponding PDF,  $G(r)$ , obtained from  $F(q)$  by Fourier transformation (3.1).

However traditionally there still was interest in behavior of PDF at small distances because that is the region from which structural information can be easily extracted. Thus it seems to us, to the best of our knowledge, that although PDF was used to characterize materials for almost a 100 years, behavior of PDF at large distances was never carefully discussed. For example, it is unclear why PDF decays at large distances. In fact, there can be three different reasons that can lead to the decay of PDF with an increase in distance.

The First and the most natural reason is the following. Note that from (3.5) follows that the value of  $\rho_i(r)$  at  $r$  is determined by those atoms that are in  $\sigma$ -vicinity

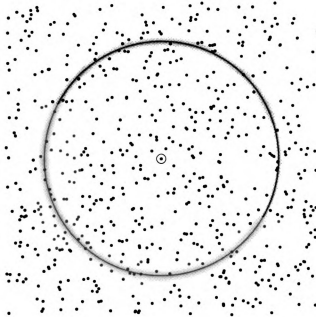


Figure 3.2: Only those sites contribute to the value of  $G_i(r)$  that are in  $\sigma$  vicinity of the distance  $r$  with respect to site  $i$ .

of the spherical shell of the radius  $r$ . In other words, in order for the site  $j$  to contribute to the value of  $\rho_i(r)$  the following condition should hold:  $|r - r_{ij}| \sim \sigma$  (see Fig.3.2). The volume that these atoms occupy can be estimated as  $dV_{\sigma,r} \sim 4\pi r^2 \sigma$ , while the number of atoms in this volume can be estimated as  $dN_{\sigma,r} \sim 4\pi r^2 \rho(r) \sigma$ . As  $r$  increases both  $dN_{\sigma,r}$  and  $dV_{\sigma,r}$  increase and it is natural to expect that  $\rho(r) \sim dN_{\sigma,r}/dV_{\sigma,r}$  converges to  $\rho_o$  leading to the decay of peak amplitude in PDF (see (3.2)). However the question of how  $\rho(r)$  converges to  $\rho_o$  was never properly addressed and we will see that prefactor  $r$  in (3.2) plays a very non-trivial role.

The second reason that can lead to the decay of PDF with increase of  $r$  is averaging (see (3.6)) of  $\rho_i(r)$  over different central atoms  $i$  each of which can have a different atomic environment.

Finally the third reason that can lead to the decay of experimental PDF is finite instrumental resolution that increasingly broadens the width of the peaks with an

crease of the distance. In order to achieve better agreement with an experiment, PDF calculated according to (3.2,3.5,3.6) is usually convoluted with so-called instrumental resolution function that is  $r$  dependent[37]. This convolution increases the width of the peaks at large values of  $r$  more significantly than the width of the peaks at small values of  $r$ .

It is clear that finite instrumental resolution leads to the decay of PDF, but do both the first and second reasons also lead to the decay of PDF? Here we are trying to discuss this issue carefully. This study was initiated by the observation (a puzzle) that PDF calculated for the fcc structure of crystalline Ni, in assumption of infinite instrumental resolution (no convolution was made), does not decay at large distances at all. The average amplitude of peaks in PDF function persists up to the very large distances as shown in Fig.3.3.

All atomic positions in the fcc structure of Ni are equivalent. Because of it there is no need to perform averaging over different atomic sites (3.6). Thus it turns out, surprisingly, that increase in the volume of the spherical annulus with  $r$  does not lead to the decay of PDF (first reason mentioned above). That is something counterintuitive. However it basically means that the amplitude of fluctuations in  $\rho(r) - \rho_o$  calculated with respect to one particular atom in fcc structure decays as  $1/r$  (see (3.2)). The question is why it decays as  $1/r$ . The answer to this question for fcc lattice and other lattices is not completely known. This problem is related to the area of mathematics called “lattice point theory”[40, 41, 42]. The problem that is basically equivalent to the one under consideration was originally formulated by C.F. Gauss[43]. It was studied for more than a hundred years and it is still not completely solved.

In our study we took a somewhat different approach. Since in nature, besides crystalline there are also amorphous materials we decided to study at first structures with disordered distribution of atoms in them. We a found simple exact solution for

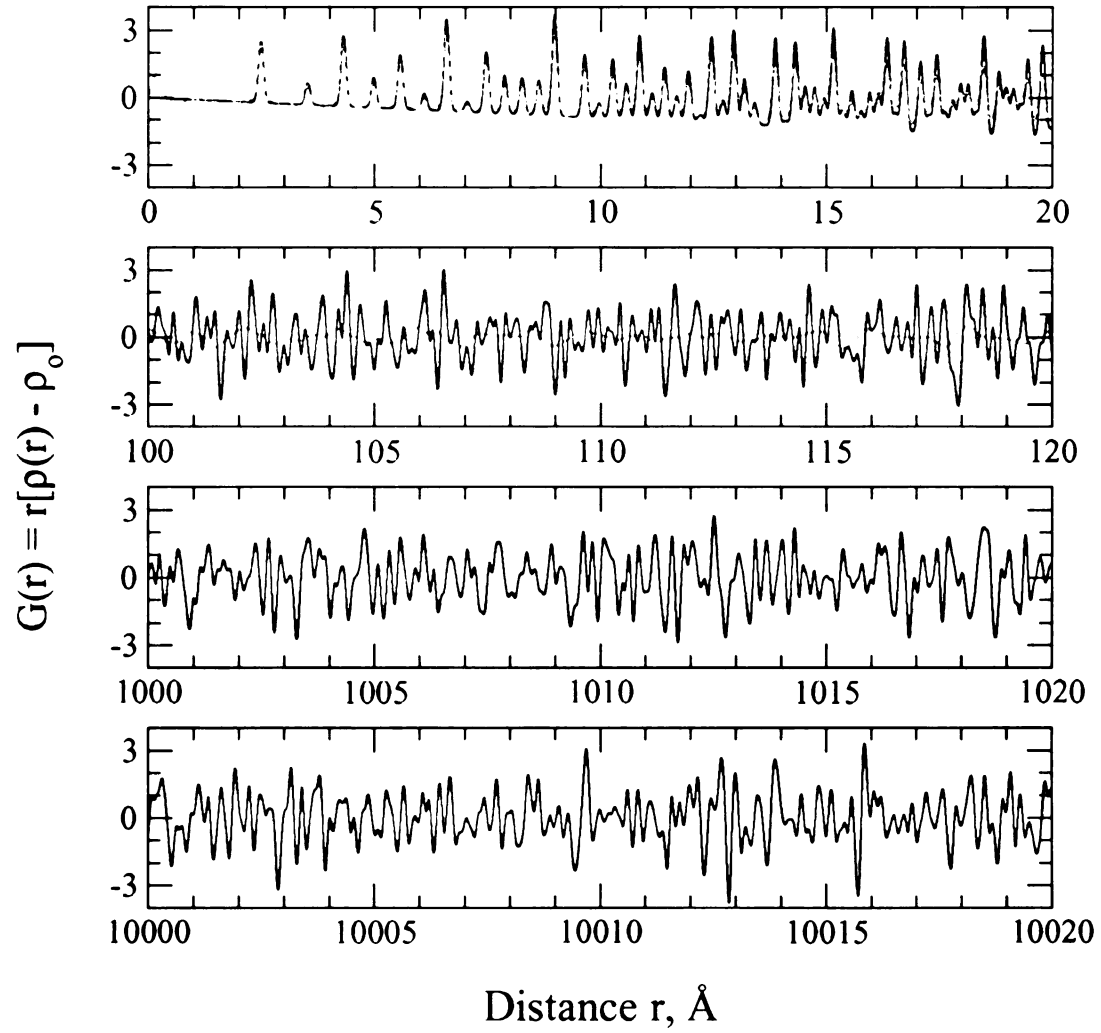


Figure 3.3: PDF of Ni at 15K at different distances. The blue solid lines are results of calculations while the red dotted lines on the two panels on top show the result of neutron scattering experiment taken from Fig. 3.1

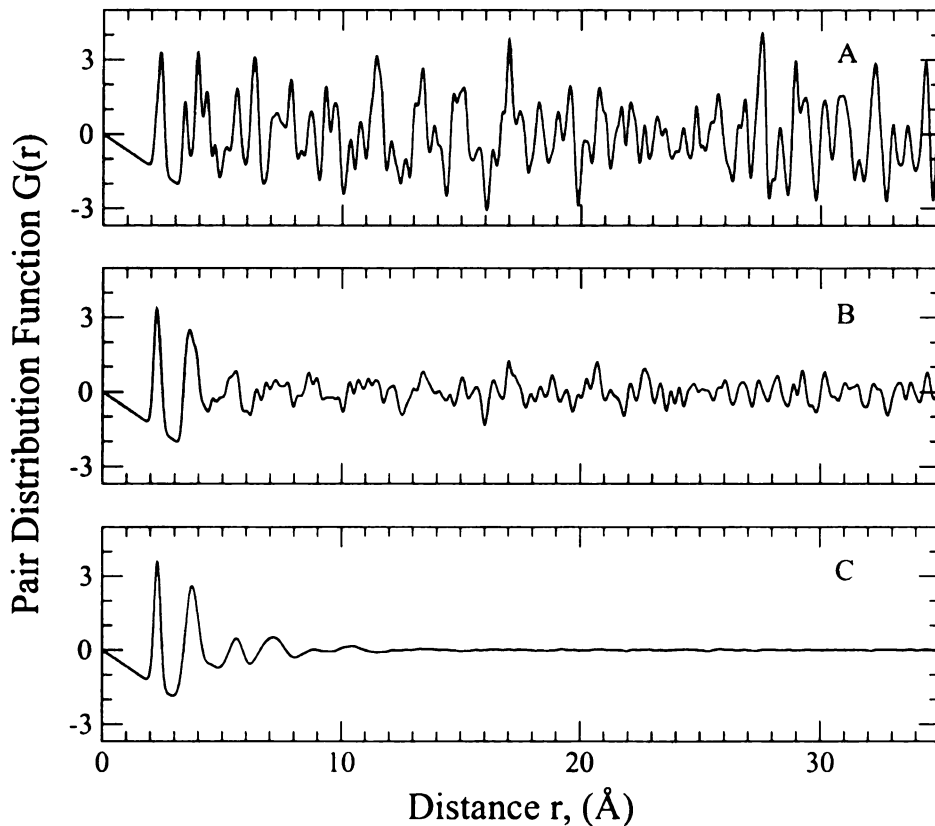


Figure 3.4: PDF for the amorphous Si:  $a_o \simeq 2.4 \text{ \AA}$ ,  $\sigma = 0.1 \text{ \AA}$ . A: with respect to 1 atom, B: averaged over 10 atoms, C: averaged over 20000 atoms.

the case when atoms are distributed completely randomly. Randomly means that position of two atoms can even coincide. The case of amorphous materials is different from the random case, in particular, because there is excluded volume around every atom. We found a way to take into account the role of the excluded volume. These two cases allow consideration in d-dimensional space and we follow this line. The case of crystals is the most complicated and we discuss some aspects of PDF behavior on crystals at the end.

Thus experimental PDF obtained on a crystal decays due to finite instrumental resolution and imperfections of the crystalline structure. In amorphous materials the decay of  $G(r)$  occurs primarily due to the averaging (3.6) of PDFs over many atoms that have different atomic environment as shown in Fig.3.4.

For simplicity we discuss everywhere the case of materials consisting atoms of one type. It is evident how to make a generalization for the case of materials that are formed by different atoms.

Mean square deviations of the distance between a pair of atoms from its equilibrium value  $\sigma_{ij}^2$  depends on positions of the atoms in the sample. For a given structure the values of  $\sigma_{ij}^2$  can be calculated from a particular force model[58, 36], as it was made for the top two panels of Fig.3.3. However if the distance between atoms  $i$  and  $j$  is large then their motion is uncorrelated and it can be assumed that  $\sigma_{ij}^2$  is the same for all atoms that are far away from each other  $\sigma_{ij}^2 = \sigma^2$ , as we do in this paper.

The chapter is organized as follows. At first we define PDF in d-dimensional space. Then we consider the case of completely random atomic distribution. After that we discuss the case of the random distribution of atoms, with randomness limited by excluded volume. Behavior of PDF in crystals is discussed after that. We conclude by discussing how reduced scattering intensity  $F(q)$  would look like on a perfect crystal if there would be infinite instrumental resolution. In the main body of the chapter there are only simple evaluations with results of numerical calculations (on square and triangular lattices for 2d and simple cubic, orthorhombic and fcc lattices in 3d), while more complex derivations are presented in the appendices.

## 3.2 PDF in d-Dimensional Space

### 3.2.1 Continuous Definition of PDF

It is possible to generalize the definition of PDF in 3d to the general case of d-dimensions. As it will be clear from the following PDF in d-dimensional space should be defined as:

$$G_d(r) = r^{\frac{d-1}{2}} [\rho_d(r) - \rho_o]. \quad (3.7)$$

This definition differs by the constant factor ( $4\pi$ ) from the definition of  $G(r)$  in 3d given by (3.2). It is not important for us whether we define PDF with this prefactor or without. For the purpose of generality everywhere below we will use definition of PDF given by (3.7).

The angular averaging of (3.3) leading to (3.4) cannot be performed in 2d or generally in d-dimensional space in a closed form. However we will assume that forms similar to (3.5) with correct prefactors are valid for any dimension:

$$\rho_{di}(r) = \frac{1}{\Omega_d r^{d-1}} \sum_{j \neq i} \frac{1}{\sqrt{2\pi\sigma_{ij}^2}} \exp\left[-\frac{(r - r_{ij})^2}{2\sigma_{ij}^2}\right], \quad (3.8)$$

where  $\Omega_d$  is the total solid angle ( $\Omega_1 = 1$ ,  $\Omega_2 = 2\pi$ ,  $\Omega_3 = 4\pi$ ). In order to obtain  $\rho_d(r)$  from  $\rho_{di}(r)$  averaging over different points (3.6) should be performed.

In the following we will also discuss PDF calculated with respect to a particular site:

$$G_{di}(r) = r^{\frac{d-1}{2}} [\rho_{di}(r) - \rho_o]. \quad (3.9)$$

We will see in the following that the period and amplitude of oscillations in  $G_{di}(r)$  at large values of  $r$  are almost independent of  $r$  for the given type of the structure, as can be seen from Fig.3.3. The period of oscillations in  $G_{di}(r)$  is determined basically by  $\sigma$ . Thus one can expect that average value of the integral:

$$\langle G_{di}^2(r) \rangle = \frac{1}{R_2 - R_1} \int_{R_1}^{R_2} G_{di}^2(r) dr. \quad (3.10)$$

calculated over a big enough interval ( $R_1; R_2$ ) is independent of  $R_1$  if  $R_1$  is big enough.

This approach will be used further for all types of materials.

For the case of amorphous materials, instead of integration of  $G_{di}^2(r)$  over some range one may want to average  $G_{di}^2(r)$  over the different sites  $i$ . For the case when sites are distributed in space completely randomly it is also possible to do averaging

over different distributions. All these methods should, as it will be shown, lead to the same result.

For a particular type of lattice,  $\langle G_{di}^2(r) \rangle$  can depend only on the lattice parameter  $a$  (i.e. density  $\rho_o = 1/\lambda^d$ ) and the value of  $\sigma$ . Thus the dimensionless combination of  $\langle G_{di}^2(r) \rangle$ ,  $\rho_o$  and  $\sigma$  which is:

$$g_{di}^2(\sigma/\lambda) = \langle G_{di}^2(r) \rangle \frac{\sigma}{\rho_o} \quad (3.11)$$

can depend only on dimensionless combination of  $\rho_o$  and  $\sigma$  i.e.  $\sigma^d/\rho_o$  or on  $\sigma/\lambda$ . The same is true for a particular type of amorphous material or for a random distribution.

In the following, instead of  $g_{di}^2(\sigma/\lambda)$  we will use the notations  $g_d^2(L)$  for lattices,  $g_{di}^2(R)$  for random distributions of points,  $g_{di}^2(F)$  for random distributions of points with excluded volume and  $g_{di}^2(G)$  for distributions of points that model glasses. Sometimes, when it is obvious what is meant, we will drop indices  $d$  and  $i$  or both without notice.

### 3.2.2 Definition of PDF Through Bins

Definition of PDF given in the previous section is a continuous definition of PDF. This definition is useful because it allows us to compare model and experimental PDFs. For our purposes, it is convenient to give a different definition of PDF also.

Let assume that we want to calculate PDF with respect to site  $i$ . Then we can define radial density with respect to site  $i$  at distance  $r$  by counting the number of points in the interval (bin)  $[r - \delta/2, r + \delta/2)$ . If there are  $N_i(\delta, r)$  points in the interval then radial density at  $r$  can be defined, assuming  $\delta \ll r$ , as:

$$\rho_{di}(\delta, r) = \frac{N_i(\delta, r)}{\Omega_d r^{d-1} \delta} \quad (3.12)$$

It is clear that  $\rho_{di}(\delta, r) \approx \rho_o$ . Then PDF is defined in the same way as before (3.9)



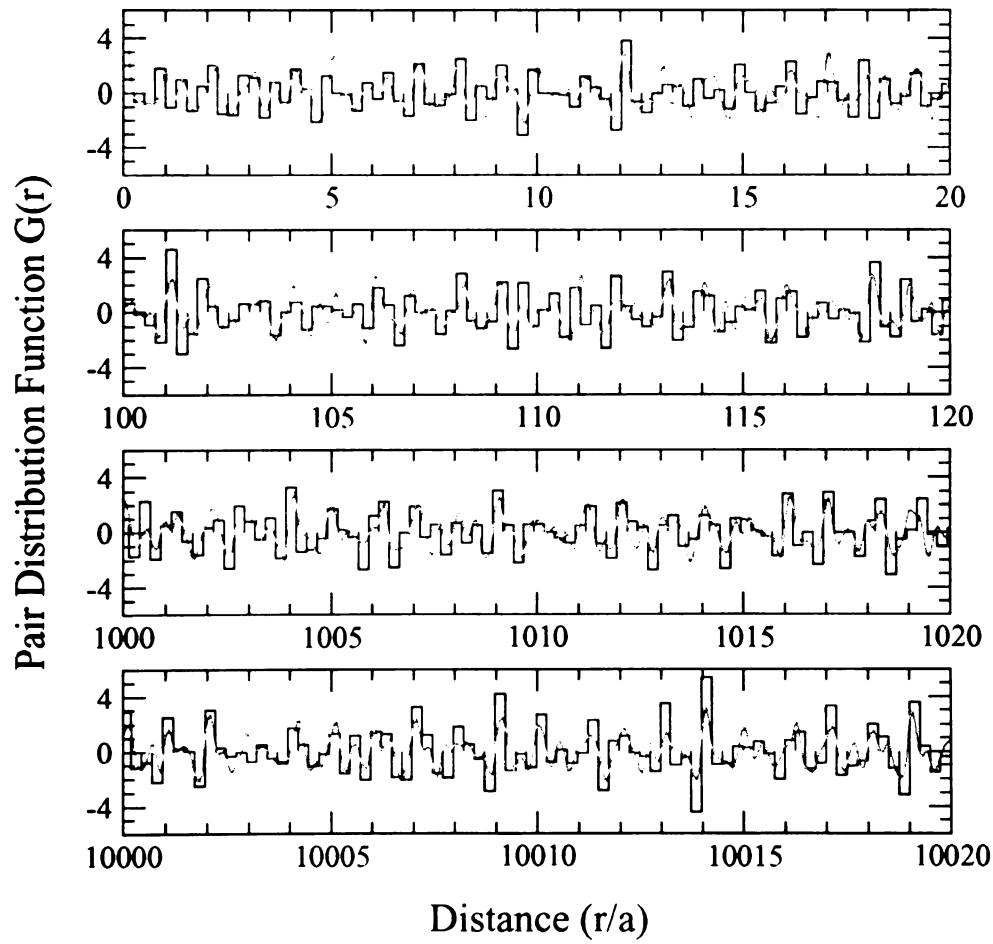


Figure 3.5: PDF calculated for a square lattice  $\sigma = 0.1a$  according to definitions through bins (blue lines) and Gaussians (red lines). Fig.3.1

with  $\rho_{di}(\delta, r)$  instead of  $\rho_{di}(r)$ .

In order to make a comparison between continuous definition of PDF and definition of PDF through bins it is convenient to establish some relationship between  $\sigma$  and  $\delta$ . We find it convenient to define this relationship in assumption that in both approaches the weight of the peak associated with every point is unity:

$$1 = \int_{-\infty}^{\infty} \frac{1}{\sqrt{2\pi\sigma^2}} \exp -\frac{(r - r_{ij})^2}{2\sigma^2} dr = h \cdot \delta ,$$

where the height of the peak in definition through bins— $h$  is forced to be the same as the height of the peak in continuous definition, i.e.  $h = 1/\sqrt{2\pi\sigma^2}$ . Thus  $\delta = \sqrt{2\pi\sigma^2}$ .

It was already shown (Fig.3.3) that amplitudes of peaks in PDF calculated according to (3.8,3.9) for fcc (3d) structure of Ni persisted up to very high distances. Figure 3.5 shows PDFs calculated according to both (continuous and through bins) definitions of PDF for square lattice in 2d. Thus we see that both definitions are equivalent in some sense. We also see that the amplitude and frequency of oscillations are basically the same at all distances.

### 3.3 Random Case

It is rather difficult to understand behavior of PDF in cases when atoms or points form ordered structures lattices. We found that the case when points are distributed randomly, besides being easily understandable, also provides a great insight into the origin of non-decaying behavior of PDF.

The value of  $\langle G_{di}^2(r) \rangle$  (see (3.10)) in the random case can be easily estimated, if it is assumed that averaging is done over different distributions of sites  $i$ . It follows from the definition of PDF through bins (3.8,3.9) that:

$$\langle G_{di}^2(r) \rangle = \frac{\langle [\Omega_d r^{d-1} \delta \rho_{di}(\delta, r) - \Omega_d r^{d-1} \delta \rho_o]^2 \rangle}{\Omega_d^2 r^{d-1} \delta^2}. \quad (3.13)$$

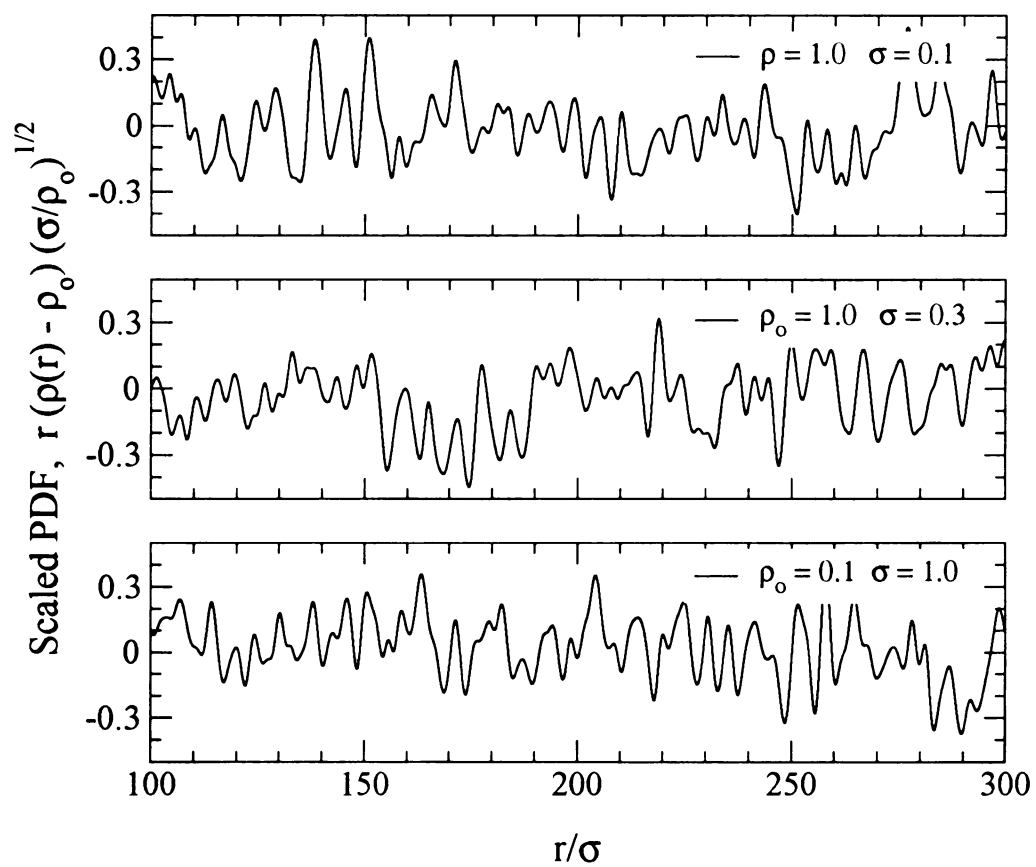


Figure 3.6: Scaled PDF function  $g_{3i}(r) \equiv G_{3i} \sqrt{\sigma/\rho_o}$  vs. reduced distance  $r/\sigma$ .

As follows from the definition of  $\rho_{di}(\delta, r)$  (3.12) the number of particles inside the spherical annulus of radius  $r$  and thickness  $\delta$  is given by  $N_i(\delta, r) = \Omega_d r^{d-1} \delta \rho_{di}(\delta, r)$ , while the average number is given by  $\overline{N_i(\delta, r)} = \Omega_d r^{d-1} \delta \rho_o$ . The well known result of statistical physics can be employed[45]:

$$\langle [N - \overline{N}]^2 \rangle = \overline{N}. \quad (3.14)$$

Thus we get:

$$\langle G_{di}^2(r) \rangle = \frac{\Omega_d r^{d-1} \delta \rho_o}{\Omega_d^2 r^{d-1} \delta^2} = \frac{1}{\Omega_d} \frac{\rho_o}{\delta}. \quad (3.15)$$

Exact calculations for the continuous definition of PDF performed (see text (3.10)) in appendices (A.1.1) in ensemble averaging and in (A.1.2) in the integral approaches lead to the following result:

$$g_{di}^2(R) = \langle G_{di}^2(r) \rangle \frac{\sigma}{\rho_o} = \frac{1}{2\sqrt{\pi}\Omega_d} = const. \quad (3.16)$$

From (3.15,3.16) it follows that in the random case  $\langle G_{di}^2(r) \rangle$  does not depend on  $r$ . This result means that an increase in the number of particles inside the spherical annulus of thickness  $\sigma$  with  $r$  does not lead to the decay of PDF. It also means that in the random case  $\rho_i(r)$  converges to  $\rho_o$  as  $r^{\frac{1-d}{2}}$ , e.i. as  $1/\sqrt{r}$  in 2D and as  $1/r$  in 3D.

Note that for the random case the value of  $g_{di}^2$  does not depend on the value of  $\sigma/\lambda$ .

Fig.3.6 shows dependence of scaled PDF  $g_{3i}(r) \equiv G_{3i}(r)\sqrt{\sigma/\rho_o}$  on scaled distance  $r/\sigma$ . It shows that the amplitude of oscillations in the scaled PDF  $g_{3i}(r)$  does not depend on  $\rho_o$  or  $\sigma$ . It also shows that  $\sigma$  determines the period of oscillations. Note that the period  $T \sim 4\sigma$  is of the order of  $\sigma$ .

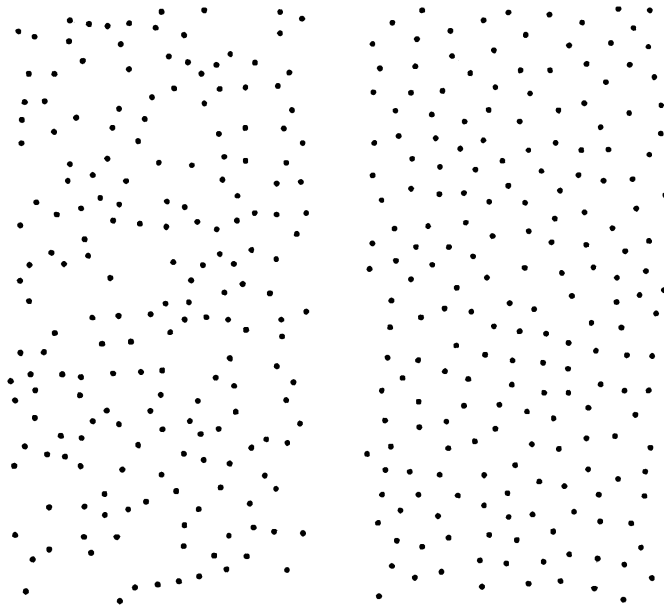


**Figure 3.7:** Distributions of points for two different excluded distances. The left figure shows distribution that was obtained by choosing excluded distance in such a way that excluded area covers  $1/4$  of the total area. In the right figure, excluded area covers  $1/2$  of the total area.

## 3.4 Random Case with Excluded Volume

### 3.4.1 General Discussion

There is an important difference between arrangement of atoms in real materials and arrangement of points in the random case. In real materials two atoms cannot be too close to each other. In other words, there is excluded volume around every atom in which there can not be another atom. Thus, in the random case, for a given finite density, the number particles inside the spherical annulus can vary, in principle, between zero and infinity. In the amorphous case, in contrast, the maximum number of particles inside the spherical annulus is limited by excluded volume.

In real materials, the excluded volume around every particle and the atomic number density of the material are closely related. However one can imagine a situation

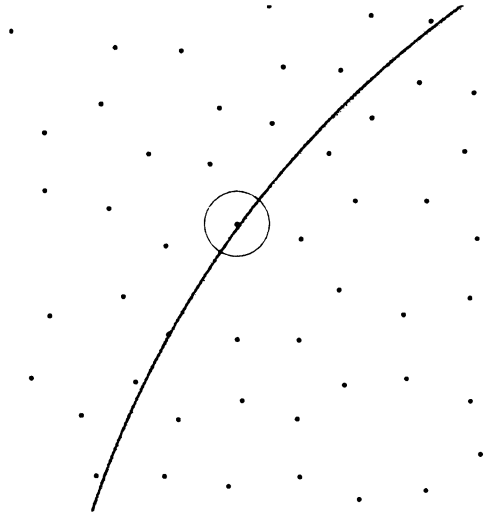


**Figure 3.8:** Only those points that are in  $\sigma$  vicinity of the distance  $r$  with respect to **site  $i$**  contribute to the value of  $G_i(r)$ . Excluded volume around every point reduces **the volume** accessible to the other points, that may want to enter the annulus due to **fluctuations**, and thus reduces the size size of fluctuations in the number of points.

**when** there is no direct relation between these two quantities. For example, we can **place** particles in some box randomly, but every new particle can be placed at some **point** only if there is no any other particle within some distance. Suppose that we **always** want to place the same number of particles in the box, so that density would be **the** same, but we want to vary the excluded distance. If the excluded distance is **small** enough we would be able to achieve our desirable density. However, as we **would** increase the excluded distance, it would be more and more difficult to find **the** configuration of sites that would satisfy both requirements: given density and **given** excluded volume. But if the excluded distance is too big we may not be able to **achieve** desired density. This problem is related to the so called problem of the **random** close packing of spheres[46, 47, 48].

Figure 3.7 shows an example of two distributions of sites with the same density **in** each of them. However, the excluded distance in the left half of the figure was **chosen** in such a way that excluded area covers 1/4 of the total area. The right half

of the figure shows distribution in which excluded area covers 1/2 of the total area.

As it was pointed out, the value of  $\langle G_{di}^2(r) \rangle$  is determined by the average size of fluctuations in the number of points inside the spherical annulus, i.e.  $\langle (N - \bar{N})^2 \rangle$ . If there is excluded volume around every point, then for any point that wants to enter the annulus due to some fluctuation, not the whole volume of the annulus is accessible: it is reduced by excluded volume of those points that are already in the annulus. Below we show that excluded volume decreases the value of  $\langle g_{di}^2(E) \rangle$  compared with the random case (3.16).

If the excluded volume around one site is  $V_{1f} \sim \lambda^d$  and there are  $\bar{N} \simeq \rho_o V$  sites inside the volume  $V$ , then the volume available for the placement of a new site is  $V - V_{1f}\bar{N}$  (in the random case it still would be  $V$ ).

Since, in order for the site  $j$  to contribute to the value  $G_{di}(r)$ , its distance from the site  $i$  should be  $\sim r \pm \sigma$ , we can say that site  $j$  should be within the volume  $V \sim \Omega_d r^{d-1} \sigma$  (see Fig.3.8). If inside this volume there is already one site, then accessible volume is reduced by  $V_{1f} \sim \gamma \lambda^{d-1} \sigma$ , where  $\gamma$  can be different for different structures. If there are  $\bar{N} = \rho_o V$  sites inside the annulus then the accessible volume  $V^*$  is reduced by  $V_{1f}\bar{N}$  compared with  $V$ , so that we have:

$$\begin{aligned} V^* &= V - V_{1f}\bar{N} \sim V - \gamma \lambda^{d-1} \sigma \cdot \rho_o V \\ &\sim V \left[ 1 - \gamma \lambda^{d-1} \sigma \cdot \frac{1}{\lambda^d} \right] = \Omega_d r^{d-1} \sigma \left[ 1 - \gamma \frac{\sigma}{\lambda} \right]. \end{aligned} \quad (3.17)$$

In comparison with the random case for which we had (3.14): for the amorphous case we write:

$$\langle [N - \bar{N}]^2 \rangle = \bar{N}^* = \rho_o V^*,$$

so that (compare with (3.15)):

$$\langle G_{di}^2(r) \rangle = \frac{\Omega_d r^{d-1} \sigma \rho_o [1 - \gamma \frac{\sigma}{\lambda}]}{\Omega_d^2 r^{d-1} \sigma^2} = \frac{1}{\Omega_d} \frac{\rho_o}{\sigma} [1 - \gamma \frac{\sigma}{\lambda}]. \quad (3.18)$$

Thus the presence of excluded volume in the amorphous case leads to the linear decay of  $\langle G_{di}^2(r) \rangle$  with an increase of  $\sigma$ . A more rigorous derivation made in Appendix (A.2) leads to (compare with (3.16)):

$$g_{di}^2(E) \cong \frac{1}{2\sqrt{\pi}\Omega_d} [1 - \gamma \frac{\sigma}{\lambda}]. \quad (3.19)$$

Results (3.18,3.19) were obtained in assumptions that  $\sqrt{(N - \bar{N})^2} \ll \bar{N}^*$  and that peaks corresponding to the different sites do not overlap, i.e.  $\sigma/\lambda \ll 1$ .

### 3.4.2 Results of Simulations in 2d

In order to verify numerically the role of excluded volume in 2d,  $N_p = 220 \times 220$  points were placed in the box of size  $[-110, 110]$  in  $x$  and  $y$  directions. The trial coordinates  $(x_i, y_i)$  of a particular point were generated using a random number generator. Point was placed at  $(x_i, y_i)$  if there was no any other point within the excluded distance  $2\xi$ . Otherwise a new attempt to generate coordinates of the point was made. This procedure was repeated until all  $N_p$  points were placed in the box. In the beginning, when the box is almost empty, points can be placed basically anywhere. As the box fills up it becomes more and more difficult to find suitable coordinates (empty space) in the box. The fraction of excluded volume to the total volume of the box can be found, if the concentration  $c = 1/\lambda^2$ , as  $S_f/S_{tot} = \pi\xi^2/\lambda^2$ . In our simulations  $\lambda = const = 1$ .

Then, for the particular choice of  $\xi$  (distribution), for all sites that were inside the central box of size  $[-50, 50]$  in  $x$  and  $y$  directions the PDF  $G_{2i}(r)$  was calculated for different values of peak width  $\sigma$ . The average value of  $g_{2i}^2 = \langle G_{2i}^2(r) \rangle / \sigma / \rho_o$  was



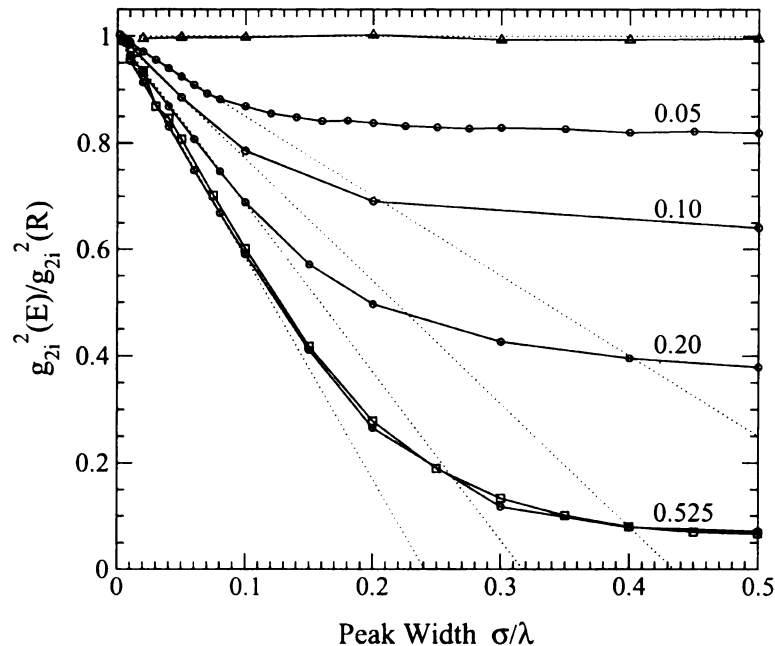


**Figure 3.9:** Dependence of  $g_{2i}^2(E)$  and  $g_{2i}^2(G)$  on  $\sigma$  for configurations with different excluded volumes. For the curves (with circles) shown, excluded volume covers 0.05 , 0.10, 0.20 and 0.525 of the total area of the box. The curve with squares corresponds to the amorphous distribution of sites. It basically coincides with the curve that has the fraction of excluded volume 0.525. The curve with triangles corresponds to completely random distribution.

found by averaging over the points that lay inside the central box. Our simulations show that  $g_{2i}^2(E)$  does not depend on  $r$ , which is in agreement with (3.19). At larger values of  $r > 20$  some size effects can be observed similar to those that occur in 3d (see description in 3d section).

Figure (3.9) shows the dependencies of the ratio of  $g_{2i}^2(E)$  to the constant exact (3.16) value  $g_{2i}^2(R)$  for the random case on  $\sigma/\lambda$  for values of excluded volume  $\pi\xi^2/\lambda^2$  equal to 0.05, 0.10, 0.20, 0.525.

It is interesting to compare results obtained from the random case with excluded volume with results obtained on some modeled amorphous structure. The curve with squares represents the results that were obtained on 3-fold coordinated network

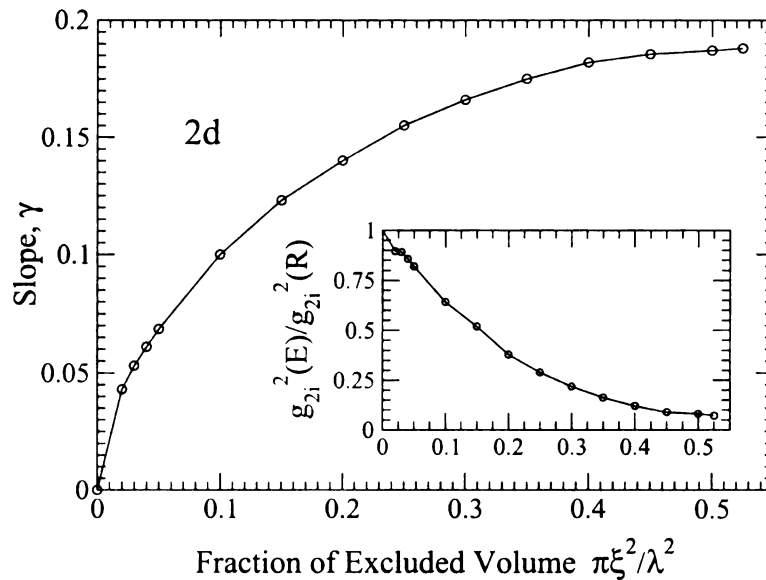


**Figure 3.10:** Dependence of the slope (linear part) of the curves  $g_{2i}^2$  versus  $\sigma$  (see Fig.3.9) on excluded volume. The value of excluded volume 0.525 is very close to the limiting accessible value. The inset shows how the ratio of the asymptotic value (large  $\sigma/\lambda$ ) of  $g_{2i}^2$  to the value of  $g_{2i}^2$  for the random case depends on excluded volume. Note the scale on the y-axis.

constructed from the honeycomb lattice by amorphizing it with an amorphization procedure similar to WWW method[49, 50]. The curve corresponding to the amorphous case basically coincides with the curve obtained on the random structure with the fraction of excluded volume 0.525. In order to obtain the data for amorphous case to the central box of size  $[-25.0;25.0]$  in  $x$  and  $y$  directions that contained 800 points periodic boundary conditions were applied. The averaging of  $G_{2i}^2(r)$  in the interval of  $r \in (5.0;15.0)$  was made over the 800 points that are inside of the central box. Although this approach has obvious shortcomings (see their discussion in 3d section), it seems, that obtained results are insensitive to them.

The curve with triangles shows the data with respect to the point at the origin while the others  $1000^2$  points were randomly distributed (zero excluded volume) in the box of size  $[-1000.0;1000.0]$  in  $x$  and  $y$  directions. The PDFs were calculated in

the interval of  $r \in (3.0; 7.0)$ . The averaging of  $G_{2i}^2(r)$  was made over 150,000 different configurations/distributions in order to calculate  $g_{2i}^2(R)$ .

As excluded volume increases, the absolute value of the curve's slope  $\gamma$  at small values of  $\sigma/\lambda$  also increases, while the asymptotic value of  $g_{2i}^2(E)$  reachable at large values of  $\sigma/\lambda$  decreases. We can see that  $g_{2i}^2(E)$  decreases linearly with  $\sigma/\lambda$  at small values of  $\sigma/\lambda$ , in agreement with (3.19). Figure 3.10 shows dependence of the slope  $\gamma$  and asymptotic (large  $\sigma$ ) values of  $g_{2i}^2(E)$  on forbidden volume.

The precision with which we determine the slope is about 5% of the value of the slope itself. Precision with which asymptotic value is determined is significantly lower  $\sim 20\%$ , since for the large values of  $\sigma/\lambda$  there occur only few oscillations in  $G_{2i}(r)$  on the interval of the studied distances. We used as an asymptotic value of  $g_{2i}^2(E)$  its value at  $\sigma/\lambda = 0.75$ .

The fact that  $g_{2i}^2(E)$  does not decay to zero at large values of  $\sigma/\lambda$  indicates that even in the case when there is excluded volume, the number of particles inside the spherical annulus can fluctuate, although fluctuations are limited. Due to the limited size of fluctuations, the value of  $g_{2i}^2(E)$  in cases when there is excluded volume is smaller than for the completely random case. The bigger excluded volume leads to smaller fluctuations and thus it results in a smaller value of  $g_{2i}^2(E)$ . Behavior of  $g_{2i}^2(E)$  at large values of  $\sigma/\lambda$  corresponds to the situation when peaks that originate from different points overlap. That is the limit when amplitude of atomic vibrations becomes comparable with interatomic distances.

### 3.4.3 Results of Simulations in 3d

Numerical simulations similar to those made in 2d can also be made in 3d. It is interesting to compare the results obtained for the random distribution of points limited by excluded volume with results obtained on some structure that represents some real amorphous material.

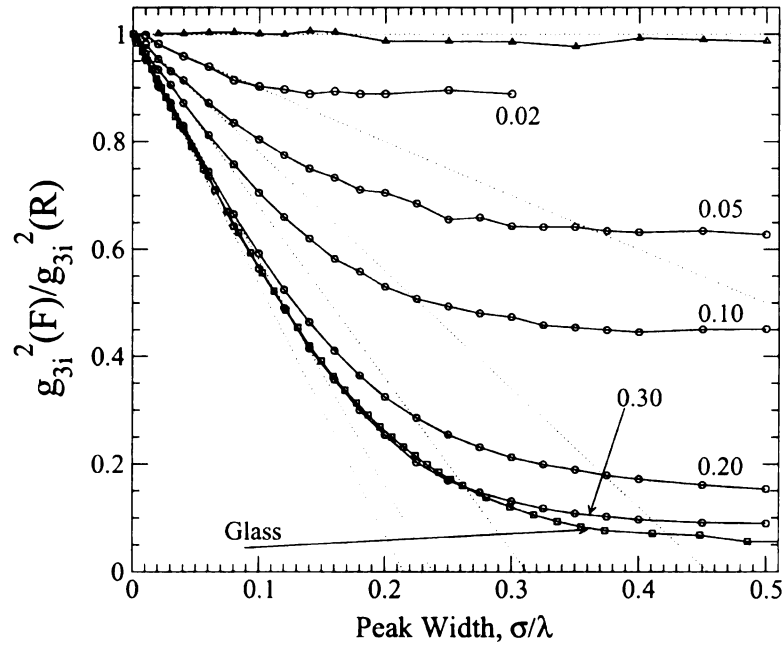


**Figure 3.11:** Dependence of  $g_{3i}^2(E)$  and  $g_{3i}^2(G)$  on  $\sigma$  for configurations with different excluded volumes. For the curves (with circles) shown, excluded volume covers 0.02, 0.05, 0.10, 0.20 and 0.30 of the total volume of the box. The curve with squares corresponds to the distribution of sites in amorphous Si. It basically coincides with the curve that has the fraction of excluded volume 0.35 (not shown). The curve with triangles corresponds to completely random distribution.

As a structure that represents a real material, we used the modeled structure of amorphous Si[51, 52]. In amorphous Si the average distance between the nearest atoms is  $\sim 2.5$  Å. Most of the simulations were made on the sample containing 20,000 atoms that occupy the cubic box of size  $[-36.23; 36.23]$  Å in  $x$ ,  $y$  and  $z$  directions. Periodic boundary conditions were applied to this box. The square of PDF  $G_{3i}(r)$  was calculated for all atoms in the original box. The average value  $g_{3i}^2(E)$  was found by averaging of  $G_{3i}^2(r)$  over 20,000 atoms. In order to find the dependence of  $g_{3i}^2(E)$  on  $\sigma$  calculations were made for different values of  $\sigma$ . The described method of calculation is not quite correct, because there are some predefined correlations in atomic positions due to periodic boundary conditions and the fact that contributions of some pairs of

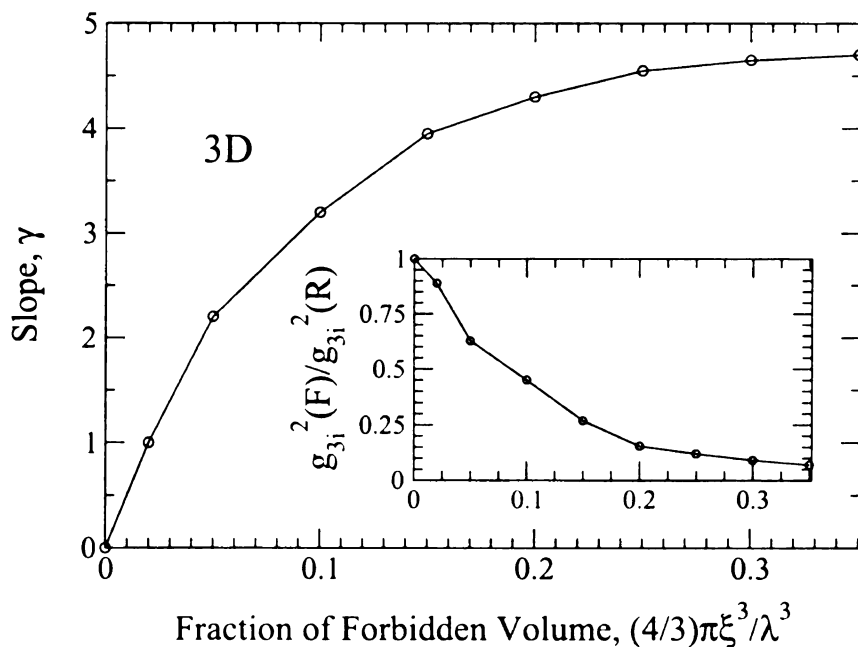


Figure 3.12: Dependence of the slope (linear part) of the curves  $g_{2i}^2$  versus  $\sigma$  (see Fig.3.11) on excluded volume. The value of excluded volume 0.525 is very close to the limiting accessible value. The inset shows how the ratio of the asymptotic value (large  $\sigma/\lambda$ ) of  $g_{2i}^2$  to the value of  $g_{2i}^2$  for the random case depends on excluded volume.

atoms to  $g_{2i}^2(E)$  are counted more than once. However, we repeated some of our calculations on a bigger sample containing 100,000 atoms without periodic boundary conditions. From that we conclude that the obtained results are not sensitive to the shortcomings of the used calculation procedure.

Coordinates of the points for the random case with excluded volume were generated using a random number generator by distributing  $90^3 = 729,000$  points in the box of size  $[-45.0; 45.0]$  in  $x$ ,  $y$  and  $z$  directions. A point was placed at generated coordinates if there was not any other point within excluded distance. Otherwise another set of trial coordinates was generated. Then from those points that were in the smaller box of size  $[-20.0; 20.0]$  (approximately  $40^3 = 64,000$ ) 10,000 points were randomly chosen. With respect to them  $G_{3i}(r)$  were calculated. We found that, as in 2d, the amplitude of oscillations in  $G_{3i}(r)$  is distance independent, if size effects are ignored. PDF  $G_{3i}(r)$  was averaged over these 10,000 points in order to find

$g_{3i}^2(E)$ . The value of  $g_{3i}^2(E)$  is constant at values of  $r < 10.0$ . At larger  $r$  values  $g_{3i}^2(E)$  slowly increases, which is the size effect caused by the finite size of the original box (finite number of points also limits the size of fluctuations). The last statement was verified by calculating  $g_{3i}^2(E)$  from the bigger box  $[-90.0;90.0]$  in  $x$ ,  $y$  and  $z$  with  $180^3 = 5,832,000$  points in it with the size of the small box still  $[-20.0;20.0]$  in  $x$ ,  $y$  and  $z$  directions. For this bigger box the increase in the value of  $g_{3i}^2(E)$  was smaller.

Figure 3.11 shows the dependencies of the ratio  $g_{3i}^2(E)/g_{3i}^2(R)$  (where, in the ratio, the numerator represents the value that was obtained from the random distribution with excluded volume and the denominator represents the value that was obtained for the purely random case) on  $\sigma/\lambda$  for different values of excluded volume. The curve that corresponds to the amorphous Si is also shown.

Figure 3.12 shows how the slopes at small values of  $\sigma/\lambda$  and asymptotic values at large values of  $\sigma/\lambda$  of the curves  $g_{3i}^2(E)/g_{3i}^2(R)$  depend on excluded volume  $(4\pi\xi^3)/(3\lambda^3)$ .

## 3.5 Crystals

### 3.5.1 General Discussion

Behavior of the PDF at large distances in crystals is the most intriguing. This case is also the most important because only in crystals can non-decaying behavior of the PDF be observed experimentally. Thus, if a crystal is formed by atoms of one type and all lattice sites are equivalent (in assumption that crystal structure is perfect) then there is no need to perform averaging (3.6) over different lattice sites since  $G_i(r)$  is the same for all of them, i.e  $G_i(r) = G(r)$ . The case of crystals also turns out to be the most complicated.

In this case we cannot say that points inside the annulus are randomly distributed, since points are fixed on the grid. Thus we can not use the same philosophy

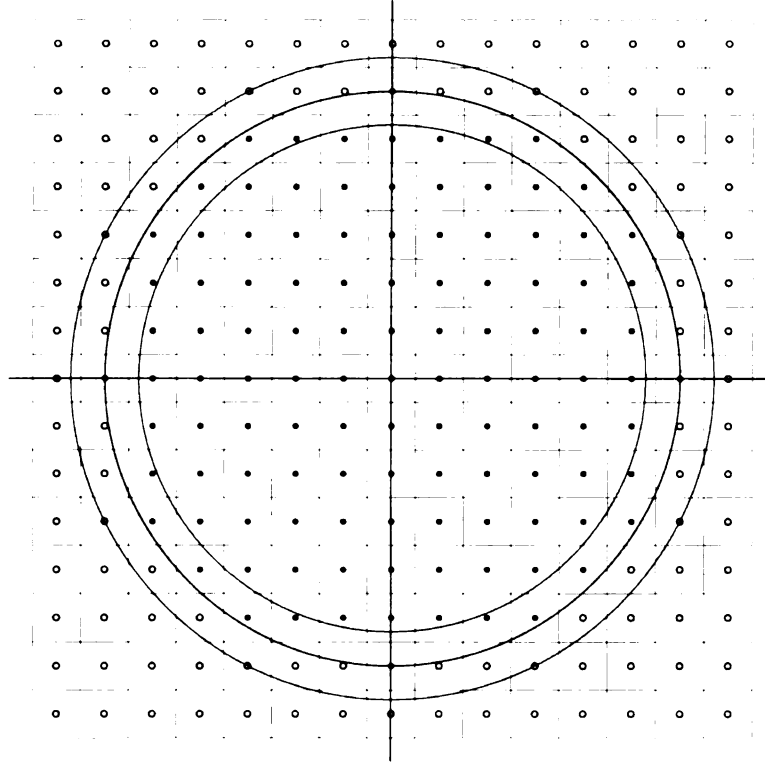


Figure 3.13: Illustration for the Gauss's circle problem. Sites that lie inside of the circle of radius  $r$  shown as black filled circles, while sites that lie outside of the circle of radius  $r$  as open circles. Only those sites contribute to the value of  $G_i(r)$  that are in  $\sigma$  vicinity of the distance  $r$  with respect to site  $i$ .

that was used for the random distribution of points to describe the case of crystals. However, as it will be shown, the geometry of the circle leads to some similarities between these two cases.

Behavior of PDF in crystals at large distance is related to complex and extensively studied mathematical area – so called lattice points theory. The problem is the most studied in 2d. More than a hundred years ago C.F. Gauss formulated the following problem[43, 44]: how many lattice points of the square lattice are there inside the of circle of radius  $r$  with the center at one particular point?

On Fig.3.13 lattice points that lie inside the circle of radius  $r$  are shown as small filled circles, while sites that lie outside are shown as small open circles.

Assume that every site of the lattice is in the center of the square with side  $a$ ,

as shown on the Fig.3.13. Thus, there is a correspondence between the area that lies inside of the circle of radius  $r$  and the number of lattice points inside of the circle. It is clear that the number of points inside of the circle can be written in the form  $N(r) = \overline{N}(r) + h(r)$ , where  $\overline{N}(r) = \pi(r^2/a^2)$ , and  $h(r)$  is the error term.

It is easy to see that Gauss's circle problem is related to the behavior of PDF. Let us use definition of PDF through bins (3.12). Then from the definition of PDF in 2d (3.7), if  $\delta \ll r$ , it follows that:

$$G(r) = [2\pi r \delta \rho(r) - 2\pi r \delta \rho_o] / (2\pi \sqrt{r} \delta), \quad (3.20)$$

while from definitions (3.12) of  $\rho(r)$  and  $\rho_o$  it follows that:

$$2\pi r \delta \rho(r) = [N(r + \delta/2) - N(r - \delta/2)] \quad (3.21)$$

and

$$2\pi r \delta \rho_o = [\overline{N}(r + \delta/2) - \overline{N}(r - \delta/2)]. \quad (3.22)$$

Thus:

$$G(r) = [h(r + \delta/2) - h(r - \delta/2)] / (2\pi \sqrt{r} \delta). \quad (3.23)$$

The simplest estimation of  $h(r)$  made by C.F. Gauss[43, 44] follows from Fig.3.13. All squares that correspond to the sites that are inside of the circle of radius  $r$  lie completely inside of the circle with radius  $r + d/2$ , where  $d = \sqrt{2}a$  is the diagonal of the little square. From the other side, the circle of radius  $r - d/2$  is completely covered by the squares that correspond to the sites that lie inside of the circle of



radius  $r$ . Thus, we conclude that:

$$\frac{1}{a^2}\pi(r - \frac{a}{\sqrt{2}})^2 \leq \pi(\frac{r}{a})^2 + h(r) \leq \frac{1}{a^2}\pi(r + \frac{a}{\sqrt{2}})^2,$$

i.e:

$$-\frac{1}{2}(\frac{2\pi r}{a}) + \frac{\pi}{2} \leq h(r) \leq +\frac{1}{2}(\frac{2\pi r}{a}) + \frac{\pi}{2}. \quad (3.24)$$

Formula (3.24) suggests that the value of the error term  $h(r)$  is determined by the length of the circumference:  $2\pi r$ . From (3.23,3.24) it follows that:

$$-\sqrt{2}\frac{\sqrt{r}}{a\delta} \leq G(r) \leq \sqrt{2}\frac{\sqrt{r}}{a\delta}. \quad (3.25)$$

We see that the obtained bounds for  $h(r)$  are very weak. If  $h(r)$  would depend on  $r$  as  $h(r) \sim r$  then  $G(r)$  would increase as  $\sqrt{r}$  while numerical simulations suggest, as follows from Fig.3.3 and as we will see further, that  $G(r) \sim \text{const}$  meaning that in fact  $h(r) \sim \sqrt{r}$ .

A number of works [53, 54, 55] were devoted to the more precise estimation of  $h(r)$ . In 1990 M.N. Huxley showed that [53]:

$$|h(r)| \leq Cr^\theta, \quad (3.26)$$

where  $C$  is a constant and the bounds on  $\theta$  are

$$\frac{1}{2} < \theta \leq \frac{46}{73} \approx 0.63. \quad (3.27)$$

The lower limit was obtained independently by G.H. Hardy and E. Landau in 1915[54, 55].

If  $\theta$  would be 1/2 it would be natural to expect that amplitudes of oscillations in

$G(r)$ , on average, are distance-independent. Since  $\theta > 1/2$  it indicates that extreme amplitudes of peaks in  $G(r)$  grow with the increase of distance  $r$ . One may argue that (3.26,3.27) basically put limitations on the extreme values of  $h(r)$ .

Thus (3.26,3.27) suggest that  $h(r)$  can exhibit, in principle, rather complicated distance-dependent behavior. However, results of our numerical simulations suggest that, on average, amplitudes of peaks in  $G(r)$  are almost distance independent. It means that  $\theta$  is almost  $1/2$ . Being more precise, it seems that,  $\theta$  being just a little bit bigger than  $1/2$  converges to  $1/2$  from above, as  $r \rightarrow \infty$ .

This observation is in agreement with result that was obtained in 1992 by P. Bleher who showed (we are not giving here precise formulation) that there exists a limit:

$$\lim_{R \rightarrow \infty} \frac{1}{R} \int_0^R \frac{h^2(r)}{r} p(r/R) dr = \alpha^2, \quad (3.28)$$

where  $p(x)$  is an arbitrary probability density on  $x \in [0, 1]$  and  $\alpha^2$  is a positive constant. This result suggests that there is also another limit that is important for us (see (3.23)):

$$\frac{1}{R_2 - R_1} \int_{R_1}^{R_2} G^2(r) dr = \tilde{\alpha}^2. \quad (3.29)$$

In the following sections, after the discussion of the exactly solvable 1d crystal, we present some puzzling results of our numerical simulations in 2d and 3d. Then we return to the general discussion again.

### 3.5.2 Exact Solution for 1d Crystal

According to definition of PDF in d-dimensions (3.7,3.8,3.9), in 1d:

$$G(r) = \rho(r) - \rho_o, \quad (3.30)$$

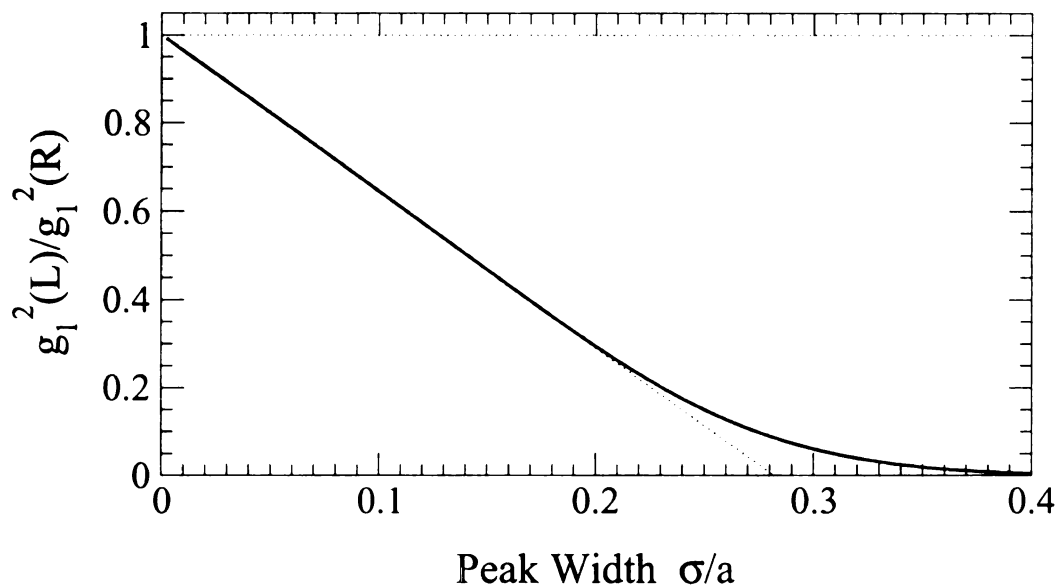


Figure 3.14: Figure shows the dependence of the ratio  $g_{1L}^2(\sigma)/g_{1R}^2(\sigma)$  on  $\sigma$ . At small values of  $\sigma$ , when different peaks in  $G(r)$  do not overlap, this ratio linearly decreases as  $\sigma$  increases. As peaks start to overlap (large values of  $\sigma$ ), the rate of decay in the average amplitude of PDF decreases.

where

$$\rho(r) = \frac{1}{\sqrt{2\pi\sigma^2}} \sum_{n=-\infty}^{\infty} \exp\left[-\frac{(r-na)^2}{2\sigma^2}\right] \quad (3.31)$$

and  $\rho_o = 1/a$ .

It can be shown (see appendix (A.3)) that for any value of  $\sigma$ :

$$\frac{g_{1L}^2(\sigma)}{g_{1R}^2(\sigma)} = \left[1 - 2\sqrt{\pi}\frac{\sigma}{a}\right] + \sum_{n=1}^{\infty} \exp\left[-\frac{n^2 a^2}{4\sigma^2}\right]. \quad (3.32)$$

This curve is plotted on Fig.3.14.

The last term in (3.32) can be ignored at small values of  $\sigma$ . As  $\sigma$  increases it changes the rate of decay in the average amplitude of PDF. Thus, behavior of the scaled amplitude  $g_{1L}^2(\sigma)/g_1^2(R)$  for 1d crystal is similar to the its behavior of in glasses (3.9,3.11).

### 3.5.3 Results of Simulations in 2d

In order to demonstrate that on average the amplitude of oscillations in  $h(r)$  indeed scales as  $r^{1/2}$  we calculated explicitly for the square lattice the number of lattice points inside the circle of radius  $r \in (0; 100,000)a$  with step  $0.01a$ , where  $a$  is the lattice spacing. We define function  $F(r)$  as [56]:

$$F(r) = \frac{N(r) - \overline{N}(r)}{\sqrt{r}}. \quad (3.33)$$

If  $h(r) \sim r^{1/2}$  then the amplitude of oscillations in  $F(r)$  on average should be constant.

Insets on the Fig.3.15 show  $F(r)$  vs.  $r$  dependence in three different intervals when  $r \in (0; 100,000)$ .

The values of  $F^2(r)$  were averaged over 100,000 different values in a few intervals of length  $1000a$ . The average value of  $\langle F^2(r) \rangle$  as a function of  $r$  is shown on Fig.3.15 as a dashed curve. Circles are plotted in the beginning and in the end of the corresponding averaging interval. From the vertical scale it follows that while  $r$  changes from 0 to 100,000 the average value of  $F^2(r)$  changes by less than 1%. From this we conclude that basically  $h(r) \sim r^{1/2}$ . There is also a slight increase in the value of  $\langle F^2(r) \rangle$  with  $r$ . This increase becomes slower as  $r$  increases. From that we conclude that  $\theta$  converges from above to  $1/2$  as  $r$  increases.

An example of PDF calculated for the square lattice in a continuous approach is shown on figure (3.5) as a dashed line. PDF calculated for triangular lattice exhibits similar behavior. In order to calculate  $g_2^2(L)$  (see (3.10,3.11) for the square and triangular lattices as a function of  $\sigma$ , the squares of corresponding PDFs were integrated (see (3.10)) in the interval of  $r \in (1000\lambda; 2000\lambda)$ . We should point out here again that the values of  $g_2^2(L)$  are very insensitive to the position of the averaging interval. Calculation in the interval  $r \in (300\lambda, 600\lambda)$  leads to almost the same results.

Figure 3.16 shows how, for the particular type of the lattice, the ratio of  $g_2^2(L)$  to

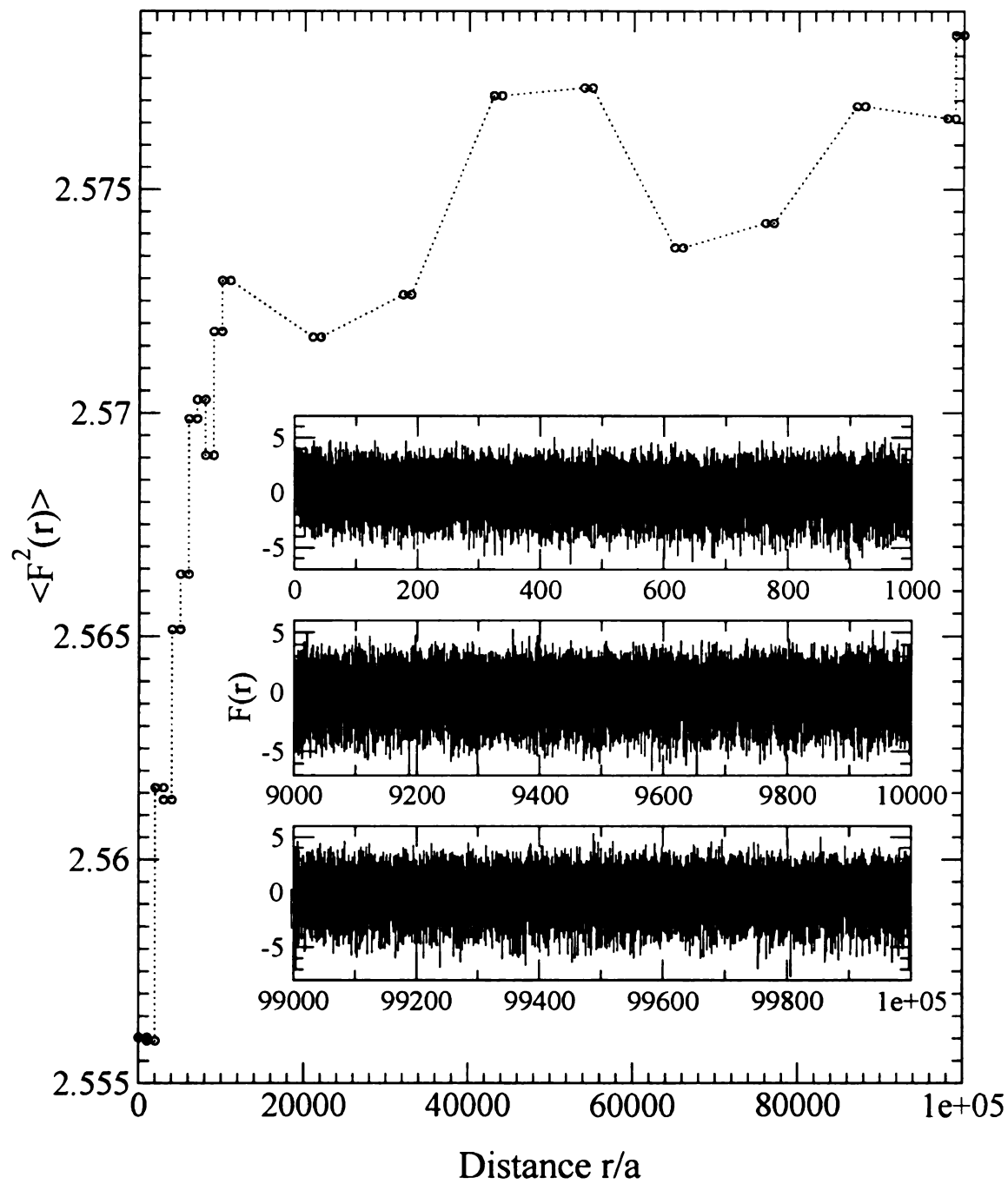


Figure 3.15: Inset shows how  $F(r)$  depends on  $r$  for  $r \in (0; 1000)a$ ,  $r \in (9000; 10,000)a$  and  $r \in (99,000; 100,000)a$ . It shows that on average amplitude of oscillations in  $F(r)$  does not depend on  $r$ . At least, it is impossible to see it by eye. The dashed curve on the main figure shows how  $\langle F^2(r) \rangle$  averaged over few intervals of  $r$  of length  $1000a$  depends on the position of the averaging interval. At the beginning and at the end of every averaging interval circles are plotted.

10  
5  
0  
10  
5  
0

$\mathbf{g}_2^2(\mathbf{L})/\mathbf{g}_{2i}^2(\mathbf{R})$

Figure 3.1  
times. The  
triangular  
formulas  
of  $\mathbf{g}_2^2(\mathbf{L})/\mathbf{g}_{2i}^2(\mathbf{R})$   
highlight the  
divergent  
terms of the  
effect of the

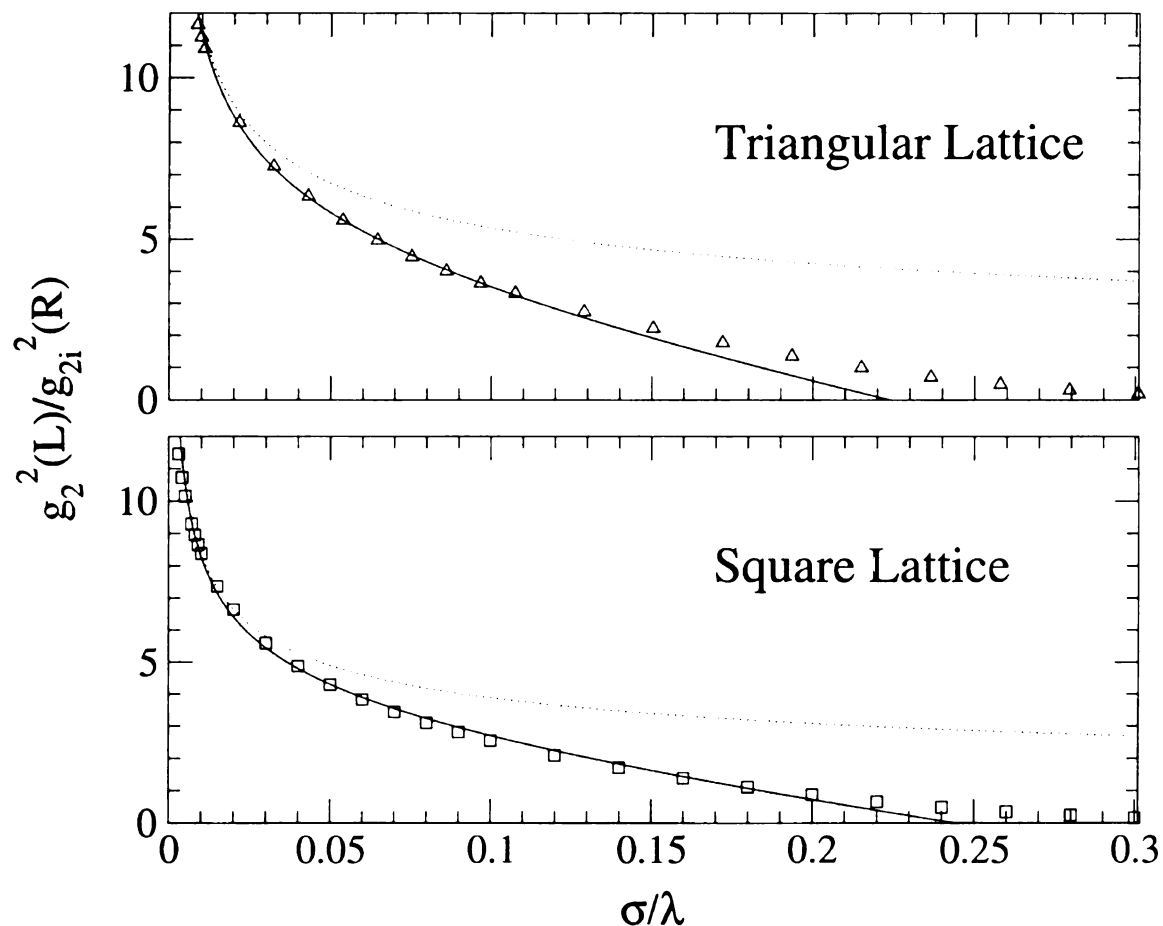


Figure 3.16: Dependencies of  $g_2^2(L)/g_{2i}^2(R)$  on  $\sigma/\lambda$  for triangular and square lattices. Triangles and squares represent the results of numerical calculations for triangular and square lattice respectively. The solid fitting curves are given by formulas  $g_2^2(tri)/g_{2i}^2(R) = 2.483(\sigma/\lambda)^{-1/3} - 18.264(\sigma/\lambda)$  for triangular lattice and  $g_2^2(sqr)/g_{2i}^2(R) = 1.849(\sigma/\lambda)^{-1/3} - 14.478(\sigma/\lambda)$  for square lattice. Dashed lines highlight the effect of excluded volume. Expressions for them are given by the first divergent term in the formulas for the solid curves. They do not contain the second term (that might be) caused by excluded volume. From the figure, it follows that the effect of the excluded volume is bigger for triangular lattice than for square lattice.

the  $g_1^2$

3.16

As

particu

$\mu_1^2$  or

are unli

Fi

vs.  $\sigma$  i

dom co

or in t

$g_1^2 R$

small

also.

$g_1^2 L$

large

V

when

form

term

also

as it

Li

prox



the  $g_{2i}^2(R)$ , where  $g_{2i}^2(R)$  is the exact constant value in completely random case (see (3.16)) depends on  $\sigma/\lambda$ .

As it was already pointed out  $g_2^2(L)$  being dimensionless can depend, for the particular type of the lattice, only on a dimensionless combination of  $\rho_o$  and  $\sigma$  i.e. on  $\rho_o\sigma^2$  or on  $\sigma/\lambda$  (see (3.11) with related text). Thus the curves presented on Fig.3.16 are universal for triangular and square lattices.

From (3.16,3.19,3.32), Fig.3.9,3.14 and Fig.3.16 it follows that behavior of  $g_2^2(L)/g_{2i}^2(R)$  vs.  $\sigma$  in case of 2d crystals is very different from its behavior in the completely random case or in the random case with excluded volume (the amorphous case too), or in the case of 1d crystal. In the random case this ratio is unity by definition ( $g_{2i}^2(R) = \text{const}$ ). In the random case with excluded volume it decays from unity (at small values of  $\sigma$ ) to some finite smaller value as  $\sigma$  increases, as it does for 1d crystal also. However, in the case of 1d crystal this ratio decays to zero. In 2d crystals  $g_2^2(L)/g_{2i}^2(R)$  diverges at small values of  $\sigma$  and it seems that it is decaying to zero at large values of  $\sigma$ .

We tried to fit numerical data with analytical curves in the form:

$$\frac{g_{2d}^2(L)}{g_{2i}^2(R)} = c_1\left(\frac{\sigma}{\lambda}\right)^{-\eta} - c_2\left(\frac{\sigma}{\lambda}\right), \quad (3.34)$$

where  $c_1, c_2$  and  $\eta$  are positive constants. The first term was chosen in the simple form that can provide divergence of  $g_2^2(L)/g_{2i}^2(R)$  at small values of  $\sigma$ . The second term originates from the notion that in the crystalline cases, in some sense, there is also excluded volume around every lattice point. Thus it was chosen in the same form as it is in the random case with excluded volume or in the amorphous case (3.19). In fact the form (3.34) provides a rather poor fit in 2d. However, the same form provides an extremely good fit in 3d case, as we will see.

For triangular lattice the values of coefficients that can provide the best fit in

the whole of

small value

$\eta = 0.245$

The  $s$

provide the

The values

$\eta = 0.245$

Note t

the square

is more de

volume to

square lat

larger th

indirect i

### 3.5.4

An

obtain, t

for and

$2000\pi$ .

averagi

Fl

tionho

We tri

in the

the whole studied range of  $\sigma$  are:  $c_1 = 2.483$ ,  $\eta = 1/3$  and  $c_2 = 18.264$ . However, at small values of sigma, different values of coefficients provide a better fit:  $c_1 = 3.742$ ,  $\eta = 0.245$  and  $c_2 = 43.433$ .

The situation with the square lattice is similar. The values of coefficients that provide the best fit in the whole range of  $\sigma$  are:  $c_1 = 1.849$ ,  $\eta = 1/3$  and  $c_2 = 14.478$ . The values of coefficients that provide a better fit at small values of  $\sigma$  are:  $c_1 = 2.806$ ,  $\eta = 0.245$  and  $c_2 = 33.410$ .

Note that the value of the coefficients  $c_2$  for triangular lattice is bigger than for the square lattice. That is in agreement with the observation that triangular lattice is more densely packed than square lattice. In other words, the ratio of excluded volume to the total volume of the sample for triangular lattice is bigger than for square lattice. Thus from Fig.3.9 it follows that  $c_2$  for triangular lattice should be bigger than for square lattice, as it is. This observation can be considered to be an indirect indication that the form of the second term in (3.34) is correct.

### 3.5.4 Results of Simulations in 3d

An example of PDF calculated for fcc lattice is shown on Fig.3.3. In order to obtain the values of  $g_3^2(L)$  as a function of  $\sigma$  the square of PDF was integrated for fcc and orthorhombic ( $b/a = 2.0$ ,  $c/a = 3.0$ ) lattices in the interval  $r \in (300\lambda; 300\lambda + 2000\sigma)$ , where  $\rho_o = 1/\lambda^3$  (obtained results are insensitive to the position of the averaging interval as in 2d).

Figure 3.17 shows how the ratio  $g_3^2(L)/g_{3i}^2(R)$  depends on  $\sigma$  for fcc and orthorhombic lattices. This ratio in 3d also diverges as  $\sigma \rightarrow 0$ , as it does in 2d. We tried to fit the data obtained from numerical calculations with the fitting curves in the form similar to the one used in 2d (3.34). We found that curves:

$$\frac{g_3^2(fcc)}{g_{3i}^2(R)} = 0.78\left(\frac{\sigma}{\lambda}\right)^{-1} - 20.0\left(\frac{\sigma}{\lambda}\right) \quad (3.35)$$

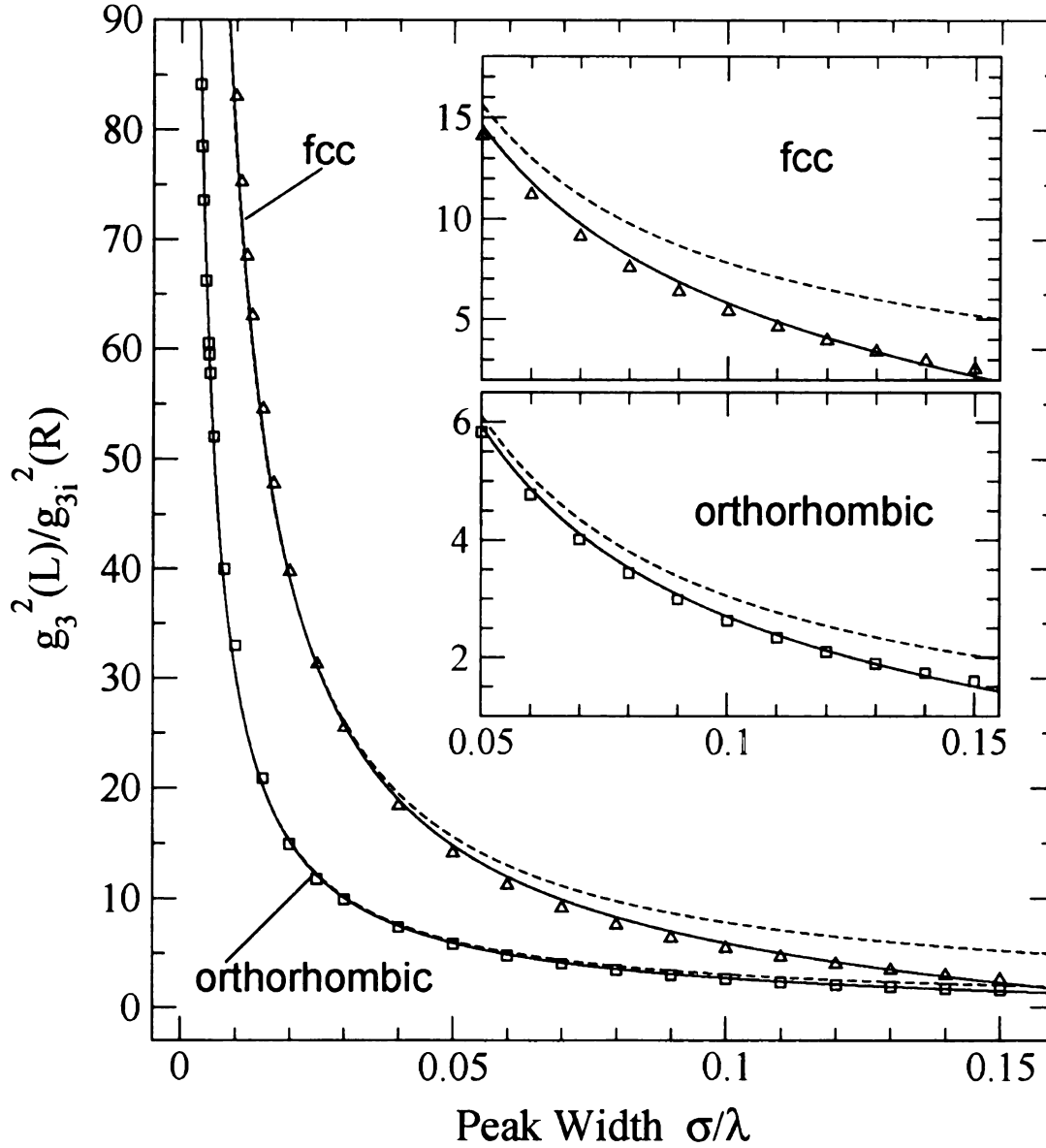


Figure 3.17: Results of numerical simulations for FCC and orthorhombic lattices. For rectangular lattice  $b/a = 2$  and  $c/a = 3$ . Points represent results of simulations. Solid fitting curves are given by formulas described in the text. Dashed lines highlight the effect of excluded volume. Expressions for them are given by the first divergent term in the formulas for the solid curves. Thus they do not contain the second term (that might be) caused by excluded volume. It can be seen from the figure that the effect of excluded volume is bigger for FCC lattice than for orthorhombic lattice.

for the last

for the first

Note

the bound

Since for

for the last

it should

We w

for a given

- A

### 3.5.5 S

In or

$< G^2$

Since

of the av

r-indepen

distribution

the annu

for fcc lattice and

$$\frac{g_3^2(ort)}{g_{3i}^2(R)} = 0.305\left(\frac{\sigma}{\lambda}\right)^{-1} - 3.5\left(\frac{\sigma}{\lambda}\right) \quad (3.36)$$

for orthorhombic lattice provide a good fit to the numerically calculated data.

Note that the value of the coefficient  $c_2$  for *fcc* lattice is bigger than for orthorhombic lattice. It is, as in 2d, in agreement with conception of excluded volume. Since fcc lattice is packed more densely than orthorhombic lattice, excluded volume for fcc lattice is bigger than for orthorhombic lattice. Thus according to Fig.3.11,3.12 it should be  $c_2(fcc) > c_2(ort)$ .

We would like to highlight again that the curves plotted on Fig.3.17 are universal for a given lattice, i.e. the ratio  $g_d^2(L)/g_{di}^2(R)$  indeed can depend only on the ratio  $\sigma/\lambda$ .

### 3.5.5 Speculations on the Origin of $\sigma$ -Divergence.

In order to find  $g_d^2(L)$  it is necessary to calculate an integral (3.10):

$$\begin{aligned} \langle G_d^2(r) \rangle &= \frac{1}{R_2 - R_1} \int_{R_1}^{R_2} G_d^2(r) dr \\ &= \frac{1}{R_2 - R_1} \int_{R_1}^{R_2} \{ [\Omega_d r^{d-1} \sigma \rho(r) - \Omega_d r^{d-1} \sigma \rho_o]^2 / [\Omega_d^2 r^{d-1} \sigma^2] \} dr . \end{aligned} \quad (3.37)$$

Since the value of the expression above (almost) does not depend on position of the averaging interval, the value of the last integrand should also be on average  $r$ -independent. We know that, in the case of random distribution of points, the fluctuations in the number of points inside of annulus is determined by the volume of the annulus or by the number of points in it (see (3.13,3.14,3.15)):

$$[\Omega_d r^{d-1} \sigma \rho(r) - \Omega_d r^{d-1} \sigma \rho_o]^2 \sim \Omega_d r^{d-1} \sigma \rho_o. \quad (3.38)$$

Thus for  $t$

Here  
that the  $s$   
annulus at  
or intern  
depend

So that for

Thus  
of points.

Fitting  
as (3.35.3)  
or  $\lambda_j^{-1/3}$

Howe  
sis (we a  
rather co  
necessary

Thus for the random case we would get:

$$g_d^2(R) = \langle G_d^2(r) \rangle \frac{\sigma}{\rho_o} \sim \frac{1}{\Omega_d} = \text{const.} \quad (3.39)$$

In crystalline case, when lattice points are fixed on the grid, it is natural to assume that the size of fluctuations is determined by position of the surfaces enclosing the annulus and thus basically by the surface area of the annulus. In principle, fluctuation on internal and external surfaces can be correlated. The size of correlations can be  $\sigma$ -dependent. Thus, for the case of crystals, we write:

$$[\Omega_d r^{d-1} \sigma \rho(r) - \Omega_d r^{d-1} \sigma \rho_o]^2 \sim \Omega_d r^{d-1} \lambda \rho_o \eta(\sigma/\lambda). \quad (3.40)$$

So that for crystals instead of (3.39) we would get:

$$g_d^2(L) = \langle G_d^2(r) \rangle \frac{\sigma}{\rho_o} \sim \frac{1}{\Omega_d} \left(\frac{\sigma}{\lambda}\right)^{-1} \eta_d(\sigma/\lambda). \quad (3.41)$$

Thus, if for the random case we had  $g_d^2(R) \sim \text{const}$ , for the ordered distribution of points, we can get divergence if, for example,  $\eta(\sigma/\lambda) \sim \text{const}$ .

Fitting curves for fcc and orthorhombic lattices in 3d (see Fig.3.35 with formulas (3.35,3.36)) suggest that  $\eta_3(\sigma/\lambda) \sim \text{const}$ . In 2d in order to obtain divergence  $(\sigma/\lambda)^{-1/3}$  (see Fig.3.16) we should assume that  $\eta_2(\sigma/\lambda) \sim (\sigma/\lambda)^{2/3}$ .

However, everything that is written in this section should be considered a hypothesis (we are not specialists in lattice point theory) and further investigation of this rather complicated problem, in connection with Gauss's circle problem, is obviously necessary.



### 3.5.6

In

on rate

similar

The

calculated

crystals

case of

with ex

distill

behavio

W

case at

crystals

As

behavio

for more

an abstr

experim

It is

formati

r. That

inside of

points th

of these

surface o

whose ed

### 3.5.6 Order and Disorder. Similarities and Differences.

In behaviors of PDF on crystals, on completely random distribution of points, on random distribution of points with excluded volume and on glasses there are some similarities, as well as differences.

Thus, in all of these structures amplitudes of oscillations in PDF that were calculated with respect to one particular site persist (or almost persist for the case of crystals) with an increase of distance. We understand the origin of this behavior in the case of completely random distribution of points and in case of random distribution with excluded volume. The case of glasses is very similar to the case of random distribution with excluded volume. We do not really understand the origin of this behavior in the case of crystals.

We also understand the dependence of the ratio  $g_{di}^2(E)/g_{di}^2(R)$  on  $\sigma$  in the random case and in random case with excluded volume (amorphous case too). The case of crystals again represents a puzzle.

As it was already pointed out, behavior of PDF in crystals is closely related to the behavior of the error term in Gauss's circle problem that remains under investigation for more than 150 years. It is interesting that this behavior that was (almost[57]) an abstract mathematical problem can be measured, in principle, in a real physical experiment.

It is clear that the size of oscillations in  $G_{di}(r)$  is determined by the size of fluctuations in the number of points near the surface of  $d$ -dimensional sphere of radius  $r$ . That is also true with respect to the behavior of  $h(r)$  in crystals, since points deep inside of the sphere are not subject to fluctuations. However, it is hard to say that points that are fixed on a grid participate in any kind of fluctuations. Thus the origin of these fluctuations, in case the crystals, lies in geometrical compatibility of the surface of the circle/sphere with its non-zero curvature and geometry of the lattice whose edges/faces have zero curvature.

Spher

connected

spherical

density  $\rho$

square and

through  $t$

as the radi

It is

stably tra

$G r = \sqrt{}$

PDF show

is also tra

oscillation

It is

be defined

contrary

PDF show

infinite  $\rho$

defined b

Thus

transition

Science t

Appara

Thus the

for the p

### 3.5.7 The Role of the Spherical Geometry.

Spherical geometry is basically imbedded into the definition of PDF due to its connection with diffraction experiments. However, in order to illustrate the role of spherical geometry, it is also possible to define triangular density  $\rho_{tri}(r)$  or square density  $\rho_{sqr}(r)$  (and so on ...) by counting the number of points inside triangular or square annuluses that are shown on Fig.3.18. Here we assume that PDF is defined through bins. The “radius” of the triangular density or square density can be defined as the radius of the circumference to which this square or triangle is inscribed.

It is almost obvious from Fig.3.18 that square density on the square lattice basically turns 2d problem into 1d problem. Thus PDF defined according to (3.7), as  $G(r) = \sqrt{r}[\rho_{sqr}(r) - \rho_o]$ , will diverge as  $r$  increases. In order to avoid divergence PDF should be defined, as in 1d, as  $G(r) = [\rho_{sqr}(r) - \rho_o]$ . It is not so evident, but it is also true with respect to triangular-pdf. Figure 3.19 shows that the amplitude of oscillations in  $[\rho_{tri}(r) - \rho_o]$  persist as  $r$  increases.

It is easy to see that if points are distributed randomly then PDF should always be defined (for any polygon) according to (3.7):  $G(r) = \sqrt{r}[\rho(r) - \rho_o]$ . On the contrary, if points form a lattice then for any polygon with finite number of edges PDF should be defined as  $G(r) = [\rho_{sqr}(r) - \rho_o]$ . But if the number of edges becomes infinite (circle) then PDF for the lattices should be defined in the same way as it is defined for the random distribution of points.

Thus it is the transition from a finite number of edges to the infinite one—transition from zero curvature of the edges to non-zero curvature of the circle’s circumference that makes random and ordered distributions of points somewhat equivalent. Appearance of this equivalence changes the way in which PDF should be defined. Thus the role of the spherical geometry (non-zero curvature) is extremely important for the properties of PDF.

Figure 3  
density  
and div

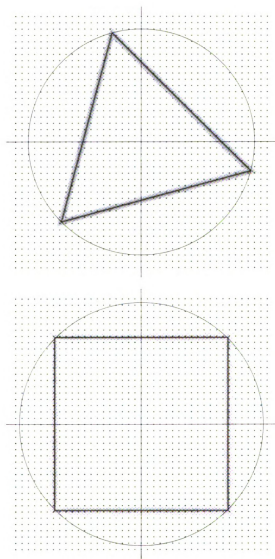


Figure 3.18: Triangular or square PDFs can be defined through triangular or square densities, i.e. by counting the number of points inside triangular or square annuluses and dividing this number by the area of the annulus.

Figure 3.1  
Large, S  
demonstra  
instead of

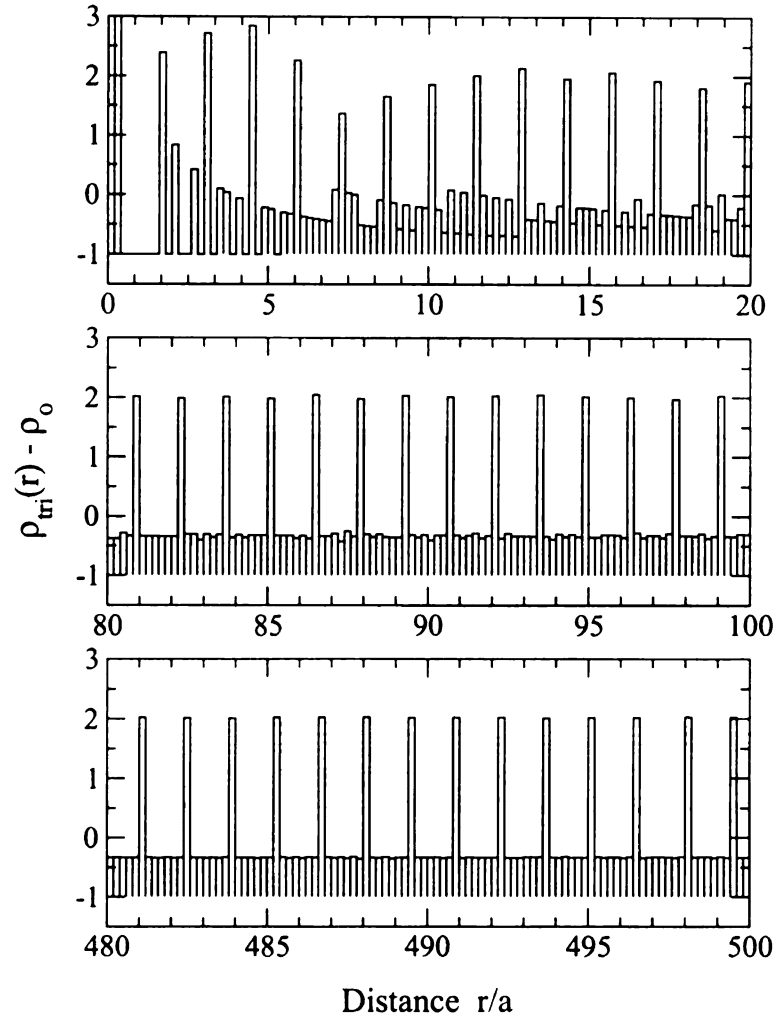


Figure 3.19: Dependence of  $\rho_{tri} - \rho_o$  on distance  $r/a$  for triangular PDF on square lattice. Since the amplitudes of oscillation persist as distance increases the figure demonstrates that the use of the polygons (any polygon can be divided into triangles) instead of the circle changes the way in which PDF should be defined.



Figure  
PDF of  
at 200

3.6

I  
exper  
May v  
Inc. Ch  
Trans  
enjoy

Ext.  
unlike

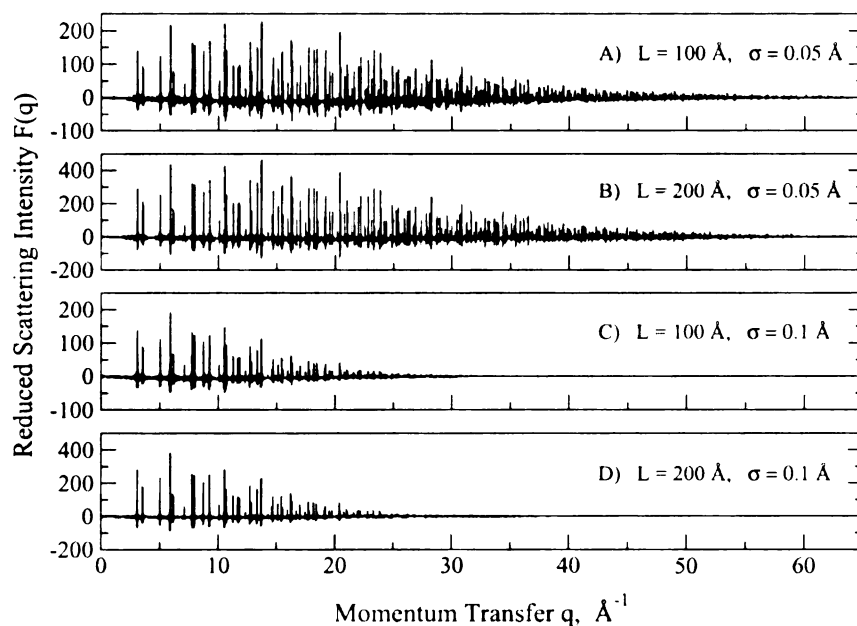


Figure 3.20: Reduced scattering intensity obtained by Fourier transformation from PDF calculated for the values of lattice parameters similar to those for the Ni crystal at 20K and 300K:  $a \simeq 3.53\text{\AA}$ ,  $\sigma_{20} = 0.05\text{\AA}$  and  $\sigma_{300} = 0.1\text{\AA}$ .

### 3.6 Perfect $S(q)$

The quality of the measured scattering intensity and, as follows from (3.1), of experimental PDF is limited by the finite instrumental resolution. However, one may want to calculate “perfect” scattering intensity, as it would be if instrumental resolution would be infinitely good. It can be done by performing inverse Fourier transformation of perfect PDF that can be calculated if lattice parameters and properties of atomic vibrations are known.

$$F(q) = \int_0^{R_{max}} G(r) \sin(qr) dr . \quad (3.42)$$

But, in the case of crystals, PDF does not decay at large distances and it becomes unclear at what maximum value of  $R_{max}$  integration should be terminated.

Figure 3.20 shows the reduced scattering intensity  $F(q)$  calculated from PDF

function

Narrate

Th

the value

A. The

termina

of  $\sigma =$

integrate

panel I

T

$Q_{\text{out}}$  a

$R_{\text{out}}$  a

with E

the sn

full os

alms

lead r

$q$  betw

I

of  $Q_{\text{out}}$

assum

PDF

than

function for the lattice parameters of the Ni crystal. It was assumed that atoms of Ni are arranged in the perfect FCC lattice and that  $\sigma$  is the same for all atomic pairs.

The panel A) shows  $F(q)$  calculated for the value of  $\sigma = 0.05 \text{ \AA}$  that is close to the value of  $\sigma$  for Ni at 20K. Integration was terminated at the value  $R_{max} = 100 \text{ \AA}$ . The panel B) shows  $F(q)$  calculated for the same value of  $\sigma$ , but integration was terminated at  $R_{max} = 200 \text{ \AA}$ . Panels C) and D) both were calculated for the value of  $\sigma = 0.1 \text{ \AA}$  which is close to the value of  $\sigma$  for Ni at room temperature. The integration was terminated at  $R_{max} = 100 \text{ \AA}$  for panel C) and at  $R_{max} = 200 \text{ \AA}$  for panel D).

Thus we see that although PDF does not decay,  $F(q)$  always decays. Moreover,  $Q_{max}$  at which occurs decay of  $F(q)$  is determined by  $\sigma$  and not by  $R_{max}$ . However,  $R_{max}$  affects the amplitude of the peaks: compare vertical scales on the panels A) with B) and C) with D). This behavior could be easily understood. The width of the smallest feature in PDF is given by  $\sigma$ . Thus if  $q$  is that big, that  $\sin(qr)$  makes full oscillation on the length  $\sim 2\sigma$ , contribution of any feature in PDF to  $F(q)$  would almost vanish. Thus  $Q_{max}2\sigma \sim 2\pi$  and  $Q_{max} \sim \pi/\sigma$ . Thus increase in  $R_{max}$  does not lead to the increase of  $Q_{max}$ , but develops the structure of  $F(q)$  in the fixed range of  $q$  between zero and  $Q_{max}$ .

This note is important in the sense that sometimes it is assumed that an increase of  $Q_{max}$  in experimental measurements would lead to a better quality of PDF. This assumption, in general, is wrong. If  $Q_{max} \sim \pi/\sigma$  then in order to obtain high quality PDF it is more important to improve instrumental resolution in the range  $q < Q_{max}$  than increase  $Q_{max}$ .

The  
 known to  
 the origin  
 in assu  
 differ in  
 crystals  
 crystals  
 even in  
 means  
 for very  
 the PD  
 and str  
 has a c  
 define  
 sites  
 origin  
 I do n  
 this pr  
 point

### 3.7 Conclusion

The PDF with respect to particular atom can not be measured by any presently known technique. In any experimental measurement, the averaging which places all at the origin is automatically performed. Thus, the pair distribution function calculated in assumption of infinite instrumental resolution only decays at large distances if different atoms at the origin have different atomic environments. Therefore for perfect crystals the pair distribution function does not decay. However even for perfect crystals the experimental PDF obtained from the diffracted scattering intensity will eventually decay at large distances due to the finite instrumental resolution. This means that the measured rate of decay of the measured pair distribution function for very good crystals could be used to test instrumental resolution. The decay of the PDF at large distances can also be used to investigate the sizes of nano-crystals and strained regions. The persistence of fluctuations in the pair distribution function has a connection to a value of the rms fluctuations for the Gauss circle problem in  $d$ -dimensions, thus providing a link between ordered and disordered distributions of sites. From my point of view it is important to have better understanding of the origin of this connection. Thus, this problem requires further investigation. However, I do not believe that we (by ourselves) would be able to move significantly forward with this problem due to the absence of sufficient knowledge in the area of the lattice point theory.

Ch

Qu

Di

cla

4.1

I

is a c

struc

least

7

form

corr-

I

extre

states

N

## Chapter 4

# Quantum correction to the Pair Distribution Function calculated classically.

### 4.1 Introduction

Recently, due to the subtleness of the protein folding problem especially, there is a demand for different techniques that will allow an accurate study of molecular structures and their dynamics, yet will not require time-consuming calculations, at least for relatively small molecules.

The pair distribution function (PDF), that can be obtained by Fourier transform of powder diffraction data, traditionally has been used to describe short-range correlations in atomic positions.

In recent years a technique has been developed that allows one to achieve an extremely good agreement between calculated and experimental PDFs for crystalline materials. [58, 36, 37].

Molecular Dynamics or Monte Carlo techniques are usually implemented in order



to st

ignit

quadr

hush

exper

and

calcu

calcu

for m

stud

comp

PDF

where

call-

MD

PDF

betwe

Pachu

Peak-

I

Start

of a p

Used

to study molecular structures and their dynamics. Thus, quantum effects are usually ignored. Other approaches, like the Car-Parinello method [59], that are based on quantum mechanics, are more time consuming than classical approaches and only feasible for a small number of atoms.

Accurate experimental PDFs can be obtained from X-ray or neutron diffraction experiments. Thus, in order to use PDFs to compare modeled molecular structures and their dynamics with real molecular structures and their motion, it is necessary to calculate molecular PDFs accurately. It is possible that PDFs obtained in classical calculations, in ignorance of QM effects, do not provide sufficient accuracy any more.

Thus, it is important to estimate the role of QM effects in calculations of PDF for molecules. Further, we will see that the accuracy of PDFs calculated using classical methods can be significantly improved without switching to QM calculations completely, but by implementing some quantum corrections to classically calculated PDFs.

It is known, that even at zero temperature, if it would be accessible, atoms would vibrate near their equilibrium positions due to the completely quantum effect that is called zero-point motion [62, 63]. This effect is completely missing in classical MC or MD calculations.

As was already discussed in the previous chapters, the width of the peaks in the PDF of solid materials is determined by the mean square deviation of the distance between a pair of atoms from its equilibrium value. Thus, at low temperatures especially, ignorance of zero point motion in classical calculations should result in a peak-width that is (significantly) smaller than the one that occurs in reality.

In this chapter the role of atomic zero point motion is discussed. The size of the effect is estimated by comparing the dependencies of the mean square displacements of a particle in the Morse potential on temperature in QM and CM calculations. We used a Morse potential because it was developed and proved to be useful in modelling

the pr

allow

and a

comp

beat

U

and

Alth

for t

with

corr

pair

PD

Inc

at

Or

be

QD

ti

ti

u

R

o

the properties of diatomic molecules. This potential is also convenient because it allows an exact QM solution. After that we develop a technique that allows to take into account the effect of zero point motion in PDFs calculated classically for more complex molecules. The same method is used to correct the classically calculated heat capacitance.

Usually, even in very simple molecules, there are different energy scales associated with the bond-stretching, angle-bending, dihedral angles rotations and so on. Although our correction can be applied to all pairs of atoms, it is the most important for those pairs that strongly interact with each other so that the energy associated with this pair (at a given temperature) is still almost the ground state energy of the corresponding vibrational mode. Thus, our correction is the most important for those pairs of atoms that bring sharp peaks into the PDF.

Molecules are usually in some environment that also contributes to the value of PDF at a particular distance. Often there are many molecules that form a liquid. Intermolecular interactions are usually much weaker than intramolecular interactions and thus they can be treated mostly classically, i.e. with MC or MD technique. In order to calculate accurately the PDF for a real sample it is necessary first of all to be able to calculate accurately the PDF for a single isolated molecule. That is the question that we address in this chapter.

Thus, our technique suggests the following algorithm for more accurate calculations of PDFs. The initial PDF can be extracted from classical MC or MD simulations that provide coordinates of atoms in a molecule as a functions of time, i.e. molecular trajectory. This modeled PDF already can be compared with the experimental PDF. Then, in order to achieve a better agreement between modeled and experimental PDFs, quantum correction can be applied to the PDF obtained from classical simulations.

In this chapter, we at first consider the case of exactly solvable Morse potential

for a di-

calculated

that Co

by clas

As

apply

correct

conting

equilib

be ass

exact

effect

the C

as ha

fixed

age t

figer

mode

traja

PDI

for a diatomic molecule. We use this example to demonstrate the precision of classical calculations of PDF and the importance of the quantum correction. Another quantity that can be corrected with our method is the heat capacitance that was calculated by classical methods.

After that, in an attempt to use our correction for more complex molecules, we apply our method to the  $C_6H_{14}$  molecule. At first we study the role of quantum corrections at very low temperatures when the molecule is in one of the equilibrium configurations and it can be assumed that the atoms only slightly vibrate about their equilibrium positions. If the amplitudes of atomic vibrations are small enough, it can be assumed that their motion is harmonic. In this case the problem could be solved exactly using either classical or quantum approaches. Thus, the role of quantum effects can be estimated at different temperatures. Finally, we calculate the PDF for the  $C_6H_{14}$  molecule at higher temperatures when the potential cannot be considered as harmonic any more and at even higher temperatures, when the molecule becomes flexible.

In our calculations we used the “TINKER” molecular dynamics simulation package that can search for equilibrium configurations and calculate eigenfrequencies and eigenvectors of molecular vibrations in these configurations. It was also used to run molecular dynamics simulations at a particular temperature. The obtained molecular trajectories (coordinates of atoms as a function of time) were used in calculations of PDF.

I

data v

where

$t$ -sin

used

C

PDF

scat

model

where

sample

power

length

value

I

realize

$d$  is

Shrink

whose

from v

## 4.2 Pair Distribution Function for a single molecule

The experimental PDF function  $G_{ex}(r)$  is obtained from the powder diffraction data via a sine Fourier transform of the normalized scattering intensity  $S(Q)$ :

$$G_{ex}(r) = \frac{2}{\pi} \int_0^\infty Q[S(Q) - 1] \sin(Qr) dQ \quad (4.1)$$

where  $Q$  is the magnitude of the scattering vector. For elastic scattering  $Q = 4\pi \sin \theta / \lambda$  with  $2\theta$  being the scattering angle and  $\lambda$  the wavelength of the radiation used.

On the other hand, the PDF is related to the structure of the material. The PDF is simply the bond length distribution of the material weighted by the respective scattering powers of the contributing atoms. It can be calculated from the structural model using the relation:

$$G_c(r) = 4\pi r \left\{ \left[ \frac{1}{4\pi r^2} \sum_i \sum_j \frac{b_i b_j}{\langle b^2 \rangle} \delta(r - r_{ij}) \right] - \rho_o \right\}, \quad (4.2)$$

where the sum goes over all pairs of atoms  $i$  and  $j$  separated by  $r_{ij}$  within the model sample. The scattering power of the atom  $i$  is  $b_i$  and  $\langle b^2 \rangle$  is the average scattering power of the sample. In the case of neutron scattering  $b_i$  is simply the scattering length, whereas in the case of X-rays it is the atomic form factor evaluated at a given value of  $Q$ . For  $Q = 0$  the value  $b_i$  is simply the number of electrons of atom  $i$ .

The first term in square brackets in (4.2) represents the radial density  $\rho(r)$  normalized in such a way that the number of atoms in the spherical annulus of thickness  $dr$  is given by  $4\pi r^2 \rho(r) dr$ . In solid materials, where atoms vibrate near their equilibrium positions  $\delta(r - r_{ij})$  functions in (4.2) should be substituted with Gaussians, whose width  $\sigma_{ij}^2$  is determined by the mean square deviation of the  $r_{ij}$  from its equilibrium value:  $\sigma_{ij}^2 = \langle (r_{ij} - \bar{r}_{ij})^2 \rangle$ . For our purposes it is convenient to define, instead



$\mathcal{G}$

we can

In ord

the pr

that w

S

the de

a m

by no

pair, t

can be

**4.3**

A

PDF

energ

form

moder

1

of  $G_c(r)$ , a different function  $g(r)$  to which we will refer to as the PDF. Summarizing we can write:

$$g(r) \equiv 4\pi r^2 \rho(r) = \sum_i \sum_j \frac{b_i b_j}{\langle b \rangle^2} \frac{1}{\sqrt{2\pi\sigma_{ij}^2}} \left\{ \exp \left[ -\frac{(r - \bar{r}_{ij})^2}{2\sigma_{ij}^2} \right] \right\} \quad (4.3)$$

In order to accurately calculate PDF it is necessary, in particular, accurately calculate the peak width  $\sigma_{ij}^2$  for the atoms that belong to the same molecule. That is the issue that we discuss in this work.

Substitution of  $\delta$ -functions with Gaussians occurs due to the time averaging of the distances between atomic pairs. If vibrations would not be small, for example if a molecule becomes flexible,  $\delta$ -functions should be substituted not by Gaussians, but by normalized probabilities to atoms in the pair at a given distance. For a particular pair, the shape of the probability function can be rather complicated. For example, it can contain several peaks that correspond to the different equilibrium configurations.

### 4.3 An example of Morse potential. The idea of the method.

Assume, for simplicity, that we are interested in an accurate calculation of the PDF for a diatomic molecule. Also assume that the only variable on which potential energy  $U$  depends is the deviation  $x = r - r_o$  of the distance  $r$  between the atoms from its equilibrium value  $r_o$ . If there is only one minimum in  $U = U(x)$  then the molecule has only one vibrational mode.

In the center of mass the Hamiltonian of the system can be written as:

$$H = \frac{p^2}{2\mu} + U(x), \quad (4.4)$$

where  $L$

in

imately

atoms

the ha

so that

It ca

prob

low

In st

same

Fi

Ne

where  $\mu = m/2$  is the reduced mass.

In the limits of low and high temperatures, this problem could be solved approximately. At low temperatures, when the deviation of the distance between the pair of atoms from its equilibrium value is very small, instead of the potential  $U(x)$  we use the harmonic approximation:

$$U_H(x) \simeq U_o + \frac{\mu\omega^2(x - x_o)^2}{2}, \quad (4.5)$$

so that we can write:

$$H = \frac{p^2}{2\mu} + \frac{\mu\omega^2(x - x_o)^2}{2}. \quad (4.6)$$

(It can be assumed, without changes in the results that  $U_o = 0$ ) The solution of the problem in the harmonic approximation is well known. The energy levels are given by:

$$E_n = \hbar\omega[n + \frac{1}{2}]. \quad (4.7)$$

In the harmonic potential the average values of kinetic and potential energies are the same:  $\langle E_{kin} \rangle = \langle E_{pot} \rangle = E_{tot}/2$ . Thus

$$\langle \frac{p^2}{2\mu} \rangle = \langle \frac{\mu\omega^2(x - x_o)^2}{2} \rangle = \frac{1}{2}\hbar\omega[\langle n(T) \rangle + \frac{1}{2}]. \quad (4.8)$$

From this we get:

$$\sigma_{HQM}^2(T) \equiv \langle (x - x_o)^2 \rangle = \frac{\hbar}{\mu\omega}[\langle n(T) \rangle + \frac{1}{2}], \quad (4.9)$$

where abbreviation HQM stands for Harmonic Quantum Mechanics. The Bose-

Enst

Expat

Thus

to A

to B

Wh

So

and

Einstein function  $\langle n(T) \rangle$  is given by:

$$\langle n(T) \rangle = \frac{1}{\exp\left[\frac{\hbar\omega}{k_b T}\right] - 1}. \quad (4.10)$$

Expanding this at high temperatures  $(\hbar\omega)/(k_b T) \ll 1$  we get:

$$\langle n(T) \rangle \cong \frac{k_b T}{\hbar\omega} - \frac{1}{2}, \quad (4.11)$$

Thus, at high temperatures:

$$\langle (x - x_o)^2 \rangle = \frac{\hbar}{\mu\omega} \frac{k_b T}{\hbar\omega} = \frac{k_b T}{\mu\omega^2} \quad (4.12)$$

If the spacing between the energy levels  $\Delta E = \hbar\omega$  is much smaller than  $k_b T$  (i.e.  $\hbar\omega/k_b T \ll 1$ ) the problem could be solved classically. In the last case, the probability to find the particle at some coordinate  $x$  is given by the Boltzman probability:

$$P_{CM}(x, T) = \frac{1}{Z_{CM}} \exp\left[-\frac{U(x)}{k_b T}\right], \quad (4.13)$$

where

$$Z_{CM} = \int \exp\left[-\frac{U(x)}{k_b T}\right] dx. \quad (4.14)$$

So that:

$$\langle x \rangle = \int x P_{CM}(x, T) dx, \quad (4.15)$$

and

$$\langle x^2 \rangle = \int x^2 P_{CM}(x, T) dx. \quad (4.16)$$

Thus

will

$Z =$

may

be

the

side

only

the

in

In

The

when

while

Thus:

$$\sigma_{CM}^2(T) = \langle (x - \langle x \rangle)^2 \rangle = \langle x^2 \rangle - \langle x \rangle^2 \quad (4.17)$$

could be found. In the harmonic case, ( $U(x) = \mu\omega^2(x - x_o)^2/2$ ):  $\langle x \rangle = x_o$ ,  $Z = \sqrt{2\pi k_b T / \mu\omega^2}$  and  $\sigma_{HCM}^2(T) = k_b T / \mu\omega^2$ , which is the same result as (4.12).

At higher temperatures, when the amplitudes of atomic vibrations are larger, it may not be appropriate to use the harmonic approximation for  $U(x)$ . Instead, it is necessary to solve the problem for the original potential  $U(x)$ . Again, as before, if the spacing between the energy levels is much bigger than  $k_b T$  the problem should be solved quantum mechanically. In the opposite limit  $\Delta E \ll k_b T$  the classical solution could be employed.

There is another potential  $U(x)$  that allows the exact QM solution. That is the Morse potential[64], which is widely used to model the properties of diatomic molecules:

$$\begin{aligned} U_M(x) &= -U_{min} + U_o \{1 - \exp[-\alpha x]\}^2 \\ &= (-U_{min} + U_o) + U_o [\exp[-2\alpha x] - 2\exp[-\alpha x]]. \end{aligned} \quad (4.18)$$

In this potential there is a finite number of the energy levels in the discrete spectrum.

The values of the energies are given by:

$$E_n = (-U_{min} + U_o) - U_o \left[1 - \frac{\alpha \hbar}{\sqrt{2mU_o}} \left(n + \frac{1}{2}\right)\right]^2, \quad (4.19)$$

where  $n$  runs over the positive integer values from zero to the maximum value at which the term in the square brackets is still positive.



Energy (eV)

Figure  
curve  
The  
been

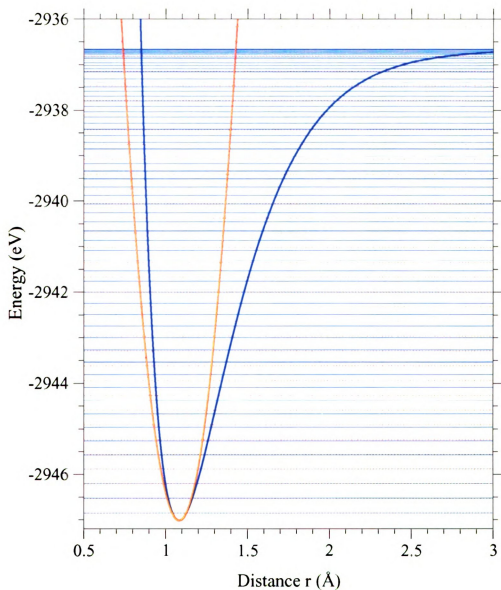


Figure 4.1: The blue curve shows the Morse potential for the  $N_2$  molecule. The red curve shows the harmonic approximation to the Morse potential at small values of  $x$ . The blue and red horizontal lines are the energy levels for the Morse and harmonic potentials respectively.

The

where

and

Final

before

In an

degree

part

when

The non-normalized wave functions are given by:

$$\psi_n(x) = \exp\left[-\frac{\xi^2}{2}\right] \xi^s w_n(\xi), \quad (4.20)$$

where

$$\xi = \frac{2\sqrt{2mU_o}}{\alpha\hbar} \exp(-\alpha x), \quad (4.21)$$

and

$$s = \frac{\sqrt{2mU_o}}{\alpha\hbar} - \left(n + \frac{1}{2}\right). \quad (4.22)$$

Finally  $w_n(\xi) = F(-n, 2s + 1, \xi)$  is the confluent hypergeometric function that can be found by the series:

$$\begin{aligned} F(\alpha, \gamma, z) = & 1 + \frac{\alpha}{\gamma} \frac{z}{1!} + \frac{\alpha(\alpha+1)}{\gamma(\gamma+1)} \frac{z^2}{2!} \\ & + \frac{\alpha(\alpha+1)(\alpha+2)}{\gamma(\gamma+1)(\gamma+2)} \frac{z^3}{3!} + \frac{\alpha(\alpha+1)(\alpha+2)(\alpha+3)}{\gamma(\gamma+1)(\gamma+2)(\gamma+3)} \frac{z^4}{4!} + \dots \end{aligned} \quad (4.23)$$

In our case, when  $\alpha = -n$ , the confluent hypergeometric function is a polynomial of degree  $n$ .

If the energy levels and the wave functions are known, the probability to find the particle at temperature  $T$  at position  $x$  is given by:

$$P_{QM}(x, T) = \frac{1}{Z_{QM}} \sum_{n=0}^{n_{max}} |\psi_n(x)|^2 \exp\left[-\frac{E_n}{k_b T}\right], \quad (4.24)$$

where

$$Z_{QM} = \sum_{n=0}^{n_{max}} \exp\left[-\frac{E_n}{k_b T}\right]. \quad (4.25)$$

Then <

and

Finally

In

low ten

For

69' with

where

If

417, v

being

operation

Then  $\langle x \rangle$  and  $\langle x^2 \rangle$  could be found as:

$$\langle x_{QM}(T) \rangle = \int x P_{QM}(x) dx, \quad (4.26)$$

and

$$\langle x_{QM}^2(T) \rangle = \int x^2 P_{QM}(x) dx. \quad (4.27)$$

Finally from (4.26,4.27) we get:

$$\sigma_{QM}^2(T) = \langle (x - \bar{x})^2 \rangle = \langle x_{QM}^2(T) \rangle - \langle x_{QM}(T) \rangle^2. \quad (4.28)$$

In these calculations the continuous spectrum was ignored. Thus, being exact at low temperatures these QM calculations should fail at very high temperatures.

For the harmonic potential, the sums (4.24, 4.25) could be explicitly calculated [63] with the following result:

$$P_{HQM}(x, T) = \left(\frac{\alpha}{\pi}\right)^{\frac{1}{2}} \exp[-\alpha x^2], \quad (4.29)$$

where

$$\alpha = \frac{m\omega}{\hbar} \tanh\left[\frac{\hbar\omega}{2k_b T}\right]. \quad (4.30)$$

If the temperature is high enough, instead the Boltzman probability (4.13, 4.14, 4.17) with  $U(x) = U_M(x)$  could be used to calculate  $\sigma^2$ . MC and MD simulations, being classical, produce  $\sigma^2$  that correspond to the Boltzman distribution at all temperatures. Thus, their results are not valid at very low temperatures.

$$p = \text{probability of } \text{log}(x)/2$$

For  
Inc  
W  
sh  
to

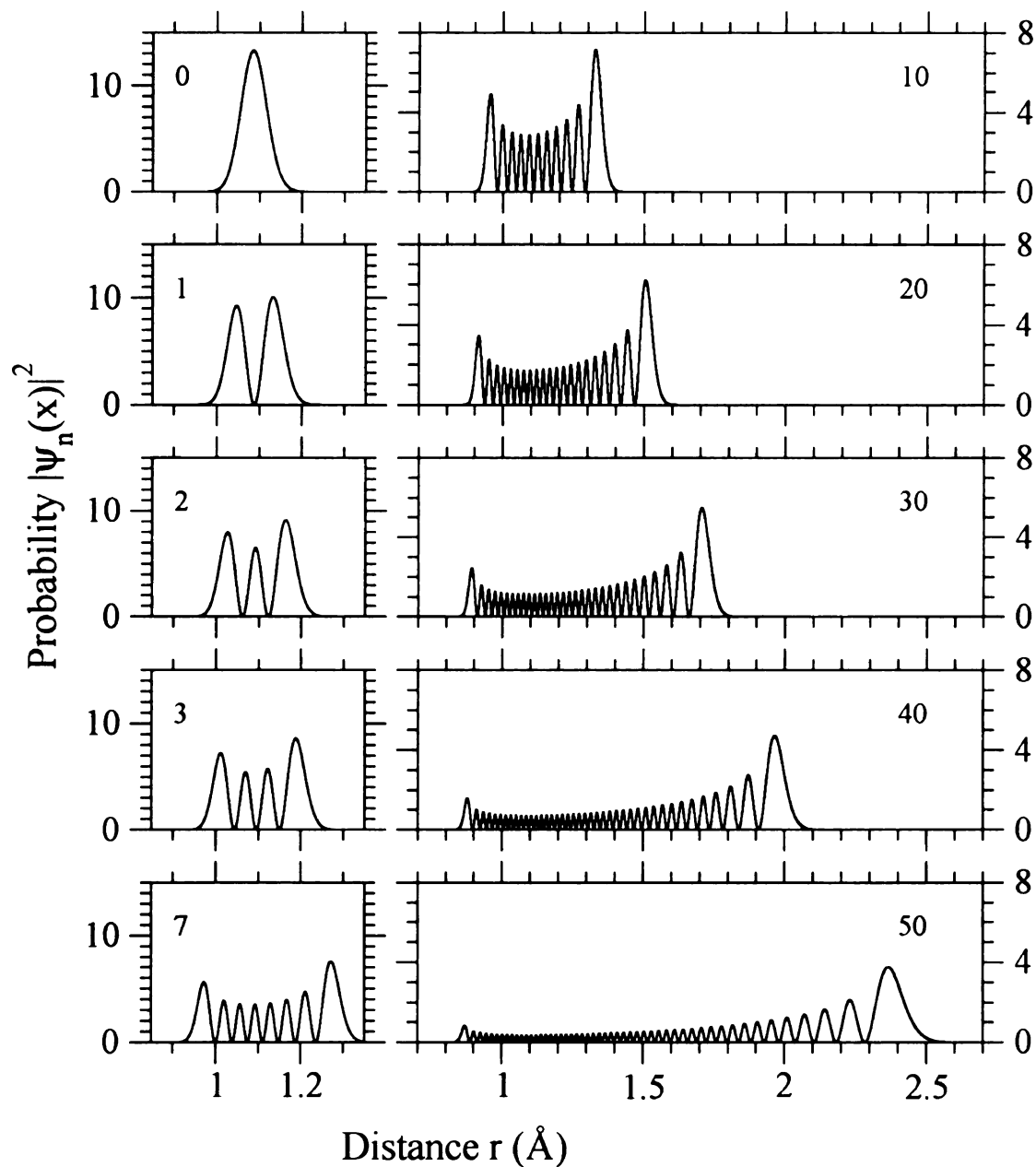


Figure 4.2: The squares of the wave functions of the Morse potential for the  $N_2$  molecule. The little figures on the left from the top to the bottom show normalized wave functions for  $n = 0, 1, 2, 3, 7$ . The figures on the right from the top to the bottom show normalized wave functions for  $n = 10, 20, 30, 40, 50$ . There are 61 energy levels for the chosen values of parameters.



A

N/m

It was

that w

istan

10828

optimi

calcul

inform

harmon

Vine h

red de

the us

T

mole

ate or

partic

due t

shifts

uniform

F

Potenti

moder

temper

almos

Energy

### 4.3.1 Molecule $N_2$

As an example, we consider the Morse potential  $U_M(x)$  parameterized for the  $N_2$  molecule. The blue curve on Fig.4.1 shows the corresponding Morse potential. It was obtained by performing calculations with the Gaussian98 [60, 61] program that was approximately solving the Shrödinger equation for the electrons when the distance between the nucleus of  $N$  atoms was fixed. The equilibrium distance  $r_o = 1.0828 \text{ \AA}$  and the equilibrium energy  $U_{min} = 2947.0188 \text{ eV}$  were found in a separate optimization run. In the same way, the energies  $E_N$  of the individual  $N$  atoms were calculated. Double of this energy is  $2E_N = -U_{min} + U_o = -2936.6608 \text{ eV}$ . This information is sufficient to construct Morse potential (4.18). The red curve is the harmonic approximation for the Morse potential at small values of  $x = r - r_{min}$ . The blue horizontal lines are the quantum energy levels of the Morse potential, while the red dashed lines are the energy levels of the corresponding harmonic potential. For the used values of parameters, there are 61 energy levels in the Morse potential.

The squares of the normalized wave functions of the Morse potential for the  $N_2$  molecule are shown in Fig. 4.2. The wave functions corresponding to  $n = 0, 1, 2, 3, 7$  are on the left and for  $n = 10, 20, 30, 40, 50$  are on the right. Thus, for small  $n$  the particle could be found only near the minimum of the potential  $r_o$ . As  $n$  increases, due to the asymmetry of the potential, the probability density, as well as  $\langle r \rangle$  shifts to the right, and thus the particle spends more and more time away from the minimum.

Figure 4.3 shows probabilities to find the particle at a given distance in the Morse potential and its harmonic approximation at different temperatures. For a diatomic molecule these probabilities represent the pair distribution function. At very low temperatures the CM results for Morse potential and its harmonic approximation almost coincide. However, the QM results are different. In QM, the ground state energies for the Morse and Harmonic potentials are separated from the bottom of the

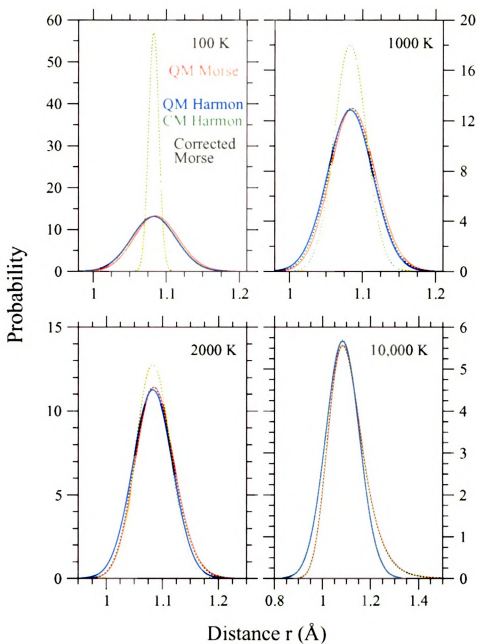


Figure 4.3: The Pair Distribution Functions or the probabilities to find the particle at a given distance in the Morse potential or its harmonic approximation at temperatures 100K, 1000K, 2000K and 10,000K. The red and orange curves represent QM (4.24,4.25) and CM (4.13,4.14) results for the Morse potential. The blue and green curves represent QM and CM results for the harmonic approximation to the Morse potential. The black curves represent CM results for the Morse potential corrected by the convolution (4.34) with  $\sigma_{corr}^2$  obtained from the harmonic approximation to the Morse potential.

poter

of th

leads

harm

PDFs

poter

I

in fo

Mors

over

is not

the fi

428

orang

413.

417

QM

N

conce

both

zero-

tempe

C

that v

lead

obtain

F

potential by finite (slightly different) energy values. Because of it the anharmonicity of the Morse potential is reflected even in the ground state of the particle. This leads to the slightly different PDFs that were obtained using QM on the Morse and harmonic potentials. At temperature 10,000K the non-Gaussian line shape of the PDFs obtained on the Morse potential are well pronounced. The depth of the Morse potential corresponds to  $\approx 100,000$  K

Figure 4.4 shows dependencies of  $\sigma^2(T)$  on temperature  $T$  that were calculated in four different ways. The red curve shows the result of the QM calculation for the Morse potential, where the summation in (4.24,4.25) were performed (numerically) over the 61 energy levels. At the temperatures plotted  $T < 10,000$  K this result is not any different from the result that could be obtained by the summation over the first 35 energy levels. Thus, it can be assumed that the range of integration in (4.28) is  $(-\infty, \infty)$ , while for the calculation the range  $(0.5, 2.5)$  Å was used. The orange curve shows the result of CM calculations of  $\sigma^2(T)$  for the Morse potential (4.13,4.14,4.17). There is a subtle point concerning the range of the integration in (4.17). This question is discussed in Appendix B. The blue and green curves show QM (4.9) and CM (4.12) results for the harmonic potential.

Note that  $\sigma_{CM}^2(T)$  calculated classically for the Morse and Harmonic potentials, converges to zero as  $T \rightarrow 0$ . In contrast,  $\sigma_{QM}^2(T)$  calculated by QM methods for both potentials converge to a finite non-zero value as  $T \rightarrow 0$ . This is the effect called zero-point motion. In other words, atoms in QM are not motionless even at zero temperature.

Classical MD or MC simulations performed on the Morse and Harmonic potentials would lead to the orange and green curves respectively. Thus, classical methods lead, especially at low temperature, to significantly incorrect results. In order to obtain the correct results, it is necessary to use the QM approach.

Potentials that are used to model molecular motion for complicated molecules

Peak Width  $\sigma^2$  ( $\text{\AA}^2$ )

Figure  
differ-  
444.4  
and C  
black c  
comes

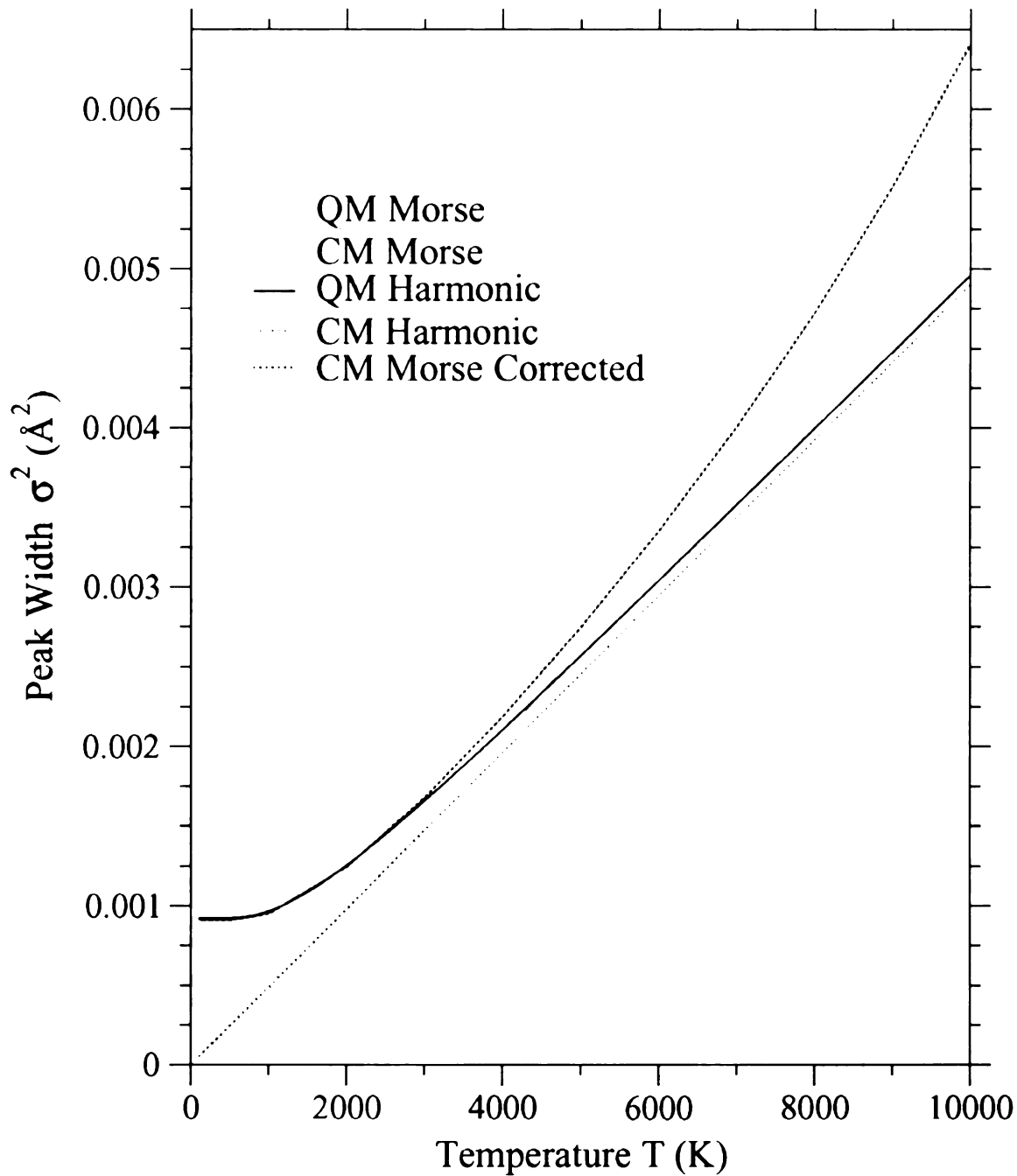


Figure 4.4: The dependencies of  $\sigma^2$  on temperature  $T$  that were calculated in four different ways. The red and orange curves show QM (4.24, 4.25, 4.28) and CM (4.13, 4.14, 4.17) results for the Morse potential. The blue and green curves show QM (4.9) and CM (4.12) results for the harmonic approximation to the Morse potential. The black curve shows the CM results on the Morse potential with correction (4.31) that comes from the harmonic approximation to the Morse potential.

do not

to sch

ration

it is p

is not

appea

MC s

Thus

such

result

track

0

when

data

to th

for t

stat

temp

temp

temp

2. 1

repr

that

Our

repr



do not allow exact QM calculations. The harmonic approximation still could be used to solve the problem at low temperatures. It can be employed if equilibrium configurations, vibrational frequencies and vibrational eigenvectors are known. In this case, it is possible to obtain both QM and CM solutions. But the harmonic approximation is not valid in the most interesting regime when more complex molecular motions appear due to the anharmonicity of the real potential. On the other hand, MD and MC simulations allow to take into account the anharmonicity of the real potential. Thus it would be valuable to find a way to correct the results of the CM calculation in such a way that at very low temperatures the corrected results would reproduce the results of low temperature QM calculations, while at high temperatures they would track the anharmonicity of the real potential.

Consider the following expression:

$$\sigma^2(T) = \sigma_{CM}^2(T) + [\sigma_{HQM}^2(T) - \sigma_{HCM}^2(T)], \quad (4.31)$$

where under  $\sigma_{CM}^2(T)$  we mean the CM results on some potential  $U(x)$  that could be obtained from the Monte Carlo or Molecular Dynamics simulations and thus sensitive to the anharmonicity of the real potential. Under  $\sigma_{HQM}^2(T)$  we mean the QM solution for the harmonic approximation to  $U(x)$  in the vicinity of  $r_o$ . Finally  $\sigma_{HCM}^2(T)$  stands for the CM solution for the harmonic approximation to  $U(x)$ . At very low temperatures,  $\sigma^2(T) = \sigma_{HQM}^2(T)$ , since  $\sigma_{CM}^2(T) \simeq 0$  for the both potentials. As the temperature increases, see Fig.4.4, the difference of the two terms in square brackets in (4.31) decreases and thus becomes:  $\sigma^2(T) \simeq \sigma_{CM}^2(T)$ . Thus, the form (4.31) reproduces the correct behavior of the *real*  $\sigma^2(T)$ . It follows from Fig.4.4 that results that were obtained using CM on the Morse potential, and corrected by (4.31), the corrections that comes from the harmonic approximation to the Morse potential, reproduce the exact QM solution to the Morse potential in the whole range of the

resol-

In  
simila  
in ord

Thus  
origin  
in it v  
while

I  
around  
from  
the co

where

In 4  
Pair o  
PDF  
The

reasonable temperatures rather well.

In general the line shape of the PDF for a pair of atoms obtained in MD or MC simulations is not Gaussian. Thus the correction (4.31) could not be applied directly in order to correct (4.3) since the  $\sigma_{ij}^2$  are not known. It is known that:

$$\begin{aligned} \int_{-\infty}^{\infty} \frac{1}{\sqrt{2\pi\sigma_1^2}} \exp\left[-\frac{(r-r')^2}{2\sigma_1^2}\right] \frac{1}{\sqrt{2\pi\sigma_2^2}} \exp\left[-\frac{(r_o-r')^2}{2\sigma_2^2}\right] dr' \\ = \frac{1}{\sqrt{2\pi(\sigma_1^2 + \sigma_2^2)}} \exp\left[-\frac{(r-r_o)^2}{2(\sigma_1^2 + \sigma_2^2)}\right]. \end{aligned} \quad (4.32)$$

Thus, the convolution (4.32) of one Gaussian with another increases the width of the original Gaussian. If instead of one Gaussian another function that has some peak in it would be used, then the convolution still would increase the width of the peak, while the height would decrease.

In MC or MD simulations, the distance between a pair of atoms would oscillate around some average value, at low enough temperatures. Thus, the PDF obtained from MC or MD simulations would represent some distribution with a peak. Thus the correction (4.31) still can be applied by the convolution:

$$G(r) = \int G_{MD}(r') \frac{1}{\sqrt{2\pi\sigma_{corr}^2}} \exp\left[-\frac{(r-r')^2}{2\sigma_{corr}^2}\right] dr'. \quad (4.33)$$

where *the correction width* is given by:

$$\sigma_{corr}^2(T) = [\sigma_{HQM}^2(T) - \sigma_{HCM}^2(T)]. \quad (4.34)$$

In (4.33, 4.34)  $G_{MD}(r')$  stands for the PDF (distribution of distances) of the atomic pair obtained from the MC or MD simulations and  $G(r)$  stands for the corrected PDF. The weighted sum over the different pairs leads to the corrected PDF (4.3). The black dashed curves on Fig.4.3 show the CM results on the Morse potential (4.13,4.14) corrected by the convolution (4.33,4.34).

I  
the of  
total  
could

where

I  
as the

The

will

when

first

### 4.3.2 Correction to the heat capacity

The same philosophy that was used to correct  $\sigma^2(T)$  could be used to correct the classically calculated heat capacity. According to QM, the average value of the *total* energy of an oscillator (a diatomic molecule) in a potential (Morse or Harmonic) could be found as:

$$\langle E_{QM}(T) \rangle = \frac{1}{Z_{QM}} \sum_{n=0}^{n_{max}} E_n \exp\left[-\frac{E_n}{k_b T}\right], \quad (4.35)$$

where  $Z_{QM}$  is given by (4.25).

In the classical approach, the average value of the total energy could be found as the sum of the average values of kinetic and potential energies:

$$\langle E_{CM}(T) \rangle = \langle K(T) \rangle + \langle U(T) \rangle. \quad (4.36)$$

The value of the kinetic energy at temperature  $T$  is given by [63]:

$$\langle K(T) \rangle = \frac{1}{2} k_b T, \quad (4.37)$$

while the average value of the potential energy could be found as [63]:

$$\langle U(T) \rangle = \frac{1}{Z_{CM}} \int U(x) \exp\left[-\frac{U(x)}{k_b T}\right] dx, \quad (4.38)$$

where  $Z_{CM}$  is given by (4.14). See Appendix (B) on the integration range.

If the average value of the total energy for a diatomic molecule is known as a function of temperature, then the vibrational heat capacity could be found as:

$$C(T) = \frac{dE(T)}{dT}. \quad (4.39)$$

Again, as we did in (4.31), we can consider the correction of the CM results for the Morse potential by using the results from the harmonic approximation to the Morse potential:

$$E(T) = E_{MCM}(T) + [E_{HQM}(T) - E_{HCM}(T)]. \quad (4.40)$$

Figure 4.5 shows the dependence of the total average energy for a particle in the Morse and Harmonic potentials. The values of parameters are the same that were used to obtain Fig.4.4. The red and orange curves were calculated via the QM (4.35,4.25) and CM (4.36,4.37,4.38) for the Morse potential. The blue (QM) and green (CM) curves were calculated for the harmonic approximation to the Morse potential. The fact that the corrected curve is very close to the exact QM solution obtained on the Morse potential shows that this correction method also works well for the average energy in a wide range of temperatures.

Note that in the limit of zero temperature there is a small difference between the curves that represent QM solutions for the Morse and Harmonic potentials. This difference is caused by the fact that there is a very small difference between the first few energy levels of the Morse and Harmonic potentials, i.e. the energy of the ground state of the Morse potential is not exactly the energy of the ground state of the Harmonic potential.

The curves that represent CM solutions for the Morse and Harmonic potentials coincide exactly in the limit of zero temperature as they should. As temperature increases the CM Morse curve deviates from the CM Harmonic curve. In the limit of very high temperature this classical solution for the Morse potential should coincide with the QM solution (exact) for the Morse potential.

Thus, the corrected curve (black dots) coincides with the QM harmonic curve at very low temperatures (limit of zero temperature), while at high temperatures it

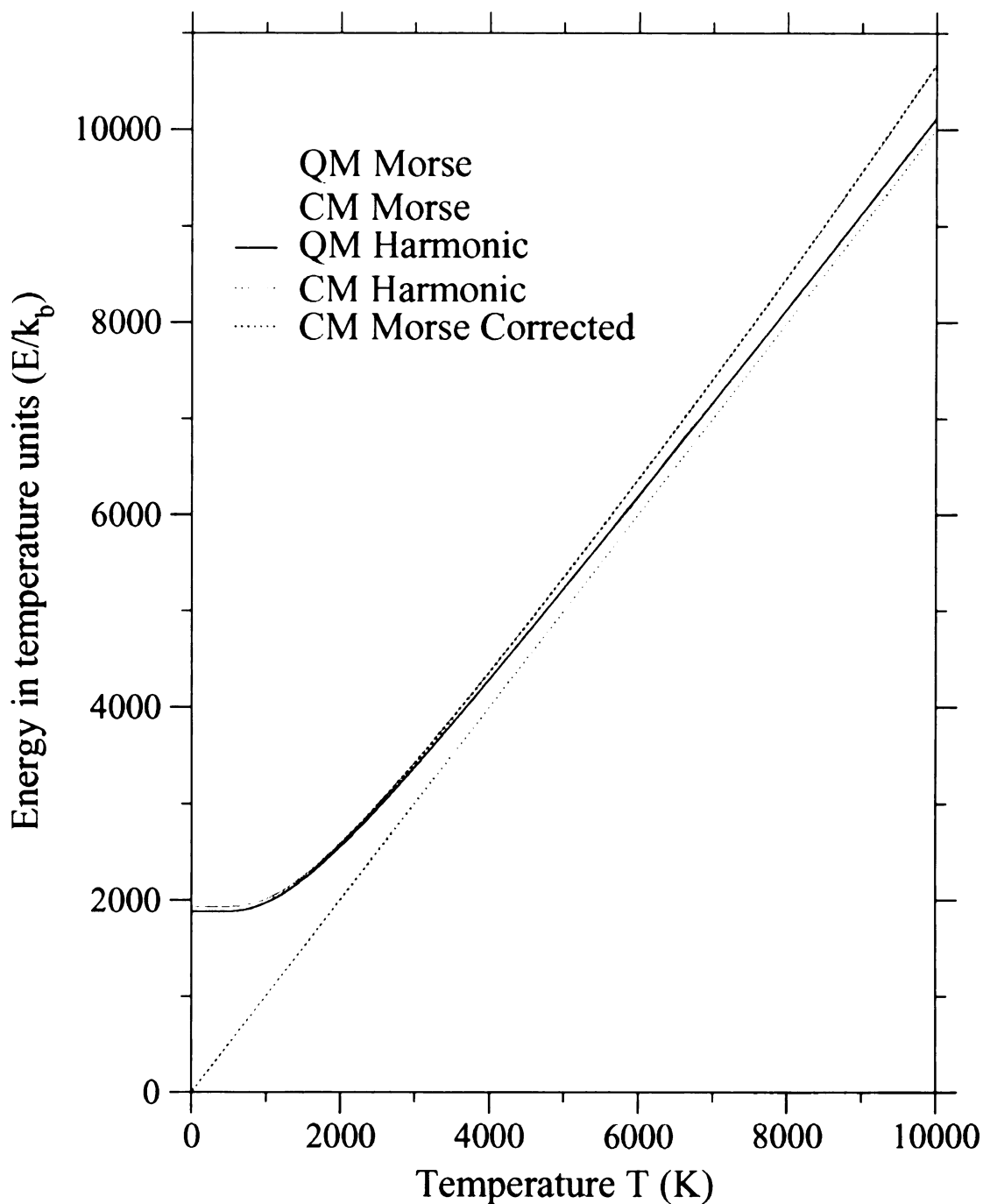


Figure 4.5: Average energies for a particle in the Morse potential and its harmonic approximation as a function of temperature. The red and orange curves represent the QM and CM solution for the Morse potential. The blue and green (dashed) curves show the QM and CM solutions for the harmonic approximation to the Morse potential. The black dashed curve shows the CM solution for the Morse potential with correction (4.31) that comes from the harmonic approximation to the Morse potential. It is assumed that  $U_o = 0$ .

coincides with the QM solution for the Morse potential. Thus the corrected curve, as temperature increases, performs transition from the blue (QM Harmonic curve with the smaller values of energy at the same temperature compare to the red QM Morse curve) to the red curve (larger energy values). Thus, the derivative (heat capacity) of the corrected curve should be slightly bigger than the derivative from the blue (QM Morse) curve in some range of temperatures (between 1000K and 5000K in Fig.4.6).

The heat capacity can be obtained by the differentiation (4.39) of the energy curves. Figure 4.6 shows how the heat capacities found by the differentiation of the energy curves on Fig.4.5 depend on temperature. Since in the harmonic potential, the average values of the kinetic and potential energies are the same and due to (4.37) the classical heat capacity for the particle in the harmonic potential is just  $k_b$  or unity in units used on Fig.4.6. The behavior of the QM solution for the harmonic potential is also well known [63]. Thus, we can see that our correction method again leads to a very good agreement between the approximate (corrected) and the exact (QM Morse) results.

Note that there is a small difference between the corrected curve (black dots) and the curve that represents the exact solution for the Morse potential in the range of temperature between 1000 K and 5000 K. This difference was already discussed above.

In QM approach the dependence of the heat capacity on temperature can be found not only by the differentiation of the energy curves but also directly from the knowledge of the energy levels. Differentiation of (4.35) with respect to temperature leads to:

$$\langle C_{QM}(T) \rangle = \frac{1}{T} [\langle E_{QM}^2(T) \rangle - \langle E_{QM}(T) \rangle^2], \quad (4.41)$$



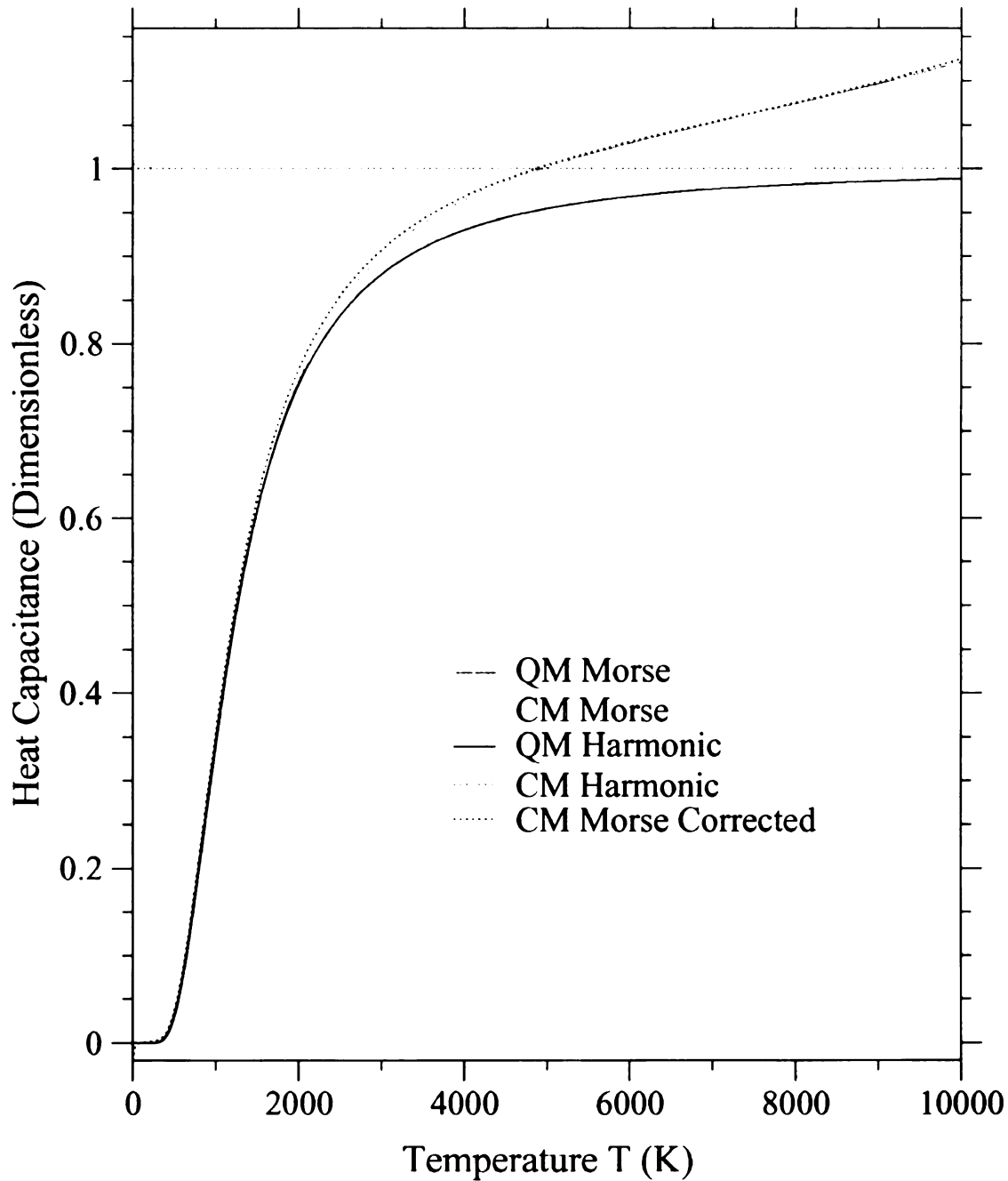


Figure 4.6: The dependencies of the heat capacities for the particle in the Morse potential and its harmonic approximation on temperature. The red and orange curves represent QM and CM solutions for the Morse potential. The blue and green (dashed) curves show the QM and CM solutions for the harmonic approximation to the Morse potential. The black dashed curve shows the CM solution for the Morse potential with the correction (4.31) that comes from the harmonic approximation to the Morse potential. All these curves were obtained by the differentiation (4.39) of the corresponding energy curves on Fig.4.5.

where  $\langle E_{QM}(T) \rangle$  is given by (4.35) and  $\langle E_{QM}(T) \rangle^2$  is:

$$\langle E_{QM}^2(T) \rangle = \frac{1}{Z_{QM}} \sum_{n=0}^{n_{max}} E_n^2 \exp\left[-\frac{E_n}{k_b T}\right]. \quad (4.42)$$

These summations can be performed for the Morse and Harmonic potentials. Moreover, in case of Harmonic potential, when energy levels are given by (4.7):  $E_n = \hbar\omega[n + 1/2]$ , the summation (4.35) can be made in a closed form leading to a well known result:

$$\langle E_{HQM}(T) \rangle = \hbar\omega\left(\langle n(T) \rangle + \frac{1}{2}\right), \quad (4.43)$$

where, as before:

$$\langle n(T) \rangle = \frac{1}{\exp\left[\frac{\hbar\omega}{k_b T}\right] - 1} \quad (4.44)$$

is the Bose-Einstein function. Expression (4.44) was previously used in (4.8). Differentiation of (4.43) with respect to temperature leads to:

$$C_{HQM}(T) = \frac{d\langle E_{HQM}(T) \rangle}{dT} = k_b\left(\frac{\hbar\omega}{k_b T}\right) \exp\left[-\frac{\hbar\omega}{k_b T}\right] \langle n(T) \rangle^2. \quad (4.45)$$

In the classical approach for the harmonic potential, since the value of the total energy is given by  $k_b T$ , the classical harmonic heat capacity is just  $k_b$ . Thus, the value of the correction term  $[C_{HQM}(T) - C_{HCM}]$  can be easily found.

In the classical approach for the general potential we have to differentiate expression (4.36) (using expressions 4.37 and 4.38). Thus, we get:

$$\langle C_{CM}(T) \rangle = \frac{1}{2}k_b + \frac{1}{T}(\langle U_{CM}^2(T) \rangle - \langle U_{CM}(T) \rangle^2), \quad (4.46)$$

where  $\langle U_{CM}(T) \rangle$  is given by (4.38) and  $\langle U_{QM}(T) \rangle^2$  is:

$$\langle U(T) \rangle = \frac{1}{Z_{CM}} \int U^2(x) \exp\left[-\frac{U(x)}{k_b T}\right] dx. \quad (4.47)$$

Last formulas can be employed for the Morse potential. Thus we write:

$$C_{MQM} = C_{MCM} + [C_{HQM}(T) - C_{HCM}] \quad (4.48)$$

Both approaches: numerical differentiation of the energy curves and calculation of the heat capacity using formulas above should lead to the same result, as they do: the differences between the curve obtained by the numerical differentiation of the corrected energy curves and the curve obtained using the formulas above would be invisible on the scale of Fig.4.6.

In case when there are several independent (orthogonal) vibrational modes the correction should be applied to each mode independently. This can be used to correct the heat capacity for the manyatomic molecules that have several vibrational modes.

## 4.4 Vibrations of large molecules

Let us assume initially that atoms in the molecule vibrate near their equilibrium positions with amplitudes of vibrations that are much smaller than any interatomic distances. Thus for the moment we ignore the possibility of the large-scale atomic motion that can be caused by the flexibility of the molecule. In order to calculate the PDF it is necessary to calculate the mean square deviations of the distances between the atoms from their equilibrium values:  $\sigma_{ij}^2$ . Let the coordinates of atoms  $i$  and  $j$  be  $\vec{r}_i = \vec{r}_i^0 + \vec{u}_i$  and  $\vec{r}_j = \vec{r}_j^0 + \vec{u}_j$ , where  $\vec{r}_i^0$  and  $\vec{r}_j^0$  are the equilibrium coordinates of atoms  $i$  and  $j$ , while their instantaneous displacements are  $\vec{u}_i$  and  $\vec{u}_j$ . Let also:  $\vec{r}_{ij} = \vec{r}_j - \vec{r}_i$ ,  $\vec{r}_{ij}^0 = \vec{r}_j^0 - \vec{r}_i^0$  and  $\vec{u}_{ij} = \vec{u}_j - \vec{u}_i$ . Then it is easy to show, under the

assumption  $u_{ij} \ll r_{ij}^o$ , that:

$$\begin{aligned}\sigma_{ij}^2 &= \langle (r_{ij} - r_{ij}^o)^2 \rangle \cong \langle [\hat{r}_{ij}^o \vec{u}_{ij}]^2 \rangle \\ &= \sum_{\alpha, \beta} \hat{r}_{ij}^{\alpha\alpha} \hat{r}_{ij}^{\beta\beta} \langle (u_{i\alpha} u_{i\beta} - u_{i\alpha} u_{j\beta} - u_{j\alpha} u_{i\beta} + u_{j\alpha} u_{j\beta}) \rangle\end{aligned}\quad (4.49)$$

where  $\hat{r}_{ij}^o = \vec{r}_{ij}^o / r_{ij}^o$ . The indexes  $\alpha, \beta$  stand for the Cartesian coordinates of the vectors.

We consider here the vibrations of a molecule that consists of  $N$  atoms with masses  $m_i$ . The potential energy of the molecule  $U(\vec{r})$  is a function of the coordinates  $\vec{r}$  of all the atoms. There are  $3N$  components  $x_i$  of the vector  $\vec{r}$ . Thus the index  $i$  runs over all the atoms and over all their Cartesian coordinates.

Let us assume that the atoms vibrate near their equilibrium positions  $\vec{r}_o$  and that their instantaneous coordinates are  $\vec{r} = \vec{r}_o + \vec{u}$ . If vector  $\vec{u}$  is small enough the potential energy could be expanded near the equilibrium ( $\vec{r}_o$ ):

$$U(x) \cong U_o + \frac{1}{2} \sum_{ij} D_{ij} u_i u_j, \quad (4.50)$$

where

$$D_{ij} = \frac{\partial^2 U(\vec{r}_o)}{\partial x_i \partial x_j} \quad (4.51)$$

is a real symmetric matrix. Thus for the Hamiltonian we have:

$$H = \sum_i \frac{p_i^2}{2m_i} + \frac{1}{2} \sum_{ij} D_{ij} u_i u_j. \quad (4.52)$$

It is convenient to introduce new variables

$$p_i = \sqrt{m_i} \pi_i, \quad u_i = q_i / \sqrt{m_i} \quad (4.53)$$

that will transform (4.52) into:

$$H = \sum_i \frac{\pi_i^2}{2} + \frac{1}{2} \sum_{ij} \tilde{D}_{ij} q_i q_j, \quad (4.54)$$

where  $\tilde{D}_{ij} = D_{ij} / \sqrt{m_i m_j}$ .

Since  $\tilde{D}_{ij}$  is a real and symmetric matrix it could be brought to the diagonal form by the linear transformations of  $q_i$  :

$$q_i = \sum_{\lambda} e_i^{\lambda} Q_{\lambda}, \quad (4.55)$$

where  $\tilde{e}^{\lambda}$  could be chosen as real, orthogonal and normalized:

$$\sum_i e_i^{\lambda} e_i^{\lambda'} = \delta_{\lambda\lambda'}. \quad (4.56)$$

In this case the transformation:

$$\pi_i = \sum_{\lambda} e_i^{\lambda} P_{\lambda} \quad (4.57)$$

will also bring to the diagonal form the first sum in (4.54). Thus we can rewrite Hamiltonian as:

$$H = \sum_{\lambda} \frac{1}{2} [P_{\lambda}^2 + \omega_{\lambda}^2 Q_{\lambda}^2]. \quad (4.58)$$

The second quantization:

$$Q_{\lambda} = \frac{1}{2} \sqrt{\frac{\hbar}{\omega_{\lambda}}} (a_{\lambda}^{\dagger} + a_{\lambda}), \quad P_{\lambda} = \frac{i}{2} \sqrt{\hbar \omega_{\lambda}} (a_{\lambda}^{\dagger} - a_{\lambda}), \quad (4.59)$$

with  $[P, Q] = i\hbar$  so that  $a_\lambda^+ a_{\lambda'} - a_{\lambda'} a_\lambda^+ = \delta_{\lambda\lambda'}$  transforms (4.58) into:

$$H = \sum_{\lambda} \hbar \omega_{\lambda} (a_{\lambda}^+ a_{\lambda} + \frac{1}{2}), \quad (4.60)$$

as it should. Thus  $\langle \psi | H | \psi \rangle = \sum_{\lambda} \hbar \omega_{\lambda} (n_{\lambda} + 1/2)$ .

From (4.53, 4.55, 4.59) follows that:

$$u_i = \sum_{\lambda} e_i^{\lambda} \sqrt{\frac{\hbar}{2m_i \omega_{\lambda}}} (a_{\lambda}^+ + a_{\lambda}). \quad (4.61)$$

Thus, separating the atomic and Cartesian coordinates, we get:

$$\langle \psi | u_{i\alpha} u_{j\beta} | \psi \rangle = \sum_{\lambda} \frac{\hbar}{2\omega_{\lambda}} (n_{\lambda} + \frac{1}{2}) \frac{e_{i\alpha}^{\lambda}}{\sqrt{m_i}} \frac{e_{j\beta}^{\lambda}}{\sqrt{m_j}}. \quad (4.62)$$

It is easy to show, using (4.62), that (4.50) transforms into:

$$\sigma_{ij}^2 = \sum_{\lambda} \frac{\hbar}{2\omega_{\lambda}} [n_{\lambda} + \frac{1}{2}] \left\{ \frac{(\vec{e}_i^{\lambda} \hat{r}_{ij}^o)}{\sqrt{m_i}} - \frac{(\vec{e}_j^{\lambda} \hat{r}_{ij}^o)}{\sqrt{m_j}} \right\}^2, \quad (4.63)$$

where  $n_{\lambda}$  is the Bose-Einstein function (4.10) that at high temperatures can be substituted by (4.11). It is easy to see that (4.63) in case of the diatomic molecules ( $m_1 = m_2 = m$ ) reduces to (4.9), if to take into account that  $\mu = m/2$  and  $(\vec{e}_i \hat{r}_{ij}) - (\vec{e}_j \hat{r}_{ij}) = 2$ .

MD or MC simulations at low temperatures, when the anharmonicity of the real potential can be ignored, would lead to (4.63, 4.11), while the correct result is (4.63, 4.10). It is clear from (4.7, 4.9, 4.10, 4.11, 4.12) and from (4.60, 4.63) that the formulas (4.31, 4.40) used to correct the CM results in case of the diatomic molecule can be modified in an obvious way in order to correct the CM results that were obtained on

a many-atomic molecule, i.e.:

$$E(T) = E_{CM}(T) + \sum_{\lambda} [E_{HQM}(\lambda, T) - E_{HCM}(\lambda, T)]. \quad (4.64)$$

The width of the peaks can be corrected via

$$\sigma^2(T) = \sigma_{CM}^2(T) + \sigma_{corr}^2(T), \quad (4.65)$$

where

$$\sigma_{corr}^2(T) = \sum_{\lambda} [\sigma_{HQM}^2(\lambda, T) - \sigma_{HCM}^2(\lambda, T)] \quad (4.66)$$

and the index  $\lambda$  runs over different vibrational modes.

From the result of MD or MC calculation only the total (not for the particular vibrational mode) average values of the  $E_{CM}(T)$  and  $\sigma_{CM}^2(T)$  could be found.

## 4.5 TINKER package for molecular modelling and the $C_6H_{14}$ molecule

In order to demonstrate the role of the quantum corrections (4.64, 4.65) for a more complicated molecule, it is necessary to find the eigenfrequencies and eigenvectors of molecular vibrations as well as the results of the classical MD or MC simulations. There are many different potentials and programs developed for the different kinds of molecules. One of the most developed potentials are those developed for hydrocarbons. One of them is the so called “MM3” potential [65, 66, 67, 68, 69, 70, 71, 72]. One of the programs (a package that includes several different programs) that can use this potential to optimize the molecular structure, calculate the eigenfrequencies

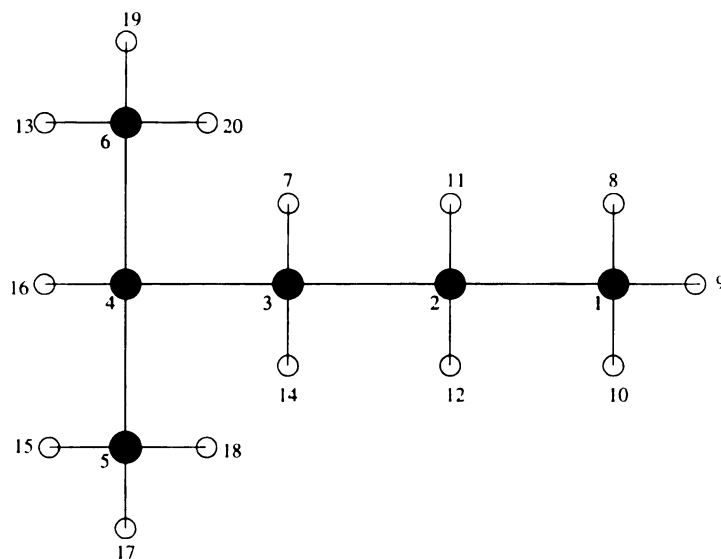


Figure 4.7: The sketch of the  $C_6H_{14}$  molecule. The carbon atoms are shown as black filled circles. The hydrogen atoms are shown as open circles. The numeration of the atoms coincides with those used in the Fig.4.9 and Fig.4.10,4.11,4.12

( $\omega_\lambda$ ) and eigenvectors ( $\vec{e}^\lambda$ ) in a particular equilibrium configuration and to run MD at given temperature is “TINKER” [73, 74, 75, 76, 77, 78, 79]. As an output of MD simulations (for a single molecule) at given temperature, TINKER provides the coordinates of the atoms, the total energy, the kinetic and potential energies as functions of time.

We use the  $C_6H_{14}$  - molecule as a test example. Figure 4.7 shows the sketch of the  $C_6H_{14}$  molecule, while the Fig.4.8 shows the geometry of the  $C_6H_{14}$  molecule in *Long* conformation. At room temperature the  $C_6H_{14}$  molecule is relatively flexible, as we will see. At normal pressure these molecules form a non-toxic and not very flammable liquid and thus its PDF can be easily measured.

At low temperatures the  $C_6H_{14}$  molecule can be in two different conformations, as follows from MD simulations and structures optimizations with TINKER, which we call *Long* and *Short*. The distances between some atoms in these molecular conformations are shown in the table 4.1. The ground state tension energies (obtained from



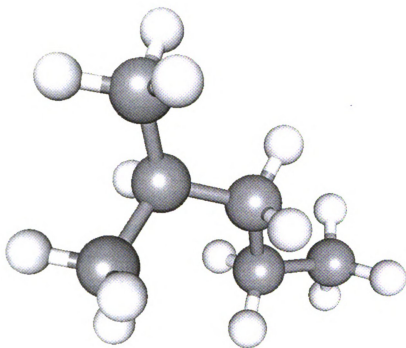


Figure 4.8: The geometry of the  $C_6H_{14}$  molecule in *Long* conformation.

Pair of Atoms $i - j$	1 - 4	1 - 5	1 - 6
Distance between $i$ and $j$ (Long), (Å)	3.94	4.56	5.07
Distance between $i$ and $j$ (Short), (Å)	3.17	4.54	3.81

Table 4.1: The distances between some atoms in *Long* and *Short* conformations.

TINKER) of the molecule in *Long* and *Short* conformations are slightly different:

$$E_L = 6.3479 \text{ (kcal/mol)}, \quad (4.67)$$

$$E_S = 7.1293 \text{ (kcal/mol)},$$

where  $L$  stands for the *Long* and  $S$  for the *Short*. The difference in the energies between these two conformations per molecule in temperature units is:

$$\Delta E = E_S - E_L \approx 393 \text{ (K)}. \quad (4.68)$$

## 4.6 Calculation of PDF for $C_6H_{14}$ molecule

### 4.6.1 Low temperatures

The blue curves on Fig.4.9 show the probabilities for finding the pairs of atoms 1-2, 1-3, 1-4, 1-5, 1-6 at a given distance obtained from MD simulations at temperatures 150 K and 500 K. In the beginning of MD runs, the molecule was always in an equilibrium *Long* conformation. At temperature 150 K the molecule remains in *Long* conformations during the MD run. At temperature 500K the molecule continuously switches between different conformations (it is flexible). The time step in MD simulations was  $\Delta t = 1$  femtoseconds. The coordinates of the atoms were saved after every 1000 MD time steps. The blue curves represent the distributions obtained from 10,000 different molecular configurations. Thus the total run time was 10,000 picoseconds. The red curves were obtained by the convolution (4.33,4.34) of the blue curves with the Gaussian whose correction width  $\sigma_{corr}$  that corresponds to the given pair of atoms for the molecule is in *Long* conformation.

At low temperature, when the molecule is frozen in the *Long* or *Short* configuration, atoms only vibrate slightly near their equilibrium positions. As the temperature increases, there can occur transitions between *Long* and *Short* configurations. This behavior could be seen from the change in the peak shape for the pairs of atoms 1-4, 1-5, 1-6 when temperature changed from 150 K to 500 K. At 150 K those peaks are relatively narrow and symmetric, while at 500 K the peaks become much broader and their shape indicates that there are two conformations in which the molecule spends most of its time.

If the molecule during the MD run remains all the time in *Long* or *Short* conformation it is clear what set of the correction  $\sigma_{corr}$  should be used. If the molecule changes its conformation during the MD run, it becomes unclear what  $\sigma_{corr}$  set should be used: from *Long* or from *Short* conformation. We will discuss this issue later.

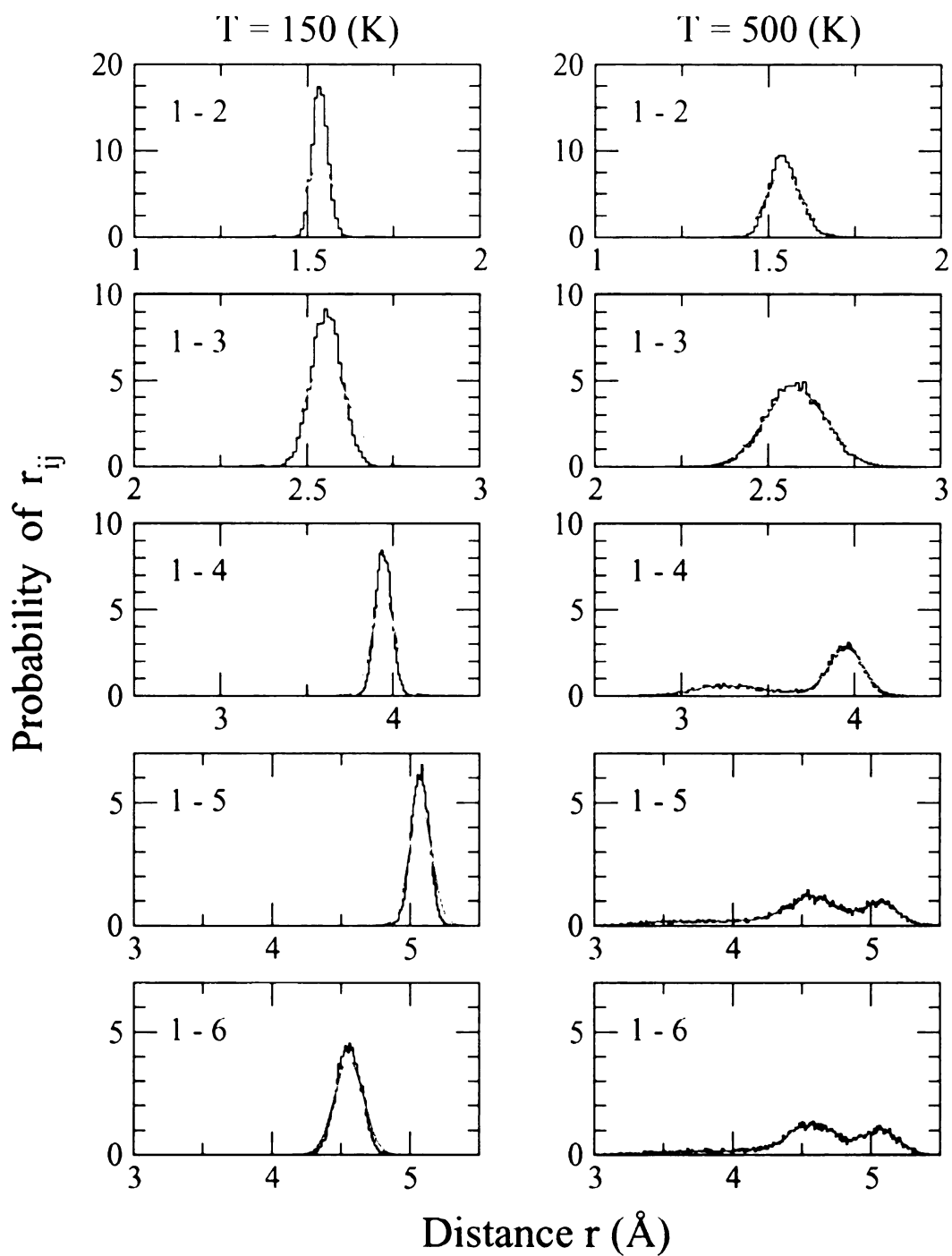


Figure 4.9: The probability for finding a particular pair of atoms at a given distance at temperatures 150K on the left and at 500K on the right. The blue curves were obtained from the classical MD trajectories. The red curves result from the convolution of the blue curves with the corresponding correction Gaussian. Every pair of atoms has its own  $\sigma_{corr}^2(T)$ .

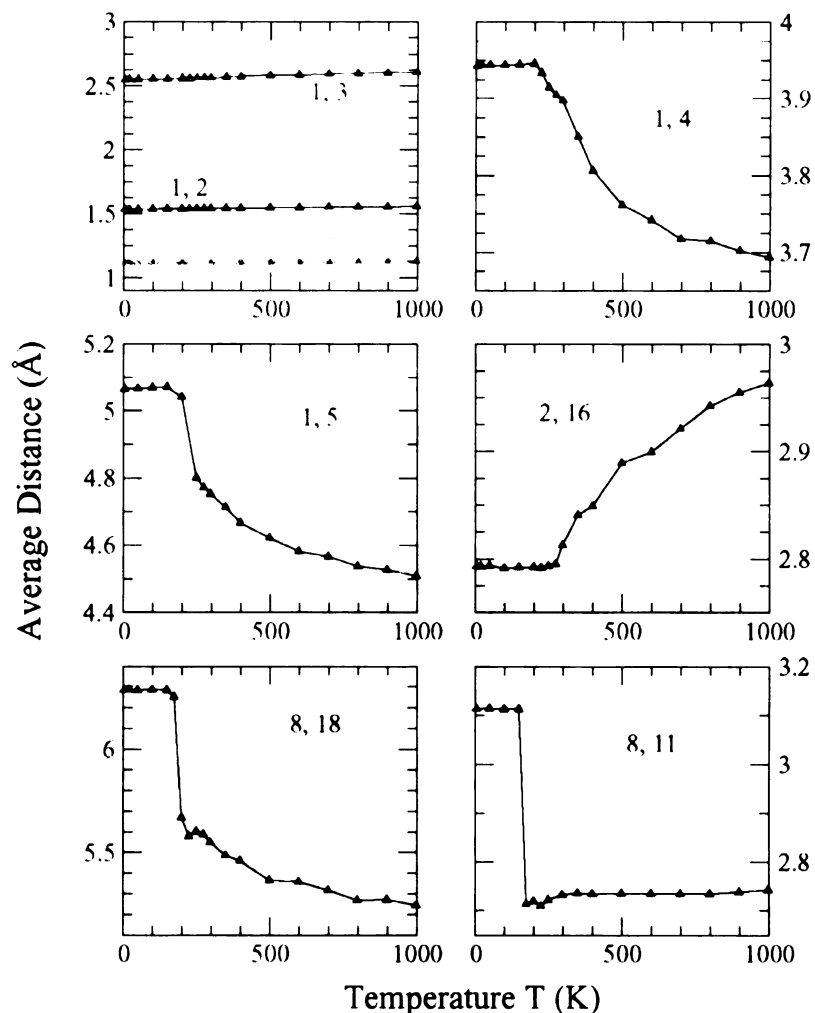


Figure 4.10: The dependencies of the average distances between some pairs of atoms on temperature obtained from MD simulations. In the beginning of every MD run (at a particular temperature) the molecule was always in equilibrium *Long* conformation. At low temperatures these distances only slightly depend on temperature, as molecule remains in the *Long* conformation. As temperature increases instantaneous distance between a pair of atoms can have significantly different values that occur when the molecule can be in different conformations (or identical atoms interchange their positions). Thus, as temperature increases, there occur sharp changes in the average distances for some pairs of atoms.

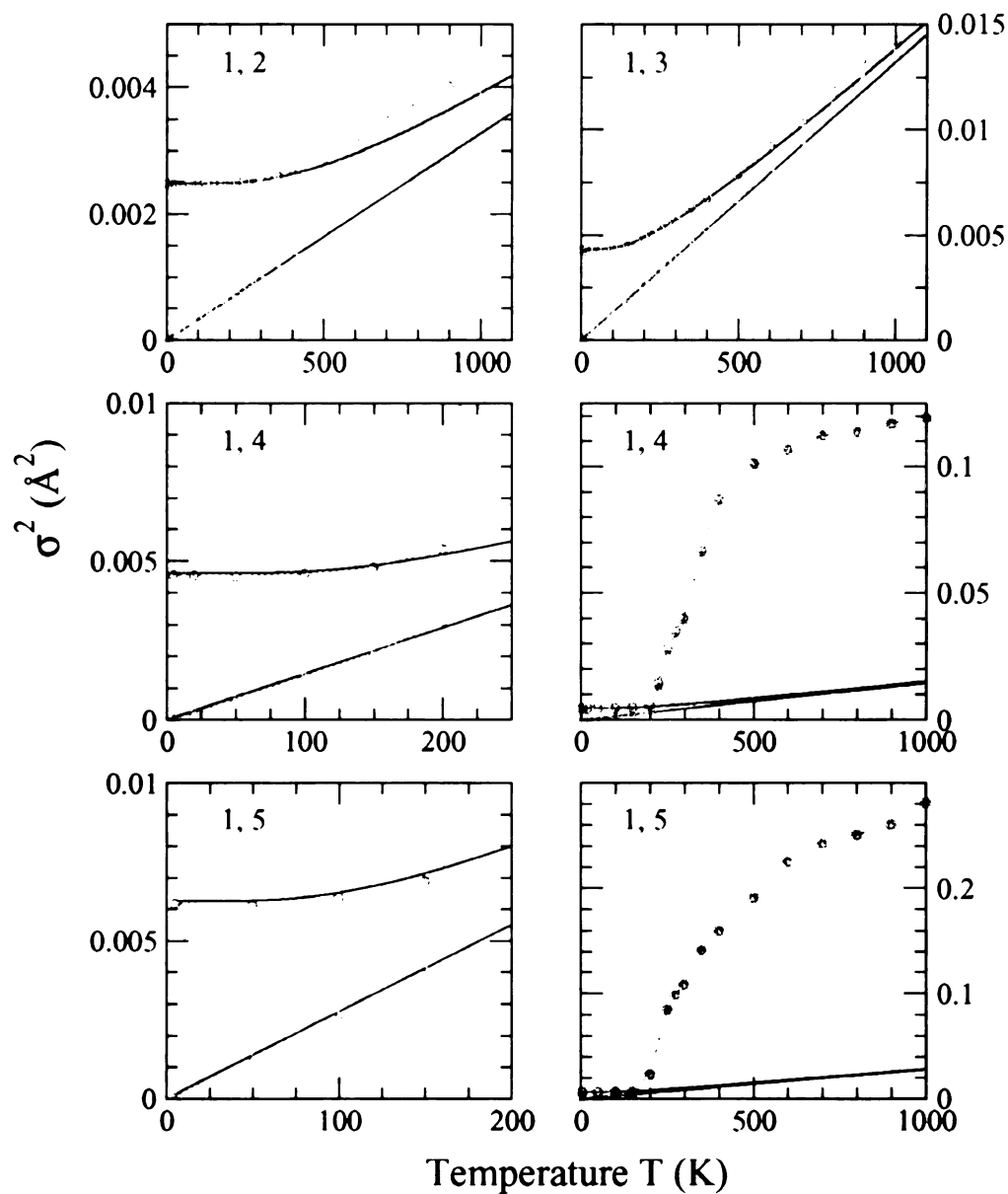


Figure 4.11: The dependencies of  $\sigma^2$  on temperature  $T$  for some pairs of atoms. The orange triangles show the results obtained from MD simulations, the blue and green curves show the QM and CM results obtained from the eigenfrequencies and eigenvectors of molecular vibrations. The red circles show the MD results corrected by adding to the orange triangles the difference between the blue and green curves.

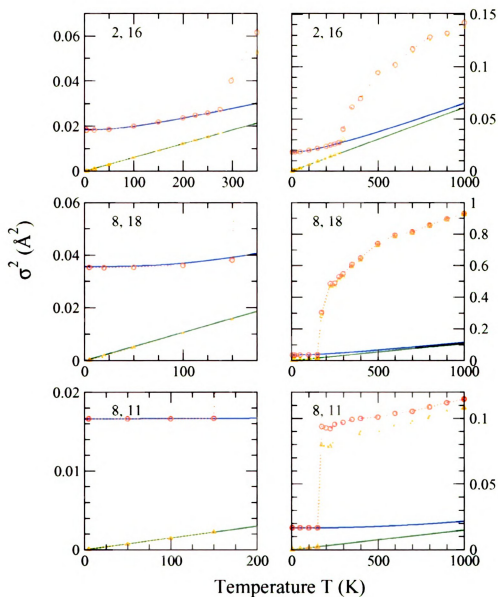


Figure 4.12: The dependencies of  $\sigma^2$  on temperature  $T$  for some pairs of atoms. The orange triangles show the results obtained from MD simulations, the blue and green curves show the results obtained from the QM and CM results obtained from the eigenfrequencies and eigenvectors of molecular vibrations. The red circles show the MD results corrected by adding to the orange triangles the difference between the blue and green curves.

The orange triangles on the Fig.4.11,4.12 show how the  $\sigma_{CM}^2$  obtained in MD runs depend on temperature (See also Fig.4.10). The blue and green curves show  $\sigma^2(T)$  that were obtained in the harmonic approximation from the eigenfrequencies and eigenvectors of molecular vibrations in the frame of QM (4.63,4.11) and CM (4.63,4.10) respectively. The red circles were obtained by applying the correction (4.65) to the MD results. Thus at very low temperatures the results of MD simulations agree with the CM results obtained in the harmonic approximation, as it should be. However the correct results at these temperatures are given by the QM results on the harmonic potential (the blue curve). Thus our correction, if applied, shifts the orange triangles into the red circles that fit QM results at low temperatures very well. As temperature increases the anharmonicity of the potential usually makes potential softer, thus increasing  $\sigma^2(T)$  compared with the harmonic case. The sharp increase in the  $\sigma^2(T)$  with increase of temperature that occurs for some pairs of atoms corresponds to the appearance of flexibility. Thus the molecule becomes flexible between 200 and 300 K. It is easy to see, from the numbers of the atoms, that it is the dihedral angles that become flexible.

If the molecular trajectory is known the PDF (4.3) could be found if the distributions of lengths (the blue curves on Fig.4.9) for every pair of atoms will be used instead of the Gaussians in (4.3). The correction could be made by the convolution of the distribution of distances for every pair of atoms with the gaussians (4.33,4.34). The brown curves on the Fig.4.13 show the PDFs obtained in MD simulations when the molecule remains in *Long* conformation before the correction, while the blue curves show the corrected PDFs. Thus at low temperatures the correction significantly changes the shape of the PDF. The role of the correction remains important at small distances at all temperatures, while at large distances its role decreases as temperature increases because the widths of peaks that correspond to the atoms that are well separated become significantly larger in MD simulations.

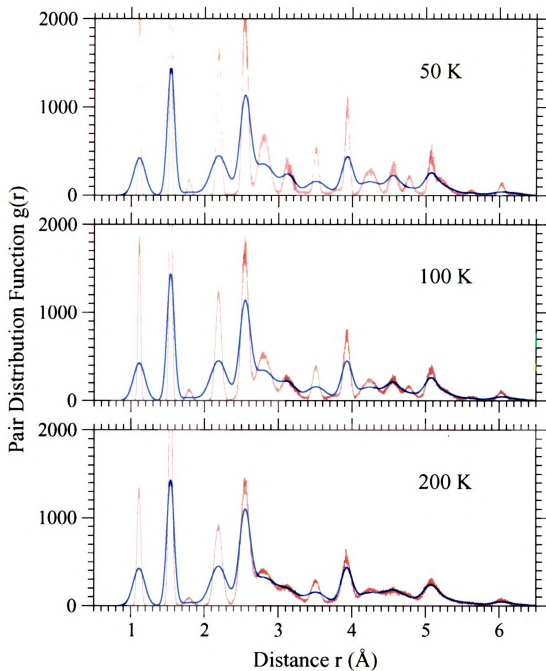


Figure 4.13: PDF for the  $C_6H_{14}$  molecule in *Long* conformation at low temperatures. The brown curves show the results of MD simulations before the correction is applied. The blue curves show the results of MD simulations corrected by convolution (4.33, 4.34).



It is not known in general how many molecules are in a particular conformation. The relative contributions of different conformations to the total PDF depend on the shape of the free energy surface. Since the line shape of the free energy is not known the simplest way to combine the results obtained on different conformations is to assign the Boltzman weights to the PDFs in different conformations. Thus the weight for the molecule in *Long* conformation:

$$w_L(T) \propto \exp \left[ -\frac{E_L}{k_b T} \right], \quad (4.69)$$

Thus for the  $C_6H_{14}$  molecule at low temperatures the total PDF can be calculated as a linear combination of the PDFs from *Long* and *Short* conformations with the corresponding Boltzman weights.

$$G(r, T) = w_L(T)G_L(r, T) + w_S(T)G_S(r, T), \quad (4.70)$$

where  $G_L(r, T)$  and  $G_S(r, T)$  are the corrected PDFs from *Long* and *Short* conformations. The Boltzman weights  $w_L(T)$  and  $w_S(T)$  are given by:

$$w_L(T) = \frac{1}{1 + \exp \left[ -\frac{\Delta E}{k_b T} \right]} \quad (4.71)$$

and

$$w_S(T) = \frac{\exp \left[ -\frac{\Delta E}{k_b T} \right]}{1 + \exp \left[ -\frac{\Delta E}{k_b T} \right]}. \quad (4.72)$$

so that:  $w_L(T) + w_S(T) = 1$ . Table 4.2 shows  $w_L(T)$  and  $w_S(T)$  for temperatures 50, 100, 150, 200 (K).

The corrected PDFs for the  $C_6H_{14}$  molecule in *Long* and *Short* conformations at different temperatures are shown in Fig.4.14 as the blue and green curves respec-

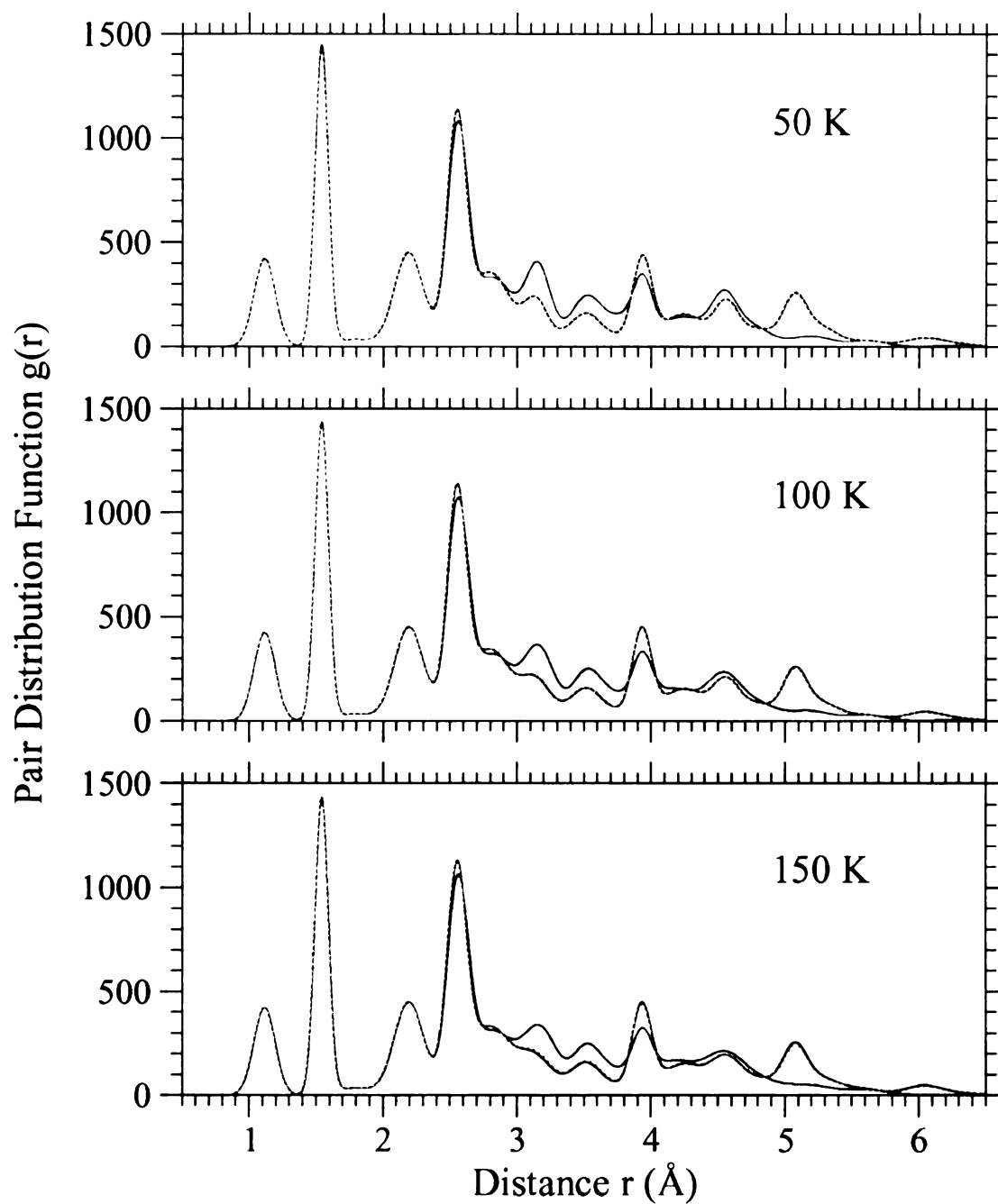


Figure 4.14: The blue and green solid curves show total corrected PDFs for the molecule in *Long* and *Short* conformations. The red dashed curve shows Boltzman combination (4.70) of PDFs from *Long* and *Short* conformations. At all temperatures when the molecules remains in one or another conformation the combined PDF basically coincides with PDF in *Long* conformation due to the values of the Boltzman weights.

Temperature T (K)	50	100	150	200
$w_L(T)$	0.9996	0.98	0.93	0.88
$w_S(T)$	0.0004	0.02	0.07	0.12

Table 4.2: Boltzman weights for  $C_6H_{14}$  molecule in *Long* and *Short* conformations at different temperatures.

tively. The red curves in Fig.4.14 show PDFs calculated according to (4.70) with the Boltzman weights taken from the table 4.2.

### 4.6.2 High temperatures

In order to use the Boltzman combination of the PDFs in different conformations to obtain the total combined PDF, the molecule should remain in one or the other conformation during the MD run, or it is necessary to separate those times (parts of the molecular trajectory) when the molecule is in one or in the other conformation. It is necessary to do this because every conformation has its own set of  $\sigma_{corr}$  that was obtained using the eigenfrequencies and eigenvectors of the molecular vibrations in the corresponding conformation.

In practice, however, it is impossible to say when the molecule is in one or in the other conformation. For example even when the molecule remains in *Long* or *Short* conformation the positions of atoms 8 and 9 can interchange during the MD run. When it happens the molecule is already in a different conformation since atoms 8 and 9 have different sets of  $\sigma_{corr}$  with respect to the other atoms. Thus although the geometry of the molecule did not change during the interchange of positions of atoms 8 and 9, the sets of  $\sigma_{corr}$  should be modified. It seems to be an impossible task to track all such little changes. Another reason that does not allow separation of different conformations at high temperatures comes from the observation that the changes in the distances between some pairs of atoms, due to the vibrations, become comparable with the changes in the distances caused by the changes in the

conformations. Thus basically it becomes impossible to say when the molecule is in one or in the other conformation. Thus, at high temperatures, the approach that combines PDFs in different conformations with the corresponding Boltzman weights becomes unacceptable.

Instead another approach could be used. In order to obtain the corrected PDF in *Long* conformation it is necessary to convolute the PDF obtained from the MD trajectory in *Long* conformation with the set of  $\sigma_{corr}$  that was also obtained on the *Long* conformation. Assume that instead of convolution performed with the set of  $\sigma_{corr}$  from the *Long* conformation we will use the set of  $\sigma_{corr}$  from the *Short* conformation. How different would the corrected PDFs be when obtained with these two different sets of  $\sigma_{corr}$  from the same MD trajectory?

The brown curves on Fig.4.15 show PDFs obtained from the MD trajectory at temperature 50 K when the molecule remains in the *Long* (top) or in the *Short* (bottom) conformation depending on initial configuration. The blue solid curve originates from the convolutions of the MD results from the *Long/Short* conformations with the correct sets of  $\sigma_{corr}$  from the *Long/Short* conformations. The red dashed curves were obtained by the convolution of the brown curves with the incorrect sets of  $\sigma_{corr}$ : the MD results from the *Long/Short* conformations were convoluted with the  $\sigma_{corr}$  from the *Short/Long* conformations.

Thus, although there are very significant differences between the non-convoluted and convoluted (corrected) PDFs the differences between the PDFs obtained by the convolutions with different sets of  $\sigma_{corr}$  are rather small.

The small differences between the MD results corrected with the different sets of  $\sigma_{corr}$  could be easily understood. Our correction is the most significant (large  $\sigma_{corr}$ ) for those pairs of atoms that are tightly connected, i.e. by a bond or by an angle. Thus the correction is significant for those atoms that are close to each other. The mutual vibrations of such pairs (distance distribution) are slightly affected by the general

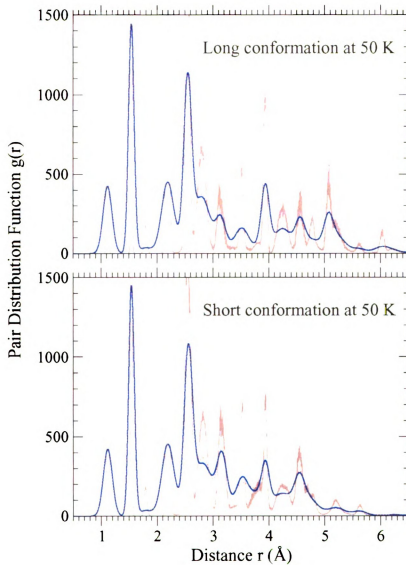


Figure 4.15: The brown curves on both figures show MD results obtained on the *Long* (top) and *Short* (bottom) conformations. The figure on top also shows the corrected PDFs obtained by the correction of MD results from the *Long* conformation with the set of  $\sigma_{corr}$  from the *Long* (the blue solid curve) and *Short* (the red dashed curve) conformations. The bottom figure also shows the PDFs obtained by the correction of MD results from the *Short* conformation with the sets of  $\sigma_{corr}$  from *Short* (blue solid curve) and *Long* (red dashed curve) conformations.

conformation of the molecule-they are almost the same for all of them. On the other hand, if atoms in a pair are far away from each other then the corresponding  $\sigma_{corr}$  are small in general, independently from the molecular configuration. Thus the correction is not that important for those pairs in principle. That means that in order to apply the correction we can convolute the PDF obtained from the MD simulations with a set of  $\sigma_{corr}$  from any particular configuration. At higher temperatures the differences between the curves obtained by convolutions with different sets of  $\sigma_{corr}(T)$  will become even smaller since  $\sigma_{corr}(T)$  decrease with increase of temperature (see Fig.4.4,??).

Figure 4.16 show PDFs calculated for the  $C_6H_{14}$  molecule at different temperatures. The PDFs at temperatures 50 (K) and 150 (K) were obtained by combining the PDFs from the *Long* and *Short* conformations with the corresponding Boltzman weights. The PDF curves at temperatures 298(K), 500(K) and 800(K) were obtained by the convolution of PDFs from the MD simulations with the Gaussians with the correction widths from the *Long* conformations. It follows from the figure that the PDFs in the region of  $r < 3$  (Å) only slightly change in the considered interval of temperatures. The inset that shows the region of  $3 < r < 6.5$ (Å) on a bigger scale shows how the flexibility of the molecule develops as temperature increases.

The region  $3 < r < 6.5$  (Å) is the most interesting if the large scale molecular motion is under consideration. In this region our correction is not very significant for a single molecule. However, in order to compare the results of calculations with the experimental results, it is necessary to calculate the combined PDF from many different molecules. The PDF from the different molecules can overlap in the region  $r < 3$  (Å). Thus, in order to extract accurate information about the mutual orientation of different molecules. (that in addition can put some constraints on a single molecular motion), it will be necessary to accurately calculate the PDF at small distances, i.e. in the region where our correction is significant.

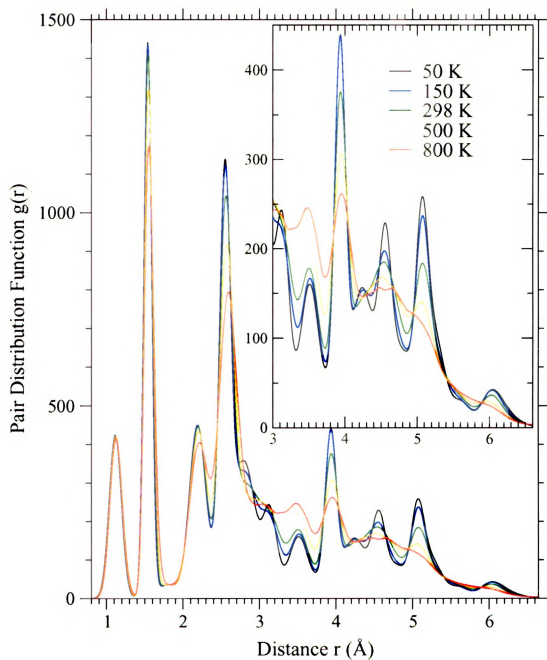


Figure 4.16: Corrected PDFs for the  $C_6H_{14}$  molecule at different temperatures. The inset shows the region between 3  $\text{\AA}$  and 6.5  $\text{\AA}$  on a bigger scale.

### 4.6.3 Pair Distribution Function from Molecular Vibrations and Partial PDFs.

In order to understand how PDF of the molecule depends on the molecule's conformation, it is useful to consider partial PDFs with respect to the carbon atom number 1. It is also informative to calculate partial PDFs from eigenfrequencies and eigenvectors of molecular vibrations in *Long* and *Short* conformations and compare those PDFs between each other and with partial PDFs obtained using results of MD simulations with our correction method. Figures 4.17, 4.18, 4.19, 4.20 and 4.21 show few of such PDFs.



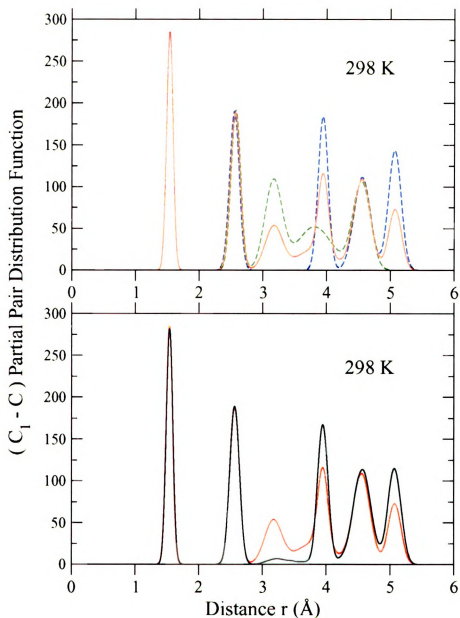


Figure 4.17: The panel on top shows PDFs with respect to carbon atom number 1 created by the other carbon atoms only at 298K. Blue and green curves were obtained from molecule in *Long* and *Short* conformations correspondingly. The widths of peaks were calculated in QM approach using eigenfrequencies and eigenvectors of molecular vibrations. As distance increases there are peaks that correspond to the carbon atoms number 2, 3, 4, 5 and 6. The red curve is a linear combination of blue and green curves with corresponding Boltzman weights. The red curve in the bottom panel is the same as the red curve in the top panel. The grey curve, that also shows PDF with respect to the carbon atom number 1 due to the other carbon atoms, was obtained from MD simulations. The black curve was obtained from the grey curve using our correction scheme.

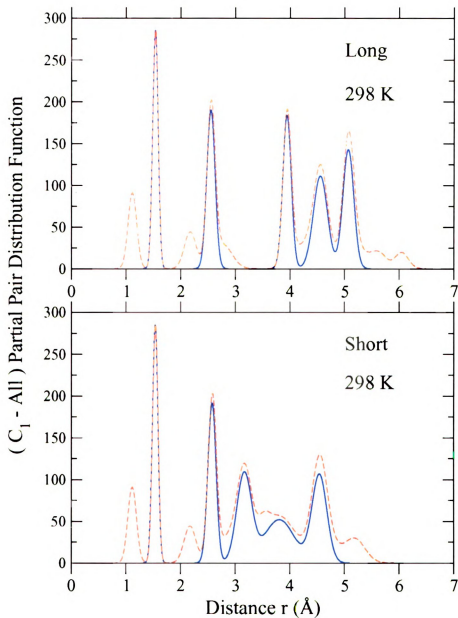


Figure 4.18: The top panel shows partial PDFs with respect to the carbon atom number 1 calculated for the molecule in *Long* conformation from eigenfrequencies and eigenvectors of molecular vibrations in the QM approach. The blue curve shows partial PDF due to the other carbon atoms only (hydrogen atoms are ignored). The red curve is due to all the other atoms (carbons and hydrogens). Thus, the difference between two curves is due to the hydrogen atoms. The bottom panel shows the same curves as the top panel, but for the molecule in *Short* conformation.

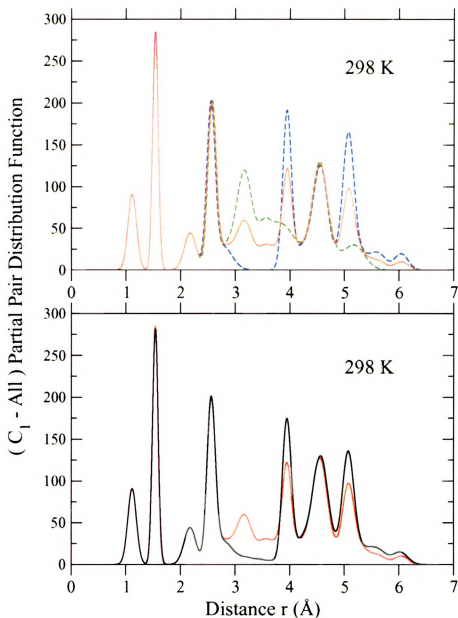


Figure 4.19: The top panel shows partial PDFs with respect to the carbon atom number 1 created by all other atoms (carbons and hydrogens). The blue and green curves were calculated from eigenfrequencies and eigenvectors of molecular vibrations in *Long* and *Short* conformations correspondingly. The red curve is the linear combination of the blue and green curves with corresponding Boltzman weights. The red curve in the bottom panel is the same as the red curve in the top panel. The grey curve was extracted from MD simulations in which transitions between conformations occur. The black curve was obtained from the grey curve using our correction method.

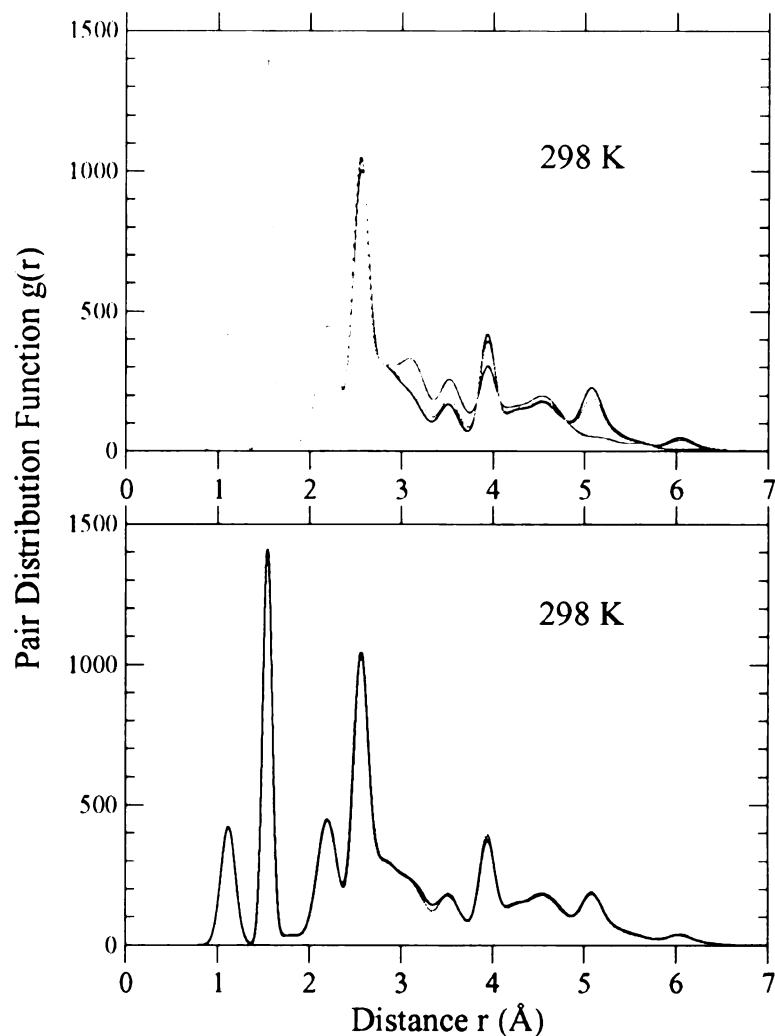


Figure 4.20: The blue and green curves in the top panel were calculated from eigenfrequencies and eigenvectors of molecular vibrations for the molecule in *Long* and *Short* conformations correspondingly. They show the total PDFs of the molecule. The red curve is a linear combination of the blue and green curves with corresponding Boltzmann weights ( $w_L(T) = 0.79$  and  $w_S(T) = 0.21$ ). The red curve in the bottom panel is the same as the red curve in the top panel. The grey curve, that also shows the total PDF of the molecule, was obtained from MD simulations. The black curve was obtained from the grey curve using our correction/convolution method.

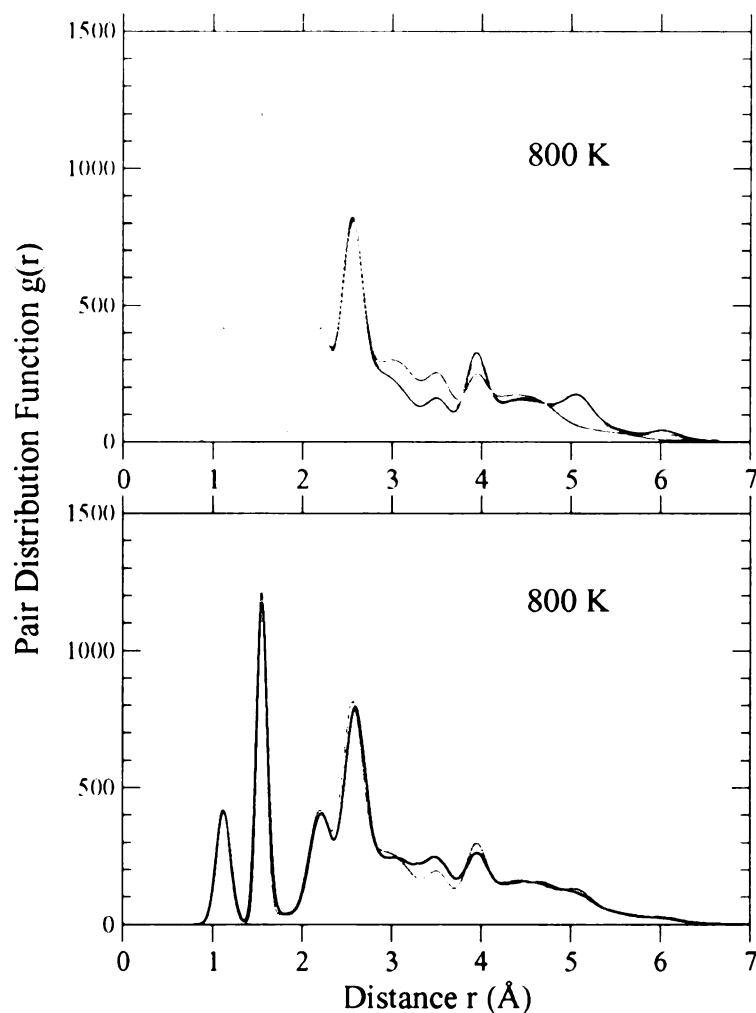


Figure 4.21: The blue and green curves in the top panel were calculated from eigenfrequencies and eigenvectors of molecular vibrations for the molecule in *Long* and *Short* conformations correspondingly. They show the total PDFs of the molecule. The red curve is a linear combination of the blue and green curves with corresponding Boltzmann weights ( $w_L(T) = 0.62$  and  $w_S(T) = 0.38$ ). The red curve in the bottom panel is the same as the red curve in the top panel. The grey curve, that also shows the total PDF of the molecule, was obtained from MD simulations. The black curve was obtained from the grey curve using our correction/convolution method.

#### 4.6.4 Correction to the Heat Capacity for $C_6H_{14}$ molecule

Figure 4.22 shows the dependencies of the total energy (top panel) and the heat capacity (bottom panel) of the  $C_6H_{14}$  molecule on temperature.

MD simulations were performed with the time step 1 femtosecond. The Tinker MD package provides as an output the values of energy averaged over 100 MD steps (0.1 picosecond). The total simulation time used to calculate the average energy values, was 1000 picoseconds for temperatures below 200 K. For temperatures above 200 K the total simulation time was 100,000 picoseconds. Thus, the average energy values were found by averaging over 10,000 ( $T < 200$  K) and 1,000,000 ( $T > 200$  K) different energy values, that are themselves the average values over 100 MD steps. The MD simulations were performed at temperatures between 10 K and 1010 K. Temperature increment was 10 K for temperatures below 200 K. Simulations also were performed at temperatures (190, 195, 200, 205, 210) K, (290, 295, 300, 305, 310) K and so on. An additional simulations were made at temperatures (240, 245, 250, 255, 260) K. In the beginning of every simulation run the molecule was in the *Long* conformation.

In the top panel of Fig. 4.22 the results of MD simulations are shown as orange circles (the orange curve connects orange circles and it is a guide for the eye). The green and blue curves show classical and quantum results obtained in harmonic approximation from eigenfrequencies and eigenvectors of molecular vibrations. The red circles (connected by red curve) show *corrected* MD results.

To obtain the heat capacity from MD simulations (the orange curve in the bottom panel), the derivatives of the energy curve (4.39) were calculated numerically with a temperature step 20 K for the temperatures below 200 K. For the temperatures above 200 K the slopes of the lines that provide best fit (least square fit) to the 5 values of energy (for example at temperatures 190, 195, 200, 205, 210 K) were used as the values of the heat capacities. Thus, the orange circles in the bottom panel

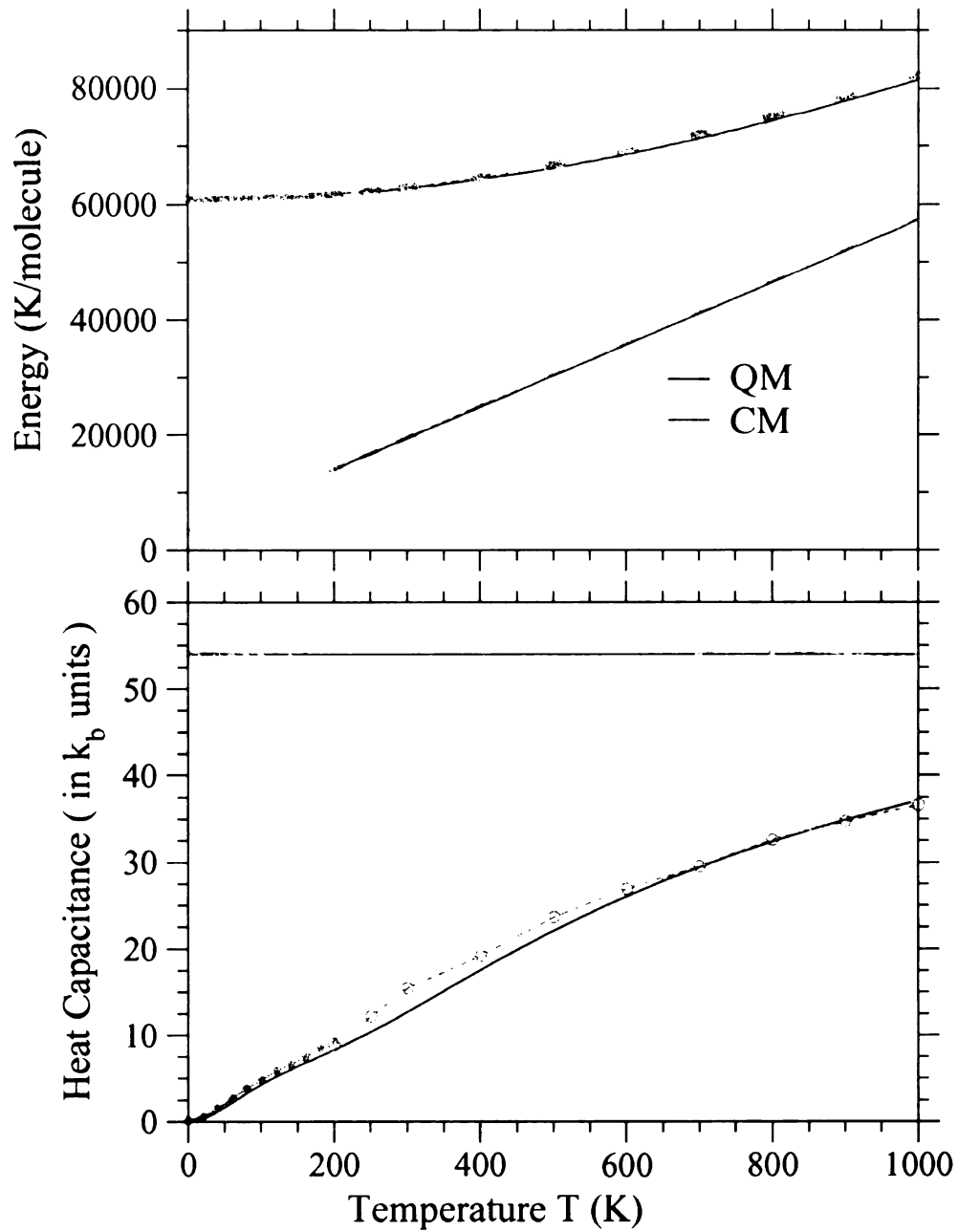


Figure 4.22: The dependencies of the energy and the heat capacity on temperature for the  $C_6H_{14}$  molecule. Blue and green curves represent the QM and CM results for the harmonic approximation to the real potential. The orange curves and circles represent the result of the MD simulations. The red curves and circles show the corrected MD results. See more detailed description of the figure in the text.

show the heat capacity obtained from the orange circles in the top panel. In the same way, red circles in the bottom panel were obtained from the red circles (red energy curve) in the top panel. The green and blue curves show classical and quantum heat capacitances obtained from eigenfrequencies and eigenvectors of molecular vibrations.

In MD simulations at low temperatures ( $T < 150$  K), the change between the *Long* and *Short* conformations does not occur. At temperatures above 150 K and below 200 K the molecule spends almost all time in the *Long* conformation. At temperatures above 200 K the amount of time that molecule spends in the higher energy (*Short*) conformation increases as temperature increases. This leads to the values of the heat capacity that are on average higher than the values of the heat capacity obtained in harmonic approximation from eigenfrequencies and eigenvectors of molecular vibrations. At temperatures above 700 K when the molecule spends approximately half of its time in the *Long* and half of its time in the *Short* conformations the heat capacity becomes again basically purely vibrational one, i.e. the values of the classical heat capacity, obtained from MD simulations, coincide with the number of vibrational modes (there are 54 vibrational modes).

In another approach the heat capacity can be calculated from the energy fluctuations using the formula:

$$C = \frac{1}{T} \frac{(\langle E^2 \rangle - \langle E \rangle^2)}{k_b T}. \quad (4.73)$$

However, this method can not be used with the “TINKER” program because the temperature is introduced into MD simulations using Berendsen’s algorithm [80] that calculates correctly the average value of the energy, but does not calculate correctly the fluctuations in the energy. If the temperature would be introduced using algorithm of W.G. Hoover [81] it would be possible to calculate heat capacity using fluctuation formula .



## 4.7 Conclusion

In this work in an attempt to develop an accurate technique for the calculation of PDF for flexible molecules we studied the role of quantum effects that are usually ignored in traditional Monte Carlo or Molecular Dynamics simulations. We found that it is very important to take into account the effect of zero-point motion for the pairs of atoms that bring sharp peaks into the PDF calculated classically. We developed a method that allows us to incorporate the effect of zero-point motion into the PDF, calculated classically from Monte Carlo or Molecular Dynamics molecular trajectories, and thus correct the classical PDF. We found that at large distances, especially when the molecule becomes flexible, its motion is almost classical.

In calculations of the total PDF for a conglomerate of molecules that are necessary to make the comparison with the experimental measurements, interactions between different molecules can be treated classically, since inter-molecular interactions are much weaker than intra-molecular interactions. Thus, the situation with inter-molecular interaction is analogous to the intra-molecular at large distances. Our correction is important if an accurate PDF in the whole range of distances is desired. It can help in reconstruction of the mutual orientations of different molecules, and thus to determine possible constraints that can be caused by the intermolecular interactions.

# Chapter 5

## Summary

In the end, as it is usually done, I want to summarize the main obtained results and list possible further developments in the studied projects.

### 5.1 Charged lattice gas with a neutralizing background

Our study of the model for the ordering of two types of ions that can occur in layered double hydroxides has lead to the following results. We found that the model predicts that only at some particular concentrations of ions would the system have homogeneous distributions of the ions in the planes. At other concentrations the system would separate into two phases with different homogeneous concentrations of ions in them. It is interesting that in spite of the original assumption that was made in the model about the homogeneity of the system we found a way to predict and study the phase separations. Thus, from the point of view of the model itself it would be interesting to consider some other physical situations to which this model can be applied. On the other hand, it may be interesting to compare the results obtained in the frame of this model with results of a model that directly allows phase separation. It is also

a possible direction for the development of the model. It follows from the structure of the layered double hydroxides that these phase separations can affect the stability of the compounds or lead to the stacking of layers with different concentrations of ions in them. We predict that these phase separations can experimentally be observed at relatively low temperatures, while at room temperatures these compounds should have homogeneous concentration of ions in the planes, i.e.; to be stable. Thus while these compounds, as predicted, should be stable at room temperature they may become unstable as temperature decreases. So far there were no detailed experimental investigations of the stability and the ordering of ions in these compounds versus ions concentration and temperature. Thus it would be interesting to have these data.

## 5.2 Behavior of the PDF at large distances

The main conclusions from our study of the behavior of the pair distribution function (PDF) at large distances are the following. We found that the natural assumption about the origin of decay in the PDF at large distances which, it seems to us, was shared by many people who work in the area is incorrect. In particular we found and proved that an increase in the number of atoms at large distances does not lead to the decay of in PDF. In other words there is no self-averaging of the PDF. The PDF at large distances decay in amorphous materials because every atom at large distances has different atomic environment. In agreement with the last statement, we found that the PDF for the crystalline materials in which every atom has the same environment does not decay at large distances. We understand that non-decaying behavior of the PDF in amorphous materials originates from relation between the amplitude of the random fluctuation in the radial density and the peculiarity in the definition of PDF. Although qualitative behavior of the PDF in crystalline materials is similar to the behavior of the PDF in amorphous materials, some quantitative features

are quite different. The behavior of the PDF in crystalline materials is closely related to the Gauss circle problem that C.F. Gauss formulated more than 150 years ago. Both problems require further investigations. Our result obtained on the behavior of the PDF in amorphous case and qualitative similarities in behavior of the PDFs in crystalline and the amorphous materials provide, from our point of view, a somewhat different perspective on the Gauss circle problem.

Another possible development is related to the derivation of a detailed analytical relation between the excluded volume and the amplitude of the oscillations in the PDF at large distances in the amorphous case.

Since our results can be used to test the amount of dislocations in crystalline materials and to test the instrumental resolutions in X-ray or neutron diffraction experiments there are two experiments that are highly desirable.

Thus, it would be valuable to compare the PDFs obtained from the two crystals made of the same material. One measurement should be done on a crystal of very good quality, while another on the crystal with significant amount of imperfections in the crystal structure. These measurements should be done on the device that provides good and stable instrumental resolution.

Other two measurements should be done on a single crystal with crystal lattice of a very high quality, but on two different machines that have different instrumental resolutions. Although information about the instrumental resolution can be extracted directly from the X-ray or neutron scattering intensity, I think that these measurements would be valuable in the modelling of the mathematical forms of the instrumental resolution functions that are used to convolute perfect PDFs obtained from the model structures in order to obtain better agreement between modelled and experimental data.

### 5.3 Quantum corrections for the PDF calculated classically

In this work, we developed a technique that allows one to incorporate the quantum effect of zero point motion into the PDF, which can be calculated for molecules in liquid or gaseous phases, using classical MD simulations. This technique should lead to an improved agreement between the modelled and experimental PDFs. The technique can also be useful for calculations of the specific heat.

The next step would be to calculate the PDF for a real liquid, which consists of relatively complicated molecules. For this purpose, it would be necessary at first to run MD for a conglomerate of molecules. Then it would be necessary to extract from the molecular trajectories the probabilities to find pairs of atoms at a particular distance. These distributions for some pairs of atoms should be corrected, using the developed technique. Summation of the PDFs for different pairs should lead to the total PDF for the conglomerate of molecules that model PDF for the real liquid.

I think that at this stage, it would be valuable to have experimental PDF for the liquid that consist of the  $C_6H_{14}$  molecules. From these data that we have it would be possible to estimate the role of the quantum corrections by comparing the calculated PDFs for a single molecule at different temperatures with experimental PDFs. High quality experimental PDF would also be valuable for the estimation of the level of the structural information that can be extracted from an experimental PDF on liquids which consist from flexible molecules.

# Appendix A

## Behavior of pdf at large distances

### A.1 Random case in d-dimensions

#### A.1.1 Ensemble averaging

Now we consider the case of completely random media when points are randomly distributed in space. In particular, it means that two points can be very close to each other; the situation that can not occur with atoms in crystals or glasses. We also assume that  $\sigma_{ij} = \sigma$  for every pair of sites  $i$  and  $j$ . In this case it is easy to make derivations for the general case of d-dimensions. The PDF function is defined in d-dimensional space as (3.9).

$$G_d(r) = r^{\frac{d-1}{2}} [\rho_d(r) - \rho_o]. \quad (\text{A.1})$$

The origin of the exponent of  $r$  will be clear from the following. The area of the surface of d-dimensional sphere of radius  $r$  can be written as  $S_d(r) = \Omega_d r^{d-1}$ , where  $\Omega_d$  is the total solid angle. Thus  $\Omega_1 = 1$ ,  $\Omega_2 = 2\pi$ ,  $\Omega_3 = 4\pi$ . Let us assume that the space is divided into very small boxes. The volume of  $i$ th box is  $dV_i = d^d r_i = d\Omega_d r_i^{d-1} dr_i$ . The number of particles in the  $i$ th box can fluctuate, but the average (averaging over

different distributions) number of sites in the  $i$ th box is  $\overline{dn_i} = \rho_o dV_i = \rho_o dS_d(r_i) dr_i = \rho_o d\Omega_d r_i^{d-1} dr_i$ . The usual relation (3.14) is applied to the average fluctuation for the number of sites in the box:  $\overline{[dn_i - \overline{dn_i}]^2} = \overline{[(dn_i)^2 - (\overline{dn_i})^2]} = \overline{dn_i}$ . In the following, while calculating  $\rho_{di}(r)$ ,  $G_{di}(r)$ , and  $G_{di}^2(r)$  with respect to a particular site we will drop indexes  $d$  and  $i$  to simplify the notations. Thus for the given distribution of sites the radial density with respect to particular site can be written as:

$$\rho(r) = \frac{1}{S_d(r)} \sum_i \frac{1}{\sqrt{2\pi\sigma^2}} \left\{ \exp\left[-\frac{(r-r_i)^2}{2\sigma_i^2}\right] \right\} dn_i. \quad (\text{A.2})$$

Ensemble averaging of (A.2) leads to

$$\overline{\rho(r)} = \int_0^\infty \frac{1}{\sqrt{2\pi\sigma^2}} \left\{ \exp\left[-\frac{(r-r_i)^2}{2\sigma_i^2}\right] \right\} \frac{\overline{\rho(\vec{r}_i)} d\Omega_d r_i^{d-1} dr_i}{\Omega_d r^{d-1}}.$$

Since  $\overline{\rho(\vec{r}_i)} = \rho_o$  there is no angular dependence and integration over the angles cancels  $\Omega_d$  in denominator. For small  $\sigma$  the contribution to the integral comes only from the region  $r_i \cong r$ . Thus we conclude that  $\overline{\rho(r)} \cong \rho_o$ . Further:

$$\overline{G^2(r)} = r^{d-1} \overline{[\rho(r) - \rho_o]^2} = r^{d-1} [\overline{\rho^2(r)} - \rho_o^2]. \quad (\text{A.3})$$

In order to calculate  $\overline{\rho^2(r)}$  it is necessary to calculate  $\overline{dn_i dn_j}$ :

$$\overline{\rho(r)^2} = \sum_{i,j} \frac{1}{\sqrt{2\pi\sigma^2}} \left\{ \exp\left[-\frac{(r-r_i)^2}{2\sigma_i^2}\right] \right\} \frac{1}{\sqrt{2\pi\sigma^2}} \left\{ \exp\left[-\frac{(r-r_j)^2}{2\sigma_j^2}\right] \right\} \frac{\overline{dn_i dn_j}}{S_d^2(r)}. \quad (\text{A.4})$$

In order to calculate  $\overline{dn_i dn_j}$  we note that:

$$\overline{dn_i dn_j} \equiv \overline{[(dn_i)^2 - (\overline{dn_i})^2]} \delta_{ij} + \overline{dn_i} \overline{dn_j},$$

where the term in square brackets is equal to  $\overline{dn_i} = \rho_o dV_i$ . If  $i \neq j$  then the summations over  $i$  and  $j$  in (A.4) can be performed separately leading to  $\rho_o^2$ . Thus we can

write:

$$\overline{\rho(r)^2} = \frac{\rho_o}{S_d(r)} \int \frac{1}{2\pi\sigma^2} \left\{ \exp \left[ -\frac{(r-r_i)^2}{\sigma^2} \right] \right\} \frac{d\Omega_d r_i^{d-1} dr_i}{\Omega_d r^{d-1}} + \rho_o^2. \quad (\text{A.5})$$

If the difference between  $r_i^d$  and  $r^d$  in the integrand is ignored, integration leads to

$$\overline{\rho(r)^2} = \frac{1}{2\sqrt{\pi} S_d(r)} \frac{\rho_o}{\sigma} + \rho_o^2.$$

Finally, from (A.3) ( $S_d(r) = \Omega_d r^{d-1}$ ) we conclude that

$$g_{di}^2(R) \equiv \overline{G_{di}^2(r)} \frac{\sigma}{\rho_o} = \frac{1}{2\sqrt{\pi}\Omega_d}. \quad (\text{A.6})$$

In the last expression we introduced index  $i$  again to emphasize that  $G_{di}^2(r)$  was calculated with respect to a particular site.

### A.1.2 Integral approach.

It is useful also to consider another approach for the calculation of  $\overline{G_{di}^2(r)}$ . In the following, for simplicity of notations, we drop index  $d$ . Instead of averaging over different distributions of sites one can calculate, for a particular distribution, the quantity:

$$\langle G_i^2(r) \rangle = \frac{1}{R_2 - R_1} \int_{R_1}^{R_2} G_i^2(r) dr = \frac{I}{R_2 - R_1}. \quad (\text{A.7})$$

In the following we explicitly show that both approaches lead to the same answer in case of the random distribution of sites. It follows from (3.7,3.9,A.1) that:

$$I = \int_{R_1}^{R_2} r^{d-1} [\rho_i^2(r) - 2\rho_i(r)\rho_o + \rho_o^2] dr. \quad (\text{A.8})$$



Further we introduce:

$$I_1 = \int_{R_1}^{R_2} r^{d-1} \rho_i^2(r) dr. \quad (\text{A.9})$$

$$I_2 = \int_{R_1}^{R_2} r^{d-1} 2\rho_i(r) \rho_o dr \quad (\text{A.10})$$

and

$$I_3 = \int_{R_1}^{R_2} r^{d-1} \rho_o^2 dr. \quad (\text{A.11})$$

It is obvious that:

$$I_3 = \int_{R_1}^{R_2} r^{d-1} \rho_o^2 dr = \frac{\rho_o}{\Omega_d} \left\{ \frac{\Omega_d}{d} [R_2^d - R_1^d] \rho_o \right\} = \frac{\rho_o}{\Omega_d} < N_{R_1}^{R_2} >, \quad (\text{A.12})$$

where  $< N_{R_1}^{R_2} >$  is an average number of particles in the spherical annulus between  $R_1$  and  $R_2$ .

For  $I_2$  using expression (3.8) for  $\rho_i(r)$ , in the assumption that  $\sigma_{ij} = \sigma$ , we write (If indices of summation are not shown it is assumed that the summations goes over such  $j$  that  $R_1 < r_{ij} < R_2$ ):

$$\begin{aligned} I_2 &= \int_{R_1}^{R_2} r^{d-1} 2\rho(r) \rho_o dr \\ &= \frac{2\rho_o}{\Omega_d} \int_{R_1}^{R_2} \Omega_d r^{d-1} \frac{1}{\Omega_d r^{d-1}} \sum_{j \neq i} \frac{1}{\sqrt{2\pi\sigma^2}} \left\{ \exp \left[ -\frac{(r - r_{ij})^2}{2\sigma^2} \right] \right\} dr \\ &= \frac{2\rho_o}{\Omega_d} \sum_{j \neq i} \int_{R_1}^{R_2} \frac{1}{\sqrt{2\pi\sigma^2}} \left\{ \exp \left[ -\frac{(r - r_{ij})^2}{2\sigma^2} \right] \right\} dr \\ &\cong \frac{2\rho_o}{\Omega_d} \sum 1 \\ &\simeq \frac{2\rho_o}{\Omega_d} < N_{R_1}^{R_2} > . \end{aligned} \quad (\text{A.13})$$

It was assumed during the last derivation that ( $\cong$  sign)  $\sigma \ll R_2 - R_1$  so that basically only sites inside of the annulus contribute to the value of the integral. This assumption is also used everywhere in the further derivations. We used the sign  $\simeq$  since for the particular distribution of sites the number of sites inside the spherical annulus can deviate from its average value  $\langle N_{R_1}^{R_2} \rangle$  with standard deviation  $\sqrt{\langle N_{R_1}^{R_2} \rangle}$ .

For  $I_1$  from (A.9.3.8) we have:

$$I_1 = \sum_{j \neq i} \sum_{k \neq i} \int_{R_1}^{R_2} \frac{1}{\Omega_d \sqrt{2\pi\sigma^2}} \left\{ \exp\left[-\frac{(r - r_{ij})^2}{2\sigma^2}\right] \right\} \frac{1}{\Omega_d \sqrt{2\pi\sigma^2}} \left\{ \exp\left[-\frac{(r - r_{ik})^2}{2\sigma^2}\right] \right\} \frac{dr}{r^{d-1}}.$$

This expression can be split into the two sums  $I_1 = I_{11} + I_{12}$ . In the first sum  $I_{11}$ :  $j = k$  while in the second  $I_{12}$ :  $j \neq k$ . Thus (If indices of summation are not shown it is assumed that the summations goes over such  $j$  that  $R_1 < r_{ij} < R_2$ ):

$$\begin{aligned} I_{11} &= \frac{1}{2\sqrt{\pi}\Omega_d^2\sigma} \sum_{j \neq i} \int_{R_1}^{R_2} \frac{1}{\sqrt{\pi\sigma^2}} \left\{ \exp\left[-\frac{(r - r_{ij})^2}{\sigma^2}\right] \right\} \frac{dr}{r^{d-1}} \\ &\cong \frac{1}{2\sqrt{\pi}\Omega_d^2\sigma} \sum \frac{1}{r_{ij}^{d-1}} \\ &\simeq \frac{1}{2\sqrt{\pi}\Omega_d^2\sigma} \int_{R_1}^{R_2} \frac{1}{r_{ij}^{d-1}} \Omega_d r_{ij}^{d-1} \rho_o dr_{ij} \\ &= \frac{1}{2\sqrt{\pi}\Omega_d} \frac{\rho_o}{\sigma} (R_2 - R_1). \end{aligned} \quad (\text{A.14})$$

It follows from (A.14) that expression for  $I_{12}$  can be written as:

$$\begin{aligned} I_{12} &= \sum_j \sum_{k \neq j} \frac{1}{\sqrt{4\pi\sigma^2}} \exp\left[-\frac{(r_{ij} - r_{ik})^2}{4\sigma^2}\right] \\ &\quad \cdot \frac{1}{\Omega_d^2} \int_{R_1}^{R_2} \frac{1}{r^{d-1}} \frac{1}{\sqrt{\pi\sigma^2}} \exp\left[-\frac{1}{\sigma^2} \left(r - \frac{r_{ij} + r_{ik}}{2}\right)^2\right] dr. \end{aligned} \quad (\text{A.15})$$

The integral in the last expression has non-zero value if  $r \simeq (r_{ij} + r_{ik})/2 \pm \sigma$ . Since  $\sigma$  is small (A.15) can be rewritten as (If indices of summation are not shown it is

assumed that the summations goes over such  $j$  that  $R_1 < r_{ij} < R_2$ ):

$$I_{12} \cong \frac{1}{\Omega_d^2} \sum_{k \neq j} \frac{1}{\sqrt{4\pi\sigma^2}} \cdot \exp\left[-\frac{(r_{ij} - r_{ik})^2}{4\sigma^2}\right] \cdot \left[\frac{2}{r_{ij} + r_{ik}}\right]^{d-1}. \quad (\text{A.16})$$

Further we substitute summation over  $k$  by integration assuming mean distribution of sites (If indices of summation are not shown it is assumed that the summations goes over such  $j$  that  $R_1 < r_{ij} < R_2$ ):

$$\begin{aligned} I_{12} &\cong \sum_{R_1}^{R_2} \frac{1}{\sqrt{4\pi\sigma^2}} \left\{ \exp\left[-\frac{(r_{ij} - r_{ik})^2}{4\sigma^2}\right] \right\} \\ &\quad \cdot \frac{1}{\Omega_d^2} \left[\frac{2}{r_{ij} + r_{ik}}\right]^{d-1} \cdot \Omega_d r_{ik}^{d-1} \rho_o dr_{ik} \\ &\cong \frac{\rho_o}{\Omega_d} \sum 1 \simeq \frac{\rho_o}{\Omega_d} < N_{R_1}^{R_2} >. \end{aligned} \quad (\text{A.17})$$

Since  $I_1 = I_{11} + I_{12}$ :

$$I_1 \simeq \frac{1}{2\sqrt{\pi}\Omega_d} \frac{\rho_o}{\sigma} (R_2 - R_1) + \frac{1}{\Omega_d} \rho_o < N_{R_1}^{R_2} >. \quad (\text{A.18})$$

Finally, for  $I = I_1 - I_2 + I_3$  we write:

$$\begin{aligned} I &\simeq \frac{1}{2\sqrt{\pi}\Omega_d} \frac{\rho_o}{\sigma} (R_2 - R_1) + \frac{\rho_o}{\Omega_d} < N_{R_1}^{R_2} > - \frac{2\rho_o}{\Omega_d} < N_{R_1}^{R_2} > + \frac{\rho_o}{\Omega_d} < N_{R_1}^{R_2} > \quad (\text{A.19}) \\ &= \frac{1}{2\sqrt{\pi}\Omega_d} \frac{\rho_o}{\sigma} (R_2 - R_1). \end{aligned}$$

Note that in the expression above, the value of the  $< N_{R_1}^{R_2} >$  is determined with precision  $\sqrt{< N_{R_1}^{R_2} >}$  (that is the origin of the  $\simeq$  sign) and that all terms in which  $< N_{R_1}^{R_2} >$  is present directly cancel each other. It is also indirectly present in the remaining term (see (A.15)). However it does not affect the domination of the main value of the remaining term.

Thus, for  $g_d^2(R)$  we have:

$$g_d^2(R) = \langle G_{di}^2(r) \rangle \frac{\sigma}{\rho_o} \cong \frac{1}{2\sqrt{\pi}\Omega_d}, \quad (\text{A.20})$$

which is the same expression (A.6) that was obtained from ensemble averaging.

## A.2 Amorphous case in d-dimensions: integral approach

### A.2.1 Difference with the random case from the integral approach: detailed derivation

The derivation for the random case with forbidden volume goes in the same way as for the completely random case. The only difference comes from the fact that when there is forbidden volume around every point expression (A.18) should be modified into (If indices of summation are not shown it is assumed that the summations goes over such  $j$  that  $R_1 < r_{ij} < R_2$ ):

$$I_{12} \cong \sum \int_{R_1}^{R_2} \frac{1}{\sqrt{4\pi\sigma^2}} \left\{ \exp \left[ -\frac{(r_{ij} - r_{ik})^2}{4\sigma^2} \right] \right\} \cdot \frac{1}{\Omega_d^2} \left[ \frac{2}{r_{ij} + r_{ik}} \right]^{d-1} \cdot (\Omega_d r_{ik}^{d-1} - \gamma \lambda^{d-1}) \rho_o dr_{ik}. \quad (\text{A.21})$$

This change comes from the fact that if, in an amorphous case, there is a point  $j$  at a distance  $r_{ij}$  then point  $k$  should be placed in such a way that  $|r_{ij} - r_{ik}| \sim \sigma$ . Otherwise the exponent in expression (A.22) will vanish. But in an amorphous case not the whole volume  $\Omega_d r_{ij}^{d-1} dr_{ij}$  is available for placing point  $k$ . There is forbidden volume around the site  $j$ :  $V_f \cong \gamma \lambda^d dr_{ij}$ , where  $\lambda$  can be considered as the distance between the nearest neighbors and  $\gamma$  is the coefficient that depends on the structure. Thus, see

Fig.3.8, effectively  $\Omega_d r_{ik}^2 dr_{ik}$  turns into  $(\Omega_d r_{ik}^{d-1} - \gamma \lambda^{d-1}) dr_{ik}$ . Further (compare with (A.18)) (If indices of summation are not shown it is assumed that the summations goes over such  $j$  that  $R_1 < r_{ij} < R_2$ ):

$$\begin{aligned}
I_{12} &\simeq \frac{\rho_o}{\Omega_d} \langle N_{R_1}^{R_2} \rangle \\
&\quad - \sum \int_{R_1}^{R_2} \frac{1}{\Omega_d^2 \sqrt{4\pi\sigma^2}} \left\{ \exp \left[ -\frac{(r_{ij} - r_{ik})^2}{4\sigma^2} \right] \right\} \frac{2^{d-1} \cdot \gamma \lambda^{d-1} \rho_o dr_{ik}}{(r_{ij} + r_{ik})^{d-1}} \\
&\simeq \frac{\rho_o}{\Omega_d} \langle N_{R_1}^{R_2} \rangle - \frac{\gamma \lambda^{d-1} \rho_o}{\Omega_d^2} \sum \frac{1}{r_{ij}^{d-1}}.
\end{aligned} \tag{A.22}$$

Using mean density approximation, we again switch from the sum to the integral:

$$\begin{aligned}
I_{12} &\simeq \frac{\rho_o}{\Omega_d} \langle N_{R_1}^{R_2} \rangle - \frac{\gamma \lambda^{d-1} \rho_o}{\Omega_d^2} \int_{R_1}^{R_2} \frac{1}{r_{ij}^{d-1}} \Omega_d r_{ij}^{d-1} \rho_o dr_{ij} \\
&\simeq \frac{\rho_o}{\Omega_d} \langle N_{R_1}^{R_2} \rangle - \frac{\gamma \lambda^{d-1} \rho_o^2}{\Omega_d} (R_2 - R_1).
\end{aligned} \tag{A.23}$$

Thus, in an amorphous case for  $I = I_1 - I_2 + I_3$  we have:

$$I \simeq \left[ \frac{1}{2\sqrt{\pi}\Omega_d} \frac{\rho_o}{\sigma} - \frac{\gamma \lambda^{d-1} \rho_o^2}{\Omega_d} \right] (R_2 - R_1) \tag{A.24}$$

So that for  $\langle G_{di}^2(r) \rangle$  we get:

$$\langle G^2(r) \rangle \cong \frac{1}{2\sqrt{\pi}\Omega_d} \frac{\rho_o}{\sigma} [1 - 2\sqrt{\pi}\gamma \lambda^{d-1} \rho_o \sigma]. \tag{A.25}$$

Since  $\rho_o = 1/\lambda^d$ :

$$g_{di}^2(F) = \langle G_{di}^2(r) \rangle > \frac{\sigma}{\rho_o} \cong \frac{1}{2\sqrt{\pi}\Omega_d} [1 - 2\sqrt{\pi}\gamma \frac{\sigma}{\lambda}]. \tag{A.26}$$

### A.3 1d crystal

From the definition of radial density in 1d (3.8) it follows that:

$$\rho(r) = \frac{1}{\sqrt{2\pi\sigma^2}} \sum_{n=-\infty}^{\infty} \exp\left[-\frac{(r-na)^2}{2\sigma^2}\right], \quad (\text{A.27})$$

while from the definition of PDF in 1d (3.7):

$$G^2(r) = \rho^2(r) - 2\rho_o\rho(r) + \rho_o^2. \quad (\text{A.28})$$

Due to the periodicity of the lattice, in order to find  $\langle G^2(r) \rangle$ , it is enough to perform integration (3.10) over any interval of length  $a$ . Because of the structure of expression (A.27) for  $\rho(r)$  and its physical meaning, the integral of  $\rho(r)$  over any interval of length  $a$  should be equal to  $\rho_o a = 1$ , i.e.  $\langle \rho(r) \rangle = \rho_o$ . Thus, for any  $R$ , we can write:

$$\int_R^{R+a} \sum_{n=-\infty}^{\infty} \frac{1}{\sqrt{2\pi\sigma^2}} \left\{ \exp\left[-\frac{(r-na)^2}{2\sigma^2}\right] \right\} dr = 1, \quad (\text{A.29})$$

while  $\langle G^2(r) \rangle = \langle \rho^2(r) \rangle - \rho_o^2$ . From (A.27) follows that:

$$\rho^2(r) = \sum_{n=-\infty}^{\infty} \sum_{m=-\infty}^{\infty} \frac{1}{2\pi\sigma^2} \left\{ \exp\left[-\frac{(r-na)^2 + (r-ma)^2}{2\sigma^2}\right] \right\}. \quad (\text{A.30})$$

Since

$$(r-na)^2 + (r-ma)^2 = 2\left[r - \frac{(n+m)a}{2}\right]^2 + \frac{(n-m)^2 a^2}{2},$$

expression for  $\rho^2(r)$  can be rewritten. If  $i = n - m$  and  $j = n + m$  then:

$$\rho^2(r) = \sum_{i=-\infty}^{\infty} \frac{1}{2\sqrt{\pi}\sigma} \left\{ \exp\left[-\frac{i^2 a^2}{4\sigma^2}\right] \right\} \sum_j \frac{1}{\sqrt{\pi\sigma^2}} \left\{ \exp\left[-\frac{(r - \frac{ja}{2})^2}{\sigma^2}\right] \right\}. \quad (\text{A.31})$$

In the terms that arise from the last expression  $i$  and  $j$  should be both even or odd.

Thus for  $\langle \rho^2(r) \rangle$  we get (compare with (A.29)):

$$\frac{1}{a} \int_R^{R+a} \rho^2(r) dr = \sum_{i=-\infty}^{\infty} \frac{1}{2\sqrt{\pi}\sigma a} \left\{ \exp \left[ -\frac{i^2 a^2}{4\sigma^2} \right] \right\}. \quad (\text{A.32})$$

From that it follows:

$$\langle G^2(r) \rangle = \frac{1}{2\sqrt{\pi}} \frac{\rho_o}{\sigma} \left[ 1 - 2\sqrt{\pi} \frac{\sigma}{a} \right] + 2 \frac{1}{2\sqrt{\pi}} \frac{\rho_o}{\sigma} \sum_{n=1}^{\infty} \exp \left[ -\frac{n^2 a^2}{4\sigma^2} \right]. \quad (\text{A.33})$$

Finally:

$$\frac{g_{1L}^2(\sigma)}{g_{1R}^2(\sigma)} = \left[ 1 - 2\sqrt{\pi} \frac{\sigma}{a} \right] + 2 \sum_{n=1}^{\infty} \exp \left[ -\frac{n^2 a^2}{4\sigma^2} \right]. \quad (\text{A.34})$$

## Appendix B

### Cut-off for the Morse potential

In order to find  $\sigma_{MCM}^2$  and  $\langle U(T) \rangle$  for the Morse potential, it is necessary to perform integrations (4.14, 4.17, 4.38) with the Morse potential used as  $U(x)$ . For the Morse potential as  $r \rightarrow \infty$  the value of potential goes to *const*, i.e.  $\exp[-U(x)/(k_bT)]$  also goes to *const*. Thus the integrals under consideration diverge as  $r \rightarrow \infty$ . This divergence means that in infinite time, a particle would escape from the potential at any temperature. Due to this divergence it is unclear what should be the upper limit of the integration. However, if temperature is low enough, there is a range of upper cut-offs (sufficiently big, but not too big) that would lead to the same results with respect to  $\sigma_{MCM}^2(T)$  and  $\langle U_{MCM}(T) \rangle$ .

Figure B.1 shows dependencies of  $\sigma_{MCM}^2(T)$  and  $\langle U_{MCM}(T) \rangle$  on temperature for different values of cut-off. Thus, we see that if  $T \leq 10000$  K any reasonable value of cut-off leads to the basically the same results. Thus for the curves on the Fig.4.4, 4.5, 4.6 cut off 2.5 (Å) was used.



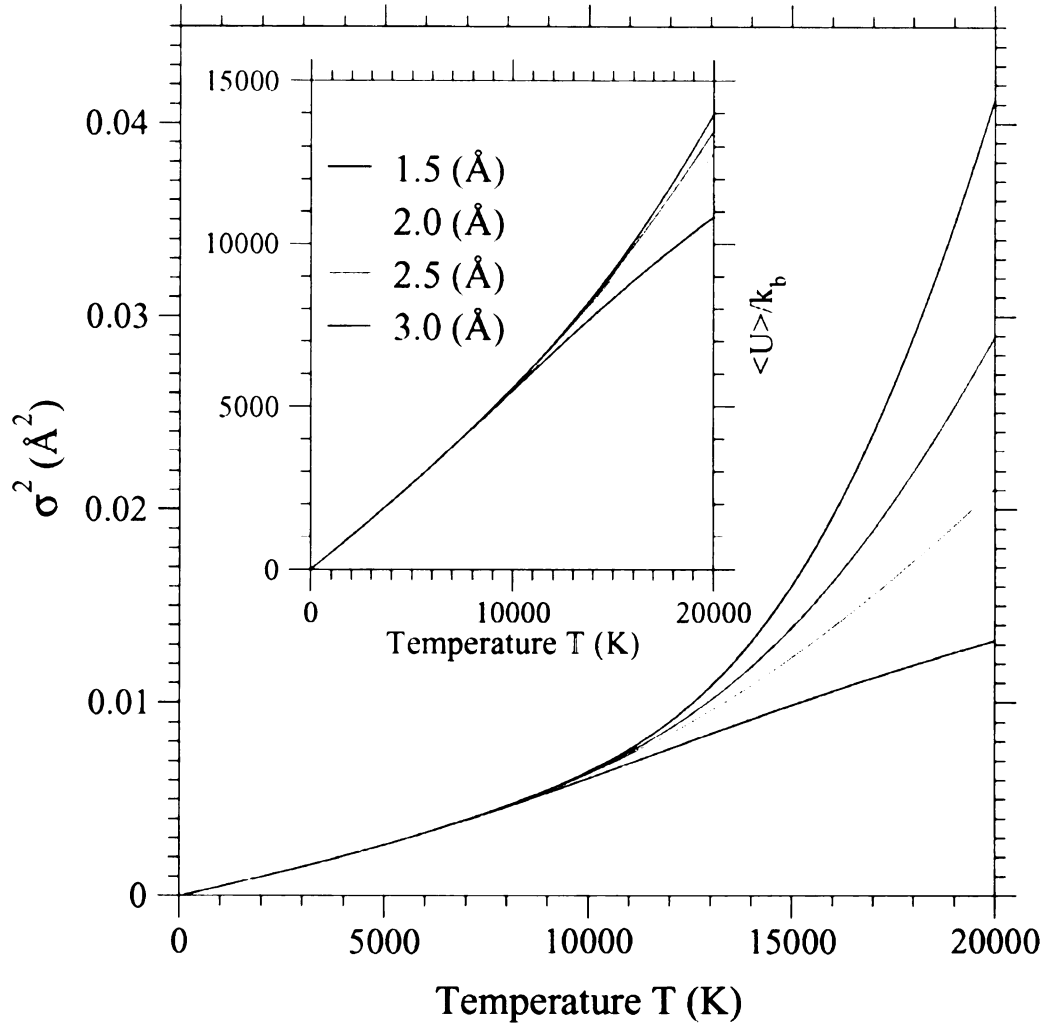


Figure B.1: Dependencies of  $\sigma^2_{MCM}(T)$  on temperature (see Fig.4.4) for different values of the upper cut off in the integrals (4.14, 4.17). Thus, if  $T \leq 10000$  (K) any cut-off in the interval (1.5:3.0) \text{\AA} would lead to basically the same result. The inset shows how  $\langle U_{MCM}(T) \rangle$  (in temperature units) depends on temperature. Thus for the potential energy any upper cut off (see (4.38)) in the interval (1.5:3.0) \text{\AA} is also suitable.

## Bibliography

- [1] Y. Xiao, M. F. Thorpe and J. B. Parkinson, Phys. Rev. B **59**, 277 (1999).
- [2] V.A. Levashov, M. F. Thorpe and B. W. Southern, Phys. Rev. B **67**, 224109 (2003).
- [3] H.F.W. Taylor, Mineral. Mag. **39**, 377 (1973).
- [4] D.L. Bish and G.W. Brindley, Am. Miner. **62**, 458 (1977).
- [5] G.W. Brindley and S. Kikkawa, Am. Miner. **64**, 836 (1979)
- [6] S.A. Solin, D.R. Hines, G.T. Seidler and M.M.J. Treacy, J. Phys. Chem. Solids **57**, 1043 (1996)
- [7] D.R. Hines, G.T. Seidler, M.M.J. Treacy and S.A. Solin, Solid State Commun. **101**, 835 (1997).
- [8] S.A. Solin, D.R. Hines, S.K. Yuk, T.J. Pinnavaia and M.F. Thorpe, J. Non-Crystal. Solids **182**, 212 (1995).
- [9] A. Audemer, A. Delahaye, R. Farhi, N. SacEpee and J.M. Tarascon, J. Electrochem. Soc. **144**, 2614 (1997).
- [10] S.U. Falk and A.J. Salkind, Alkaline Storage Batteries, Wiley, New York, 1969.
- [11] R. Barnard and C.F. Randell, J. Appl. Electrochem. **13**, 97 (1983).
- [12] A.D. Vidal and M. Figlarz, J. Appl. Electrochem. **17**, 589 (1987).
- [13] P. Elumalai, H.N. Vasan and N. Munichandraiah, J. Power Sources **93**, 201 (2001).
- [14] B. Liu, X.Y. Wang, H.T. Yuan, Y.S. Zhang, D.Y. Song and Z.X. Zhou, J. Appl. Electrochem. **29**, 855 (1999)
- [15] C. Faure, C. Delmas and P. Willmann, J. Power Sources **36**, 497 (1991).
- [16] G.A. Caravaggio, C. Detellier and Z. Wronski, J. Mater. Chem. **11**, 912 (2001).
- [17] F.Ducastelle, *Order and Phase Stability in Alloys*, Elsevier Science Publishers B.V. Amsterdam, The Netherlands, 1991.

- [18] A.J. Berlinsky, W.G. Unruh, W.R. McKinnon and R.R. Haering, Solid. State. Commun. **31**, 135 (1979).
- [19] W. Li, J.N. Reimers and J.R. Dahn, Phys. Rev. B **46**, 3236 (1992).
- [20] A.H. Thompson, J. Electrochem. Soc. **126**, 608 (1979).
- [21] M. Winter, J.O. Besenhard, M.E. Spahr and P. Novak, Adv. Mater. **10**, 725 (1998).
- [22] T. Zheng and J.R. Dahn, Phys. Rev. B **56**, 3800 (1997).
- [23] S.A. Safran and D.R. Hamann, Phys. Rev. B **22**, 606 (1980).
- [24] S.A. Safran and D.R. Hamann, Phys. Rev. Lett. **42**, 1410 (1979).
- [25] H.A. Kramers and G.H. Wannier, Phys. Rev. **60**, 252 (1941).
- [26] M. E. J. Newman and G.T. Barkema, *Monte Carlo Methods in Statistical Physics*, Oxford University Press Inc., New York, 1999.
- [27] A.C. Maggs and V. Rossetto, Phys. Rev. Lett. **88**, 196402 (2002).
- [28] E.P. Wigner, Phys. Rev. **46**, 1002 (1934).
- [29] G. Meissner, H. Namaizawa and M. Voss Phys. Rev. **13**, 4 (1976).
- [30] L. Bonsall and A.A. Maradudin, Phys. Rev. B **15**, 1959 (1977).
- [31] This exact result only agrees with the approximate expression in equation (11) of reference[1] in the limit  $x \rightarrow 0$
- [32] F. Zernicke, J.A. Prins Zeit Physik. **41**, 184- (1927).
- [33] P.J.W. Debye, H. Menke Physical. Zeit. **31**, 797 (1930).
- [34] B.E. Warren X-ray diffraction (Dover Publications 1990).
- [35] J.S. Chung, M.F. Thorpe Local atomic structure of semiconductor alloys using pair distribution function Phys. Rev. B **59**, 1545-1553 (1997).
- [36] M.F. Thorpe, J.S.Chung, S.J.L. Billinge and F. Mohiuddin-Jacobs Advances in Pair Distribution Profile Fitting in Alloys in Local Structure from Diffraction, 157-174, Ed. By S.J.L. Billinge and M.F. Thorpe (Plenum Press, New York, 1998)
- [37] M.F. Thorpe, V.A. Levashov, M. Lei and S.J.L. Billinge Notes on the analysis of data for pair distribution functions, 105-128, Ed. By S.J.L. Billinge and M.F. Thorpe (Kluwer Academic/Plenum Publishers, New York, 2002)
- [38] D.A. Dimitrov, H. Röder and A.R. Bishop Phys. Rev. B **64**, 14303 (2001)

- [39] B.H. Toby and T. Egami *Acta Cryst.* **48**, 336 (1992)
- [40] For a summary on Lattice Point Theory, see <http://mathworld.wolfram.com/PointLattice.html>
- [41] E. Krätzel *Lattice Points*, Kluwer Academic Publishers (1988)
- [42] P. Erdős, P.M. Gruber, and J. Hammer *Lattice Points*, Longman Scientific and Technical with John Wiley and Sons, Inc., New York (1989)
- [43] C.F. Gauss *De nexu inter multitudinem classium, in quas formae binariae secundi gradus distribuuntur, earumque determinantem.* *Werke*, vol.2, pp.269-291 (277)
- [44] For a summary of what is known about the Gauss Circle Problem, see <http://mathworld.wolfram.com/GaussCircleProblem.html>
- [45] L.D. Landau, E.M. Lifshitz *Statistical Physics P1* (1999)
- [46] S. Torquato, T.M. Truskett and P.G. Debenedetti *Is Random Close Packing of Spheres Well Defined?* *Phys. Rev. Lett.*, **84**, 2064 (2000)
- [47] W.M. Visscher and M. Bolsterli *Nature (London)* **239**, 504 (1972) See also remarks published in *Nature (London)* **239**, 488 (1972)
- [48] J. Tobochnik and P.M. Chapin *J. Chem. Phys.* **88**, 5824 (1988).
- [49] F. Wooten, K. Winer, D. Weaire *Phys. Rev. Lett.* **54**, 1392 (1985).
- [50] H. He *Ph.D. thesis*, Michigan State University (1985).
- [51] G.T. Barkema and N. Mousseau *High-quality continuous random networks.* *Phys. Rev. B* **62**, 4985-4990 (2000).
- [52] R.L.C. Vink, G.T. Barkema, M.A. Stijnman and R.H. Bisseling *Towards device-size computer models of amorphous silicon.* *Phys. Rev. B* **64**, 245214 (2001).
- [53] M.N. Huxley *Exponential Sums and Lattice Points.* *Proc.London Math. Soc.* **60**, 471-502, 1990
- [54] G. H. Hardy *Quart. J. Math.* **46**, 283, 1915
- [55] E. Landau *Über die Gitterpunkte in einem Kreise. (Zweite Mitteilung.)* *Nachrichten der K. Gesellschaft der Wissenschaften zu Göttingen. Mathematisch-physikalische Klasse.* 161-171 (1915).
- [56] P.M. Bleher *Duke Mathematical Journal* **67**, No.3 p.461
- [57] P.M. Bleher, F.J. Dyson and J.L. Lebowitz *Non-Gaussian energy level statistics for some integrable systems* *Phys. Rev. Lett.* **71**, No.19 p.3047-3050 (1993)

- [58] J.S. Chung, M.F. Thorpe Local atomic structure of semiconductor alloys using pair distribution function Phys. Rev. B **59**, 1545-1553 (1997).
- [59] R. Car and M. Parinello Unified Approach for Molecular Dynamics and Density-Functional Theory, Phys. Rev. Lett. **55**, p.2471-2474 (1985)
- [60] M. J. Frisch, G. W. Trucks, H. B. Schlegel, G. E. Scuseria, M. A. Robb, J. R. Cheeseman, V. G. Zakrzewski, J. A. Montgomery, Jr., R. E. Stratmann, J. C. Burant, S. Dapprich, J. M. Millam, A. D. Daniels, K. N. Kudin, M. C. Strain, O. Farkas, J. Tomasi, V. Barone, M. Cossi, R. Cammi, B. Mennucci, C. Pomelli, C. Adamo, S. Clifford, J. Ochterski, G. A. Petersson, P. Y. Ayala, Q. Cui, K. Morokuma, P. Salvador, J. J. Dannenberg, D. K. Malick, A. D. Rabuck, K. Raghavachari, J. B. Foresman, J. Cioslowski, J. V. Ortiz, A. G. Baboul, B. B. Stefanov, G. Liu, A. Liashenko, P. Piskorz, I. Komaromi, R. Gomperts, R. L. Martin, D. J. Fox, T. Keith, M. A. Al-Laham, C. Y. Peng, A. Nanayakkara, M. Challacombe, P. M. W. Gill, B. Johnson, W. Chen, M. W. Wong, J. L. Andres, C. Gonzalez, M. Head-Gordon, E. S. Replogle, and J. A. Pople, Gaussian, Inc., Pittsburgh PA, 2001.
- [61] M.J.S. Dewar, E.G. Zoebisch and E.F. Healy Gaussian 98, Revision A.11.1, J. Amer. Chem. Soc. **107**, 3902 (1985)
- [62] L.D.Landau and E.M. Lifshits Quantum Mechanics: Non-Relativistic Theory, Volume 3, Butterworth-Heinemann; 3rd edition (February 1997)
- [63] L.D.Landau and E.M. Lifshits Statistical Physics, Volume 5, Butterworth-Heinemann; 3rd edition, Part 1 (February 1999)
- [64] P.M. Morse Phys. Rev. **34** 57-64 (1929)
- [65] N. L. Allinger, Y. H. Yuh and J.-H. Lii, "Molecular Mechanics. The MM3 Force Field for Hydrocarbons. 1", J. Am. Chem. Soc., **111**, 8551-8566 (1989)
- [66] J.-H. Lii and N. L. Allinger, "Molecular Mechanics. The MM3 Force Field for Hydrocarbons. 2. Vibrational Frequencies and Thermodynamics", J. Am. Chem. Soc., **111**, 8566-8575 (1989)
- [67] J.-H. Lii and N. L. Allinger, "Molecular Mechanics. The MM3 Force Field for Hydrocarbons. 3. The van der Waals' Potentials and Crystal Data for Aliphatic and Aromatic Hydrocarbons", J. Am. Chem. Soc., **111**, 8576-8582 (1989)
- [68] N. L. Allinger, H. J. Geise, W. Pyckhout, L. A. Paquette and J. C. Gallucci, "Structures of Norbornane and Dodecahedrane by Molecular Mechanics Calculations (MM3), X-ray Crystallography, and Electron Diffraction", J. Am. Chem. Soc., **111**, 1106-1114 (1989) [torsion-stretch]
- [69] N. L. Allinger, F. Li and L. Yan, "Molecular Mechanics. The MM3 Force Field for Alkenes", J. Comput. Chem., **11**, 848-867 (1990)

- [70] N. L. Allinger, F. Li, L. Yan and J. C. Tai, "Molecular Mechanics (MM3) Calculations on Conjugated Hydrocarbons", *J. Comput. Chem.*, **11**, 868-895 (1990)
- [71] J.-H. Lii and N. L. Allinger, "Directional Hydrogen Bonding in the MM3 Force Field. I", *J. Phys. Org. Chem.*, **7**, 591-609 (1994)
- [72] J.-H. Lii and N. L. Allinger, "Directional Hydrogen Bonding in the MM3 Force Field. II", *J. Comput. Chem.*, **19**, 1001-1016 (1998)
- [73] See the Internet web-site of the "TINKER" program:  
<http://dasher.wustl.edu/tinker/>
- [74] P. Ren and J. W. Ponder, *J. Phys. Chem. B*, **107**, 5933-5947 (2003)
- [75] R. V. Pappu, R. K. Hart and J. W. Ponder, *J. Phys. Chem. B*, **102**, 9725-9742 (1998)
- [76] M. E. Hodsdon, J. W. Ponder and D. P. Cistola, *J. Mol. Biol.*, **264**, 585-602 (1996)
- [77] M. J. Dudek and J. W. Ponder, *J. Comput. Chem.*, **16**, 791-816 (1995)
- [78] C. E. Kundrot, J. W. Ponder and F. M. Richards, *J. Comput. Chem.*, **12**, 402-409 (1991)
- [79] J. W. Ponder and F. M. Richards, *J. Comput. Chem.*, **8**, 1016-1024 (1987)
- [80] H.J.C. Berendsen, J.P.M. Postma, W.F. van Gunsteren, A. DiNola and J. R. Haak *J. Comput. Chem.*, **8**, 1016-1024 (1987)
- [81] W.G. Hoover *Phys. Rev. A* **31** 1695-1697 (1985)

MICHIGAN STATE UNIVERSITY LIBRARIES



3 1293 02498 6261